



---

# QFIRST

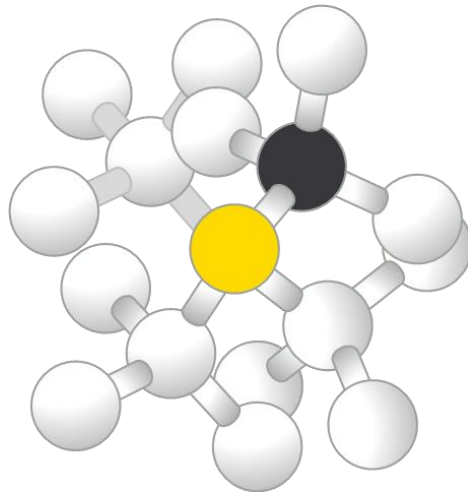
## Quantum Sensing & Metrology

### Nitrogen Vacancy Centers in Diamond

# State of the Art

Edited by Nina Slobodian, PhD, 2022

---



[www.tecnalia.com](http://www.tecnalia.com)



[www.ehu.es](http://www.ehu.es)



<https://cfm.ehu.es>



[www.tekniker.com](http://www.tekniker.com)



<https://www.a-v-s.es/>

This initiative is supported by the Basque Government through the ELKARTEK Program under Grant KK2022/00062 – Qfirst, Devices based on Quantum Technologies.





## Contents

<b>1. Diamond classification .....</b>	<b>10</b>
1.1 Classification by types according to their optical absorption	10
1.2 Classification by defects	11
1.3 Classification by synthetic diamond growth methods	11
1.4 Classification by crystallite size	11
<b>2. Diamond synthesis .....</b>	<b>12</b>
2.1 Types, forms and sizes of synthesized diamonds	12
2.2 Features of the CVD method in comparison with the HPHT method	13
<b>3. Nitrogen-vacancy centers in diamond.....</b>	<b>15</b>
3.1 What is an NV center in diamond?	15
3.2 Generation of fluorescent defects	15
3.3 Properties of the diamond chip and fluorescent defects that impact sensing performance	16
3.3.1 Methods to make NV layers of varying thickness.....	17
3.3.2 NV centers, isotopes and impurity concentration .....	17
3.3.3 Synthetic diamond chips cuts .....	18
3.4 NV center electronic structure	19
3.5 NV center optical properties	20
3.6 NV center spin properties	21
3.7 Hyperfine splitting	22
3.8 NV center spin Hamiltonian	22
<b>4. Magnetometry introduction &amp; operation regimes depending on the magnetic field amplitude .....</b>	<b>27</b>
4.1 Weak magnetic field regime	28
4.2 Strong magnetic field regime	29
<b>5. Sensing protocols.....</b>	<b>31</b>
5.1 Continuous-wave optically detected magnetic resonance (CW-ODMR)	31
5.2 Pulsed ODMR	32
5.3 Ramsey measurements	33
5.4 Rabi beat sensing	35
5.5 AC detection. Spin-echo magnetometry	35
5.6 Relaxometry	35
5.7 Double-quantum (DQ) coherence magnetometry	36
5.8 Spin-to-charge conversion (SCC) readout	37
5.9 Ancilla-assisted repetitive readout	39
5.10 Geometric phase magnetometry	41
5.11 Summarized representation of different NV measurement protocols	42



<b>6. Characteristic coherence times for NV centers .....</b>	<b>44</b>
6.1 $T_1$ Relaxation time	44
6.2 $T_2$ coherence time	45
6.3 $T_2^*$ dephasing time	46
6.4 Typical coherence times	47
<b>7. Sensitivity .....</b>	<b>48</b>
7.1 Spin projection noise and photon shot noise	48
7.2 Physical quantities which are measured by sensors on NV centers	48
7.3 Dependence on temperature	49
7.4 Ways to improve sensitivity	49
7.5 Diamond growth technique to optimize the performance of NV-based quantum sensing	50
7.6 Engineering NV defects close to surfaces	51
7.7 Sensitivity of CW-ODMR method for DC magnetic fields	52
7.8 Sensitivity for a Pulsed ODMR and Ramsey-type NV magnetometry	52
7.9 Sensitivity to AC magnetic fields	53
7.10 Parameters limiting sensitivity	54
<b>8. Equipment choice and its impact on instrument performance .....</b>	<b>56</b>
8.1 Laser	56
8.2 Microwave source	57
8.3 Static magnetic field	58
8.4 Optics for illumination and fluorescence collection	59
8.5 Camera	60
8.6 Diamond mounting and configuration	62
8.7 General design considerations	63
<b>9. Navigation without external references .....</b>	<b>64</b>
9.1 Inertial navigation systems	64
9.2 Map-based navigation using magnetic field measurements	66
9.3 Dark Ice quantum magnetometer of Lockheed Martin	67
<b>10. Rotation measurement using NV-center sensors .....</b>	<b>69</b>
10.1 Development of spin-based rotation measurement	69
10.2 Sensing mechanism of spin-based rotation measurement	69
10.3 Sensitivity optimization of spin-based rotation measurement	72
10.4 Nuclear magnetic resonance gyroscopes	72
10.5 Diamond nuclear spin gyroscope	73
10.5.1 The experimental setup description .....	73
10.5.2 Rotation detection principle.....	74
10.5.3 Measurement protocol description.....	75



<b>11. Acceleration measurement using NV-center sensors .....</b>	<b>77</b>
11.1 Spin-based acceleration measurement	77
11.2 Sensing mechanism of spin-based acceleration measurement	77
11.3 Sensitivity optimization of acceleration measurement	79
11.4 Hybrid opto-mechanical systems with nitrogen-vacancy centers. Atomic accelerometers	80
11.4.1 Inertial sensing technology based on levitated optomechanics .....	80
11.4.2 Magnetic field gradient induced coupling .....	81
11.4.3 Applications as resonator cooling .....	82
11.4.4 Applications in quantum information processing .....	82
11.4.5 Applications in ultra-sensitive measurement .....	83
<b>12. Magnetometer prototypes and commercially available magnetometers on NV-centers.....</b>	<b>85</b>
12.1 Integrated magnetometers prototypes	85
12.2 The diamond magnetic microscope imaging schemes	88
12.3 Applications of NV centers to sensing the inhomogeneities, deformations, stress and strain in crystal.	90
12.4 Nanodiamond for in vivo sensing and cell tracking applications	90
12.5 Companies that offer magnetometers on NV centers, quantum diamond microscopes or quantum diamond microscope tips	91
12.5.1 WAINVAM-E (Ploemur in the west region of France).....	91
12.5.2 QZabre (Zurich, Switzerland).....	98
12.5.3 Qnami AG (Switzerland) .....	100
<b>13. Bibliography .....</b>	<b>102</b>



## List of figures

Figure 1. Phase diagram for carbon. Sources: [15], [16].	13
Figure 2. The technological processes of diamond synthesis by HPHT and CVD methods. Sources: [17], [18].	14
Figure 3. NV center schematic diagram. Source: [16].	15
Figure 4. Experimental ODMR spectra for different bias magnetic field magnitudes and orientations.	19
Figure 5. NV-center lattice structure and electron density	19
Figure 6. Characteristics of the nitrogen-vacancy (NV) center.	20
Figure 7. NV structure, energy levels, electron spin resonance.	21
Figure 8. NV ground-state configurations and ODMR Spectra.	22
Figure 9. Energy level diagram for the NV– ground-state spin in the presence of an axial magnetic field.	25
Figure 10. Weak magnetic field regime.	28
Figure 11. Strong magnetic field regime.	29
Figure 12. Overview of CW-ODMR, pulsed ODMR and Ramsey magnetometry protocols	32
Figure 13. Bloch sphere depiction of Ramsey sequence.	34
Figure 14. Ramsey free induction decay and Ramsey magnetometry curve	34
Figure 15. Sensing techniques and protocols	36
Figure 16. Double-quantum (DQ) coherence magnetometry	37
Figure 17. Spin-to-charge conversion (SCC) readout.	38
Figure 18. Ancilla-assisted repetitive readout.	40
Figure 19. Geometric phase magnetometry	42
Figure 20. NV measurement protocols. Source: [32].	43
Figure 21. Spin-phonon relaxation time.	44
Figure 22. Hahn echo pulse scheme and graph.	45
Figure 23. Dephasing time scheme and example graph.	46
Figure 24. Typical coherence times of single NV defect electron spins	47
Figure 25. Microwave sources	57
Figure 27. Optics for illumination and fluorescence collection	60
Figure 28. Camera sensor operation.	61
Figure 29. Basic schematic of an inertial navigation system. Source: [97].	65
Figure 30. The “Dark Ice” quantum magnetometer. Source: [102].	67
Figure 31. Mechanism diagram of NV-based rotation measurement.	70
Figure 32. Schematic of rotation measurement.	71
Figure 33. Principle of the rotating test bench.	71
Figure 34. Diamond nuclear spin gyroscope experimental setup.	74



Figure 35. Nuclear spin gyroscope measurement protocol ..... 75

Figure 36. Spin-oscillator coupling acceleration sensing schemes based on NV center. .... 78

Figure 37. Magnetic coupling between a mechanical oscillator and a NV center..... 81

Figure 38. Multiple NV centers spins that couple with mechanical oscillator ..... 82

Figure 39. Schematic view of a scalable quantum information processor on an electromechanical quantum bus and NV centers spins as qubits. Source: [143]...... 83

Figure 40. A hybrid system in which a single nitrogen-vacancy center coupled with a nanomechanical oscillator..... 83

Figure 41. The hand-held magnetometer ..... 85

Figure 42. Miniaturised and integrated magnetometer based on NV- centers. .... 86

Figure 43. CMOS-integrated quantum sensing architecture..... 86

Figure 44. The hybrid fiber-optical thermometer setup ..... 87

Figure 45. Fiber magnetometer mechanism..... 87

Figure 46. Wide-field magnetic imaging fluorescence microscope used for combined optical and magnetic imaging..... 88

Figure 47. Principle of scanning-NV magnetometry which combines an atomic force microscope (AFM) and a confocal microscope..... 89

Figure 48. Schematic of the combined NV stress and birefringence imager..... 90

Figure 49. The prototype of NV center magnetometer for detecting magnetic nanoparticles in biomedical applications ..... 91

Figure 50. Low Field NV Magnetometer WAINMAG-LF. Source: [165]. ..... 92

Figure 51. Wide Field NV Imager WAINIM-WF. Source: [166]. ..... 93

Figure 52. High Field NV Magnetometer WAINMAG-ST. Source: [167]. ..... 94

Figure 53. Microwave Generator WAINVAM-MW-GEN01. Source: [168]. ..... 95

Figure 54. QZabre quantum sensor tip. Source: [171]..... 98

Figure 55. QZabre Quantum Scanning Microscope. Source: [172]. ..... 99

Figure 56. QZabre QSM system. Source: [172]. ..... 100



## List of tables

<b>Table 1.</b> HPHT and CVD technology comparison .....	14
<b>Table 2.</b> Comparison of the fluorescent properties of organic dyes, colloidal quantum dots, and single nitrogen-vacancy (NV) centers in nanodiamonds. Abbreviations: IR-UV – infrared-ultraviolet; FWHM – full width at half maximum Source [4].....	16
<b>Table 3.</b> Compiled constants for the electronic ground state of the NV <sup>-</sup> center in diamond. Source [38].....	24
<b>Table 4.</b> Operational regimes and selected applications of broadband DC and AC sensing protocols employing NV <sup>-</sup> ensembles in diamond. Source: [38]. .....	43
<b>Table 5.</b> Summary of diamond sample parameters. Source: [68]. .....	47
<b>Table 6.</b> The best sensitivities achieved with sensors on NV centers. ....	48
<b>Table 7.</b> Summary analysis of diamond engineering parameters and methods for high-sensitivity ensemble-NV <sup>-</sup> magnetometry. Colored lines indicate methods that may be employed to optimize each parameter. Source: [38]. .....	51
<b>Table 8.</b> Dephasing time $T_2^*$ optimization. Source: [38]. .....	55
<b>Table 9.</b> Readout fidelity optimization $F=1/\sigma_R$ . ( $\sigma_R = 1$ corresponds to readout at the spin-projection limit.). Source: [38].....	55
<b>Table 10</b> Summary of microwave antenna parameters. Source: [68]......	58
<b>Table 11.</b> Camera sensor parameters used for determination of achievable SNR and magnetic field sensitivity. Source: [94] .....	61
<b>Table 12:</b> General hardware considerations that apply to all measurement techniques. Source: [32] .....	63
<b>Table 13.</b> Comparison in sensitivity and size of some representative gyroscopes and the NV- based gyroscope [99].....	72
<b>Table 14.</b> The parameters of the magnetometer WAINMAG-LF. Source: [165]. .....	92
<b>Table 15.</b> The parameters of the wide field NV imager WAINIM-WF. Source: [166]....	93
<b>Table 16.</b> The parameters of the High Field NV Magnetometer WAINMAG-ST. Source: [167]. .....	94
<b>Table 17.</b> Specifications of microwave generator WAINVAM-MW-GEN01. Source: [168]. .....	95
<b>Table 18.</b> Absolute maximum ratings of microwave generator WAINVAM-MW-GEN01. Source: [168]. .....	96
<b>Table 19.</b> The parameters of the WAINVIEW confocal NV microscope. Source: [169]. .....	96
<b>Table 20.</b> The parameters of the WAINVIEW relaxometer. Source: [170].....	97



## Abbreviations:

AC – alternating current  
ADC – analog-to-digital converter  
AFM – atomic force microscope  
AOM – acousto-optical modulator  
APD – avalanche photodiode  
CCD – charge-coupled device  
CMOS – complementary metal–oxide–semiconductor  
CoM – center of mass  
CPC – compound parabolic concentrator  
CVD – chemical vapour deposition  
CW-ODMR – continuous-wave optically detected magnetic resonance  
DC – direct current  
DND – detonation nanodiamonds  
DQ – double-quantum  
EPR – electron paramagnetic resonance  
ESR – electron spin resonance  
FCR – fidelity of the charge readout  
FF – fill factor  
FID – free induction decay  
FPS – number of frames that a camera is able to capture per second  
FSCC – fidelity of the Spin-to-charge conversion  
FWHM – full width at half maximum  
FWC – full well capacity  
GPS – global positioning system  
HPHT – high-pressure high-temperature  
IMU – inertial measurement unit  
INS – inertial navigation systems  
IR – infrared  
ISC – spin selective intersystem crossing  
LED – light-emitting diode  
LIA – lock-in amplifier  
ML – machine learning  
MPCVD – microwave plasma-activated chemical vapour deposition  
MTB – magnetostatic bacteria  
MW – microwave  
NA – numerical aperture  
NMR – nuclear magnetic resonance  
NV center – nitrogen-vacancy center





ODMR – optically detected magnetic resonance  
PBS – phosphate-buffered saline  
PD – photodiode  
PL – photoluminescence  
ppb – part per billion atoms  
ppm – part per million atoms  
QDM – quantum diamond microscope  
QE – quantum efficiency  
RF – radiofrequency  
SCC – spin-to-charge conversion  
SCD – single crystal diamonds  
SEM – scanning electron microscopy  
SIL – solid immersion lens  
SNR – signal-to-noise ratio  
SQ – single-quantum  
 $T_1$  – longitudinal spin relaxation time  
 $T_2$  – coherence time  
 $T_2^*$  – dephasing time  
TEM – transmission electron microscope  
TIR – total internal reflection lens  
UV – ultraviolet  
ZPL – zero phonon line



## 1. DIAMOND CLASSIFICATION

Diamond is known as the hardest natural mineral. It is one of the allotropes<sup>1</sup> of carbon. Other known allotropes of carbon are graphite, graphene, buckminsterfullerene, and carbon nanotubes.

It can be classified in several different ways [1] according to:

1. Optical absorption
2. Defects
3. Synthetic growth methods
4. Crystallite size

Next each of the classification methods will be present in more details.

### 1.1 Classification by types according to their optical absorption

The optical absorption of diamonds varies depending on the types and concentrations of impurities present in the diamond. One of the first proposed principles for the classification of diamonds is the differentiation of four main types according to their optical absorption [1]:

- Type I. The main impurity of diamonds of this type are nitrogen atoms in concentrations of 100-1000 ppm. This type of impurities is the most common.
  - Type Ia: this type of diamond also contains clustered nitrogen impurities; the concentration of nitrogen is up to 0.3% (3000 ppm). It has a characteristic yellow color due to the absorption of the blue part of the spectrum by nitrogen impurity atoms. This type is the most common and makes up to 98% of all natural diamonds.
  - Type Ib: diamonds of this type contain nitrogen atoms in an isolated form: some of the carbon atoms in the crystal lattice are replaced by nitrogen atoms. In nature, diamonds of this type are much rarer than type Ia diamonds and make up only about 0.1% of all natural diamonds. But almost all high pressure high temperature (HPHT) synthetic diamonds are of this type. Diamonds of this type have a darker yellow or brown color due to the absorption of both blue and green parts of the spectrum by impurities.
- Type II. Diamonds of this type contain almost no nitrogen impurities. They are formed under extreme pressure conditions for a long time.
  - Type IIa: these diamonds have a very small proportion of nitrogen impurities (less than 5 ppb of nitrogen atoms) and, as a result, have no optical absorption, which makes them almost colorless. Due to the high pressure and high tension these diamonds were subjected to during their formation, they contain structural deformations that can be corrected during the HPHT process. In nature, diamonds of this type are more common than type Ib diamonds, but do not make up more than 1-2%.
  - Type IIb: diamonds of this type make up only 0.1% of natural diamonds and are the rarest and most valuable. There are practically no nitrogen impurities in them, but boron impurities are present in significant amounts, due to which they acquire the properties of a p-type semiconductor. Boron impurities absorb yellow, orange, and red light, making these diamonds appear light blue or grey.

---

<sup>1</sup> An allotrope is the different forms that an element or molecule can present.



## 1.2 Classification by defects

A diamond can contain several hundred types of various defects. Nitrogen impurities in various configurations are the most common. Apart from nitrogen, both natural and artificial diamonds may contain impurities of boron, silicon, phosphorus, hydrogen, nickel, and cobalt [1].

Along with NV centers, which are currently the subject of a large amount of research, many other diamond color centers are known, some of which are also characterized by magnetic resonance from electronic spin states, spin-dependent fluorescence and similar to NV centers optical transitions.

In particular, the potential of using silicon vacancy ( $\text{SiV}^-$ ), which has an electronic spin 1/2 system and strong zero phonon line at  $\lambda=737$  nm ( $E=1.68$  eV), has recently been explored [2], [3].

Other types of internal defects in diamond are such violations of the crystal structure as stress, dislocations, clusters of vacancies or isolated vacancies or platelets [1].

## 1.3 Classification by synthetic diamond growth methods

Except for the extraction of natural diamonds, there are various methods for the artificial diamond synthesis [1]:

### 1. High-pressure high-temperature (HPHT) diamond

The essence of the HPHT method is an attempt to recreate in the laboratory the conditions that exist inside the earth's mantle, under which natural diamonds are formed. Diamonds synthesized by HPHT method typically contain nitrogen concentrations more than 100 ppm. But recently, methods have also appeared for obtaining pure HPHT diamonds with a nitrogen concentration of less than 0.1 ppm.

### 2. Chemical vapour deposition (CVD) diamond

CVD diamond is synthesized in a vacuum chamber, which form a microwave cavity and produce a plasma mixture of methane ( $\text{CH}_4$ ) and hydrogen gases ( $\text{H}_2$ ). In this case, in contrast to the HPHT method, diamond synthesis occurs under non-equilibrium conditions. It is possible to obtain isotopically pure CVD-diamond if a methane source  $^{12}\text{CH}_4$  is used.

### 3. Shock wave synthesis

Shock wave synthesis diamonds are obtained by controlled detonation in a closed vessel, and the carbon contained in the explosives is the source material. Diamonds obtained by this method have a diameter of several nanometres.

## 1.4 Classification by crystallite size

Diamonds can be classified according to the size of the crystals into the following types [1]:

1. Single crystal diamonds (SCD) can have grain sizes of over 500  $\mu\text{m}$ .
2. Polycrystalline diamonds have grain sizes between 50 nm and 500  $\mu\text{m}$ .
3. Nanocrystalline diamonds have grain sizes below 50 nm.



## 2. DIAMOND SYNTHESIS

As a rule, synthetic diamonds are used to create sensors based on NV centers. Natural diamonds are not well suited for magnetometry and related research because they are characterized by non-standard sizes, uncontrolled impurity concentrations and output.

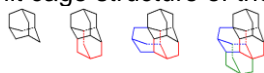
### 2.1 Types, forms and sizes of synthesized diamonds

Synthetic diamonds exist in the forms of bulk crystals, thin films and nanocrystals [4].

- a. The smallest diamonds (<1 nm), so-called diamondoids<sup>2</sup> are extracted from crude oil. However, they cannot provide stable fluorescent defects inside the lattice due to their too small size [4].
- b. Detonation nanodiamonds (DNDs) are the next largest type of nanoparticles, measuring 4–5 nm in size. DND is synthesized by controlled detonation in a closed vessel of trinitrotoluene-like explosives [5]. The resulting particles have a  $sp^3$  core, which is surrounded by a shell of several  $sp^2$  carbon atoms. Diamonds obtained in this way are well suited for applications in biology due to their small size and monodispersity. However, such diamonds contain a lot of  $sp^2$ -like carbon and are difficult to deaggregate. To clean the surface of the obtained particles from undesirable  $sp^2$  residues, procedures are used based on the selective oxidation of  $sp^2$  carbon compared to the more stable  $sp^3$  carbon [6]. DND-like nanodiamonds are also obtained using pulsed laser ablation, which allows better control of the reaction conditions [7].
- c. Another way to obtain nanodiamonds can be the grinding of larger crystals to particles with a size of < 100 nm. After grinding, such particles are sorted by size using ultracentrifugation and dynamic light scattering [8]. Such diamonds are much purer than those obtained by the DND method. However, the disadvantage of this method of obtaining nanodiamonds is their relatively large size, as well as an irregular, jagged shape. The smallest average particle size of commercially available nanodiamond powders is around 15 nm, and research initiatives have produced particles up to 5 nm in diameter [9].
- d. Currently, the most widely used method for the synthesis of diamonds is the chemical vapor deposition (CVD) method. Growing crystals by CVD makes it possible to control the concentration of impurities and the isotopic composition of carbon, which makes it possible to obtain samples of purer diamonds based on  $^{12}\text{C}$  and to increase the dephasing time parameter  $T_2^*$ , important for magnetometry, which is strongly influenced by the nuclear spin of  $^{13}\text{C}$  [10]. In addition, in CVD diamonds it is possible to obtain NV centers oriented in a certain way [11], [12].
- e. Another well-known method of diamond synthesis is the method of high pressure and high temperature (HPHT). When growing diamonds with the conventional HPHT method, catalysts such as iron, cobalt or nickel are needed. As a result, the diamonds obtained by this method are characterized by a high nitrogen concentration and a large amount of magnetic impurities, which shortens the dephasing time  $T_2^*$  [13]. This makes it impossible to use diamonds obtained by conventional HPHT technology for NV center sensing applications. Compared with them, however, diamonds produced by new, modified HPHT processes show significantly better performance. They have fewer irregularities and can reach the same impurity concentration as CVD diamonds [14].

---

<sup>2</sup> Diamondoids are variants of the carbon cage molecule known as adamantane ( $\text{C}_{10}\text{H}_{16}$ ), the smallest unit cage structure of the diamond crystal lattice



Examples: [Wikipedia]

## 2.2 Features of the CVD method in comparison with the HPHT method

The areas of temperature-pressure space favourable for diamond growth are represented in the carbon phase diagram, which is shown in Figure 1. The area of the carbon phase diagram in which diamond is thermodynamically stable corresponds to conditions that exist at depths of about 200 km (temperature of about 1400-1600°C, pressure 70 -80 kbar) where natural diamonds are thought to originate. As can be seen from the diagram, under room conditions the stable allotrope of carbon is graphite, while the diamond is metastable [15].

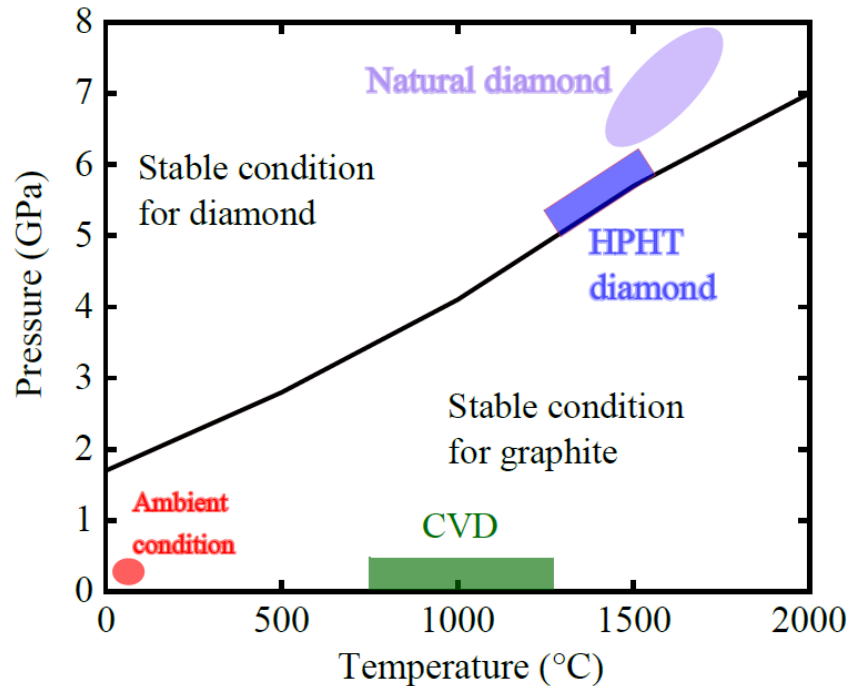


Figure 1. Phase diagram for carbon. Sources: [15], [16].

Since the growth of CVD diamonds occurs in a metastable mode (in contrast to the stable mode of growing HPHT diamonds), the process of CVD synthesis is regulated not by thermodynamics, but by kinetics. The substrate for the growth of CDV diamonds is a seed crystal, which is placed on a heater inside the growth chamber and heated to a temperature of 700–1300°C, maintaining a pressure of about 30 mbar. To create the conditions necessary for diamond growth, with the help of MW radiation of the order of several hundred Watts, a plasma of a mixture of gaseous reagents – hydrogen  $H_2$  and a small percentage (0,5% - 5%) of methane  $CH_4$  – is formed in the growth chamber, which promotes the activation of the diamond synthesis process. The described process is called microwave plasma-activated chemical vapor deposition (MPCVD) [16].

Gradually heated by MW radiation, the gas mixture in the growth chamber turns into plasma, forming highly reactive atomic hydrogen H, capable of etching unwanted graphite (stable allotrope of carbon) from the diamond surface and forming dangling carbon bonds ending with a carbon atom of the  $CH_3$  radical, also obtained from plasma, or with hydrogen atom. The quality of the resulting diamonds can be improved by using deuterium instead of hydrogen in the gas mixture [16].

Thus, CVD technology, in comparison with HPHT method, makes it possible, due to the possibility of the strict control of the isotopic initial gas mixture composition, to obtain very pure and high-quality diamonds, which are mainly of type IIa. At present, diamond samples containing up to 99.999% of  $^{12}C$  isotope atoms and only 4 ppb of nitrogen atoms are available and used in experimental sensors based on NV centers [16].

Figure 2 schematically shows the technological processes of diamond synthesis by HPHT and CVD methods. The difference between these two methods is summarised in the table 1 [17], [18], [19].

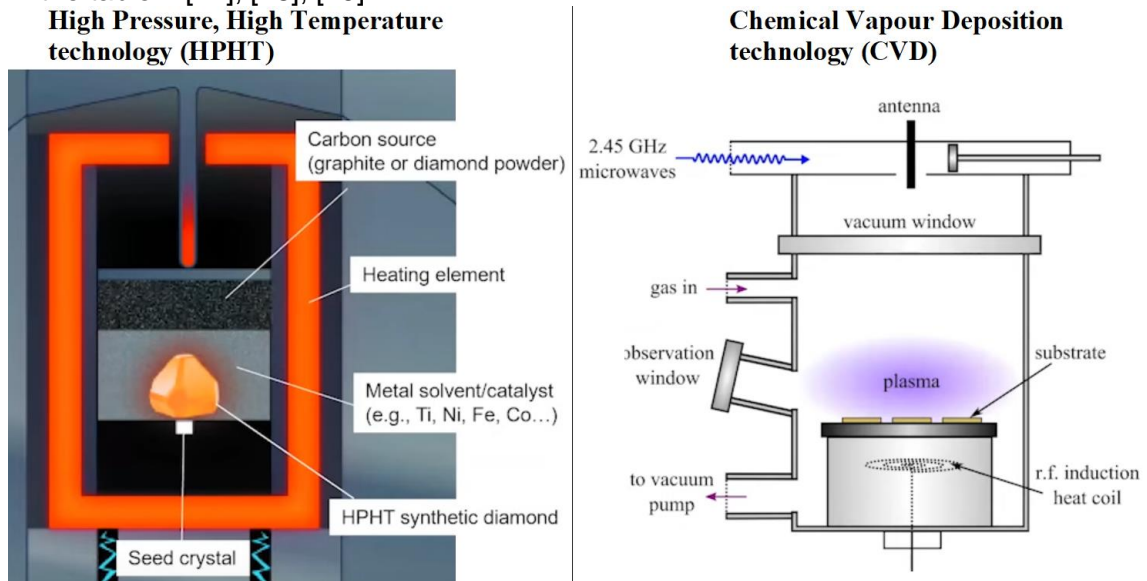


Figure 2. The technological processes of diamond synthesis by HPHT and CVD methods. Sources: [17], [18].

**Table 1.** HPHT and CVD technology comparison

	<b>HPHT technology</b>	<b>CVD technology</b>
<b>Regime of phase transition</b>	stable, governed by thermodynamics	metastable, governed by kinetics
<b>Process description</b>	HPHT press used for grows, which mimic key conditions of natural diamond growth	gas-phase chemical reaction
<b>Environmental characteristic</b>	metal solvent/catalyst are added (e.g. Ti, Ni, Fe, Co)	the mixture of H <sub>2</sub> and 0.5% – 5% of CH <sub>4</sub> is heated up by the microwave radiation, and turns into a plasma above diamond substrate
<b>Pressure</b>	~ 5 – 6 GPa	~10-200 torr (1/20 – 1/4 atm)
<b>Temperature</b>	~ 1300 – 1600 °C	~700 – 1000 °C
<b>Duration</b>	~ days – weeks	~ days - weeks
<b>Power consumption</b>	175–225 kWh per rough ct.	60–120 kWh per rough ct.

### 3. NITROGEN-VACANCY CENTERS IN DIAMOND

#### 3.1 What is an NV center in diamond?

Nitrogen atoms are about the same size as carbon atoms. Impurities of nitrogen atoms inside the diamond lattice have specific absorption lines or bands, which cause the different colors of diamond.

One of the varieties of such color centers in a diamond crystal is a nitrogen vacancy (NV) center, a point defect with  $C_{3v}$  symmetry. The NV center consists of a nitrogen atom replacing one of the carbon atoms in a diamond lattice site and a vacancy in a nearby lattice site. The axis connecting the substituting nitrogen atom and the vacancy is the axis of symmetry of the nitrogen-vacancy center (Figure 3).

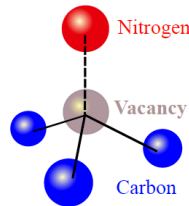


Figure 3. NV center schematic diagram. Source: [16].

Apart from negatively charged ( $NV^-$ ), neutral ( $NV^0$ ) and positively charged ( $NV^+$ ) nitrogen vacancy centers are known, but it is specifically negatively charged NV centers have properties that allow them to be used in quantum information processing and quantum sensing.

The following five key properties of NV centers can be distinguished, each of which, individually or in combination, are used by various applications of NV centers [20]:

1. Ability to generate single photons and detect individual centers due to the photostable and bright optical transition.
2. The presence of a fine structure of the optical zero phonon line (ZPL), which depends at room temperature on the magnetic field, and at low temperatures also on the electric field and the strain field.
3. Controllable ground state magnetically resonant electronic spin, which has a long coherence time and is coupled with neighbouring nuclear and electronic spins.
4. Possibility of the optical ground state spin polarisation and readout
5. Manufacturing reliability and flexibility.

The unique properties of NV centers allow them not only to be used as nanoscale multisensors sensitive to many physical quantities or spin qubits in quantum information processing, but also to act as a photostable source of single photons in quantum cryptography or to be the object of fundamental experiments necessary for the development of quantum theory and the theory of condensed state. In particular, the NV center was proposed [21] as an ideal system for studying such mesoscopic quantum effects as entanglement of NV spin qubits separated by mesoscopic distances using a magnetic micromechanical cantilever or, as a variant, entanglement between cantilever vibrations and NV spin qubit. Sections 9 to 12 will provide a more detailed description of the different NV centres applications.

#### 3.2 Generation of fluorescent defects

As a rule, the natural concentration of NV centers found in most diamonds is insufficient for applications. For example, only 1 out of 1000 nanodiamonds from commercial powders with an average particle size of about 25 nm actually contains an NV center [6]. To increase the concentration of NV centers, high-energy irradiation with electrons or  $N^+$



ions is used (which promotes the formation of vacancies and, if necessary, an increase in the concentration of nitrogen atoms in diamond) followed by annealing at temperatures  $\geq 800^\circ\text{C}$  (during which vacancies migrate, forming NV centers). The described procedures ensure the conversion of nitrogen to NV centers with an efficiency of about 10%, which makes it possible to obtain several NV centers in a 10-nm particle and corresponds to the density of tens of parts per million [9]. Apart from the use of ion implantation [22], [23], additional nitrogen concentrations can be introduced through deliberate doping during the growth of CVD diamonds [24]. Both of these methods make it possible to create near-surface NV centers with a depth of up to 5 nm, which is important for the sensitivity of sensors based on them [25], [26].

During research, it is important to consider that in some cases the samples may exhibit fluorescence that is not associated with diamond. The amorphous carbon or graphite shells on the nanodiamond surface can create fluorescence as well as actively quench the fluorescence from color centers [27]. This behavior is especially characteristic of DND diamonds, whose surface fluorescence can significantly exceed the fluorescence from color centers [28]. Table 2 summarizes the comparative information on the fluorescent properties of nanodiamonds, typical organic dyes and quantum dots.

**Table 2.** Comparison of the fluorescent properties of organic dyes, colloidal quantum dots, and single nitrogen-vacancy (NV) centers in nanodiamonds. Abbreviations: IR-UV – infrared-ultraviolet; FWHM – full width at half maximum Source [4].

Property	Typical organic dye (20)	Quantum dot (20)	Nanodiamond (NV center)
Size	<1 nm	3–10 nm	>4 nm
Emission spectrum	IR-UV	IR-UV, selected by size	Fixed at approximately 630–800 nm
Emission line width (FWHM)	35–100 nm	30–90 nm	>100 nm
Absorption cross section	Typically $1 \times 10^{-16} \text{ cm}^2$	Typically $3 \times 10^{-15} \text{ cm}^2$	$3 \times 10^{-17} \text{ cm}^2$
Quantum yield	0.5–1.0	0.1–0.8	0.7–0.8
Lifetime	1–10 ns	10–100 ns	25 ns
Photostability	Low	High	Extremely high
Thermal stability	Low	High	Extremely high
Toxicity	From low to high	Not well known	Low

### 3.3 Properties of the diamond chip and fluorescent defects that impact sensing performance

In the process of diamonds preparation, it is necessary to control the following properties of the diamond chip, which strongly affects the sensing performance [29], [30] [31]:

- The impurity color centers concentration
- The nitrogen atom concentration
- The NV centers concentration
- The proportion of  $^{13}\text{C}$  isotopes (their natural concentration is 1.1%)
- The stress uniformity
- The particle size

For example, in magnetometry applications, to obtain the highest quality visualization of a thin two-dimensional magnetic sample, it is necessary that the thickness of the NV layer is comparable to the thickness of the magnetic sample and for quantum diamond microscopes (QDM) it lies in the range from ~10 nm to ~100  $\mu\text{m}$  [32].





### 3.3.1 *Methods to make NV layers of varying thickness*

To create layers with an increased concentration of NV centers, the following methods are used:

1. Pure type IIa diamonds with an impurity density of the order of several ppb are subjected to ion implantation with  $N^+$  or  $N_2^+$  ions followed by high-temperature annealing. This method makes it possible to obtain near-surface NV layers at depths of 10–100 nm. Annealing at temperatures of 800–1200 °C increases the efficiency of the conversion of nitrogen atoms into negatively charged NV centers and significantly increases the coherence time parameter  $T_2$ , which is important for sensing performance [33].
2. Formation of a natural NV layer directly during the CVD growth of diamond, which also makes it possible to control the orientation of the axis of the grown NV centers and double the sensitivity of the sensors obtained on their basis, compared to sensors in which all four possible NV orientations are present. But the density of the NV centers obtained by this method and, as a result, the fluorescence yield will be lower [34].
3. Growing a nitrogen-rich layer with a depth of several micrometers to several nanometers by CVD on pure type IIa diamond substrates, followed by high-energy electron irradiation, which stimulates the formation of vacancies, and annealing, which improves the NV yield to 10% efficiency. However, the layers thus obtained contain NV centers oriented in different directions [23], [25].
4. Delta doping: on a pure type IIa diamond substrate, a nitrogen-enriched layer several nanometers thick is grown using CVD method by temporarily increasing the nitrogen concentration in the growth chamber, on top of which a pure diamond layer is grown. Then, by irradiation with high-energy electrons and annealing, vacancies are formed and NV centers are created. This method creates samples with an additional cap layer of pure diamond, which increases the distance from the sensitive layer to the object, that may be required in rare cases for some specific applications [24].
5. Formation of a shallow NV layer in HPHT diamond by ion implantation and annealing or use of HPHT diamonds with a uniform bulk density of NV centers cut into 35-micron layers [13].

### 3.3.2 *NV centers, isotopes and impurity concentration*

A high density of NV centers gives a high fluorescence intensity and good photon shot noise, but this occurs due to an increase in magnetic inhomogeneity, to which paramagnetic nitrogen impurities contribute, and, as a result, an increase in the optically detected magnetic resonance (ODMR) linewidth, which worsens the optical contrast sensitivity to magnetic field. These two factors must be balanced to obtain optimal sensitivity. In addition, when creating an NV layer, it is necessary to take into account the conditions that favor the formation of negatively charged  $NV^-$  centers, since neutrally charged  $NV^0$  centers also contribute to the background fluorescence, worsening the contrast used for the imaging [35].

Also, a very important factor is the isotopic composition of carbon and nitrogen atoms of the samples used for measurements.

The atoms of the  $^{13}C$  carbon isotope whose spin is 1/2 present in the diamond as well as paramagnetic defect centers make a negative contribution to the decrease in the dephasing time parameter  $T_2^*$ . Therefore, isotopically purified diamonds grown on the basis of the  $^{12}C$  carbon isotope, which has a nuclear spin of 1, are ideal for applications in magnetometry. In the case of using diamonds with a natural content of the  $^{13}C$  carbon isotope (1.1%), it makes sense to increase the nitrogen density more and, as a consequence, the density of sensitive NV centers, since their contribution to the increase

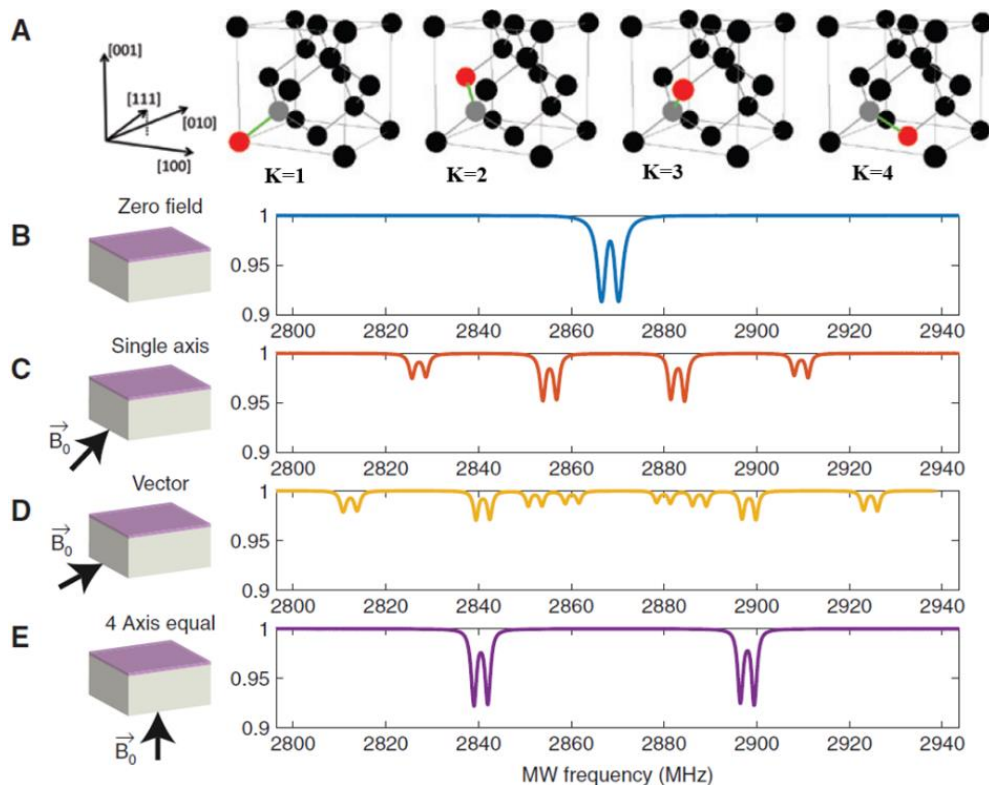


in the ODMR linewidth will not be predominant. Also, in the case of very shallow NV layers (less than 10 nm deep), magnetic inhomogeneity caused by near-surface phenomena can neutralize the advantages of isotopically purified  $^{12}\text{C}$  diamond and make its use irrelevant [32].

Diamonds produced without special isotope control procedures are characterized by the predominant content of the  $^{14}\text{N}$  isotope (having a nucleus with spin 1), which is more common in nature, but gives less contrast in the ODMR spectrum and requires a larger range of MW probe frequencies than the  $^{15}\text{N}$  isotope, which has a nucleus with spin 1/2 [32].

### 3.3.3 Synthetic diamond chips cuts

Typically, the choice of diamond cut does not affect the performance of fabricated sensors. Synthetic diamonds are available in various cuts (Figure 4), among which the most common are diamonds with lateral faces along the [100] and [110] planes or with an upper facet along the [100] plane, when the angle of inclination of the NV center axis to the plane is approximately  $35^\circ$ . In the less common [111] plane cut, the NV center is directed perpendicular to the face, while in the [110] plane cut, there are two NV orientations in the plane. Other, rarer facets are also possible, for example, along a plane [113] [36]. The method of treatment of the diamond can have a significant impact on the characteristics of the resulting sensors. Also, different cuts of diamonds are characterized by different prices and availability due to the different complexity of their production, which increases if the crystals are not grown along the preferential growth axis of diamonds. [32].



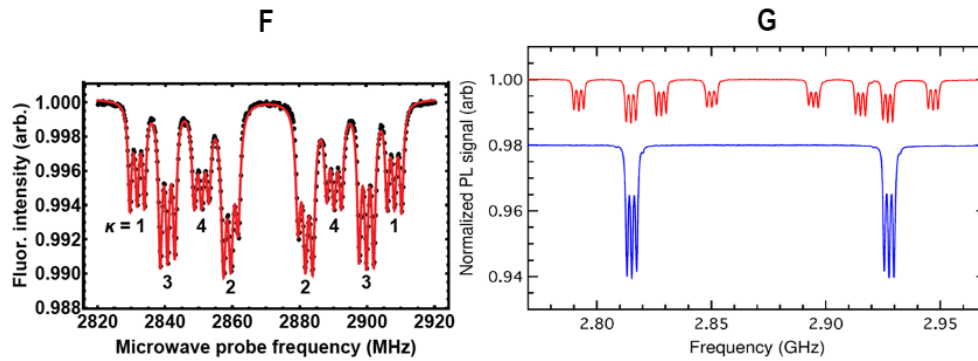


Figure 4. Experimental ODMR spectra for different bias magnetic field magnitudes and orientations.

(A) Example of four possible NV orientations in the diamond lattice, and the crystallographic directions. The four N-V axes shown in green, carbon atoms are black, nitrogen atoms are red, and vacancies are gray. (B) Example ensemble NV ODMR spectrum with  $|\mathbf{B}_0| = 0$ . The resonance is centred at  $\sim 2.87$  GHz, but splits into two peaks around this resonance frequency because of the  $^{15}\text{N}$  hyperfine coupling. Strain and electric field also contribute to the ODMR lineshape and broadening and can cause a variety of lineshapes at  $|\mathbf{B}_0| = 0$  for different samples. (C) Ensemble NV ODMR spectrum with  $|\mathbf{B}_0|$  pointing along one axis. The frequency separation between the outer resonance peaks is proportional to the applied field. The inner peaks are from the three other NV orientations overlapping with each other due to equal Zeeman interactions for each. The  $^{15}\text{N}$  hyperfine interaction again splits each resonance into a doublet. (D) Ensemble NV ODMR spectrum with  $|\mathbf{B}_0|$  orientation such that each axis has a different projection of bias field. (E) Ensemble NV ODMR spectrum with  $|\mathbf{B}_0|$  along the [001] direction, such that each NV orientation has the same Zeeman interaction. The peak separation is proportional to the  $|\mathbf{B}_0|$  field projection along the NV axes. (F) Example ODMR spectrum with  $\mathbf{B} = \{220; 593; 1520\}$   $\mu\text{T}$  in the diamond chip coordinate system (fit function plotted in red). The labels indicate the resonances from the different NV orientations. Each NV resonance is split into three lines due to hyperfine interactions with the spin-1  $^{14}\text{N}$  nucleus. (G) Example ODMR spectra from the same NV-ensemble in different applied bias magnetic fields. A bias field with a different projection on each of the four NV- crystallographic orientations separates the  $m_s = 0 \leftrightarrow m_s = \pm 1$  spin resonances into distinct groups (red). A bias field that projects equally onto all four orientations overlaps the spin resonances (blue, offset for clarity). Sources: A – E [32], F – [37], G – [38].

### 3.4 NV center electronic structure

The NV center has an electronic structure consisting of six electrons. The nitrogen atom provides two electrons, three another are dangling bonds of carbon atoms surrounding the vacancy, and one more electron the NV center captures from the lattice, which is usually given by nitrogen donors, making NV center charge state negative ( $\text{NV}^-$ ). The electronic density is maximum at three carbon atoms and in the area of the vacancy and is located mainly in the plane perpendicular to the NV center axis [4] [39], [40] (Figure 5).

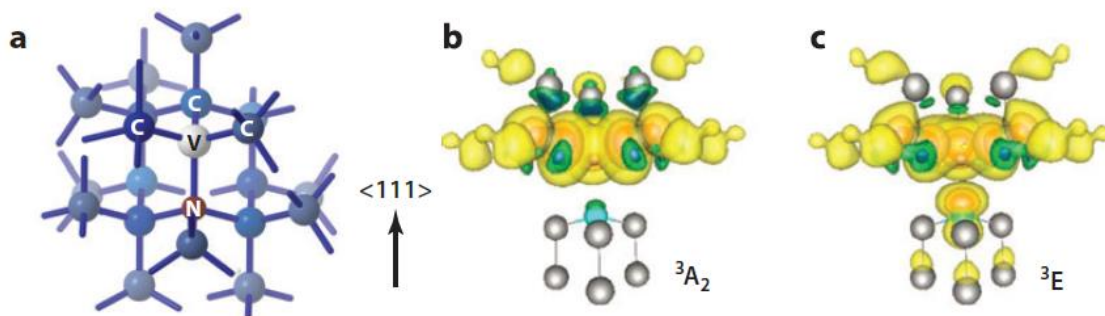


Figure 5. NV-center lattice structure and electron density

(a) Lattice structure of the nitrogen-vacancy center. (b, c) Three-dimensional electron density of the  $^3\text{A}_2$  electronic ground state and the  $^3\text{E}$  excited state Sources: [4], [39].

### 3.5 NV center optical properties

The remarkable optical properties of the NV center are determined by the arrangement of electronic levels in its energy diagram (Figure 6 a and Figure 7). The electronic system of the NV center is characterized by spin  $S=1$ , which leads to the appearance of two triplets: the ground state triplet  $|g\rangle$  with  ${}^3A_2$  symmetry and the excited state triplet  $|e\rangle$  with  ${}^3E$  symmetry. There is also a singlet state  $|s\rangle$ , which is very important for numerous applications of NV centers due to the possibility of selective intersystem crossing (ISC), consisting of two levels with  ${}^1A_1$  and  ${}^1E$  symmetries. The transition between the ground and excited states  $|g\rangle \leftrightarrow |e\rangle$  has a resonant zero phonon line (ZPL) at 637 nm. It is effectively excited at wavelengths less than 640 nm. However, most of the luminescence falls on the side vibrational bands in the range from 630 to 800 nm while the radiation corresponding to ZPL accounts for only a few percent (Figure 6 b) [4]. Depending on the spin state, approximately 70–80% of the excited electrons decay through the radiative transition  $|e\rangle \rightarrow |g\rangle$ , which determines the quantum yield of the system. The lifetime of the metastable singlet state is 250 ns and exceeds by an order of magnitude or more the lifetime of the excited state  $|e\rangle$ , which depends on the refractive index and can vary from 13 ns for NV centers in bulk diamond to 25 ns for nanodiamonds [20].

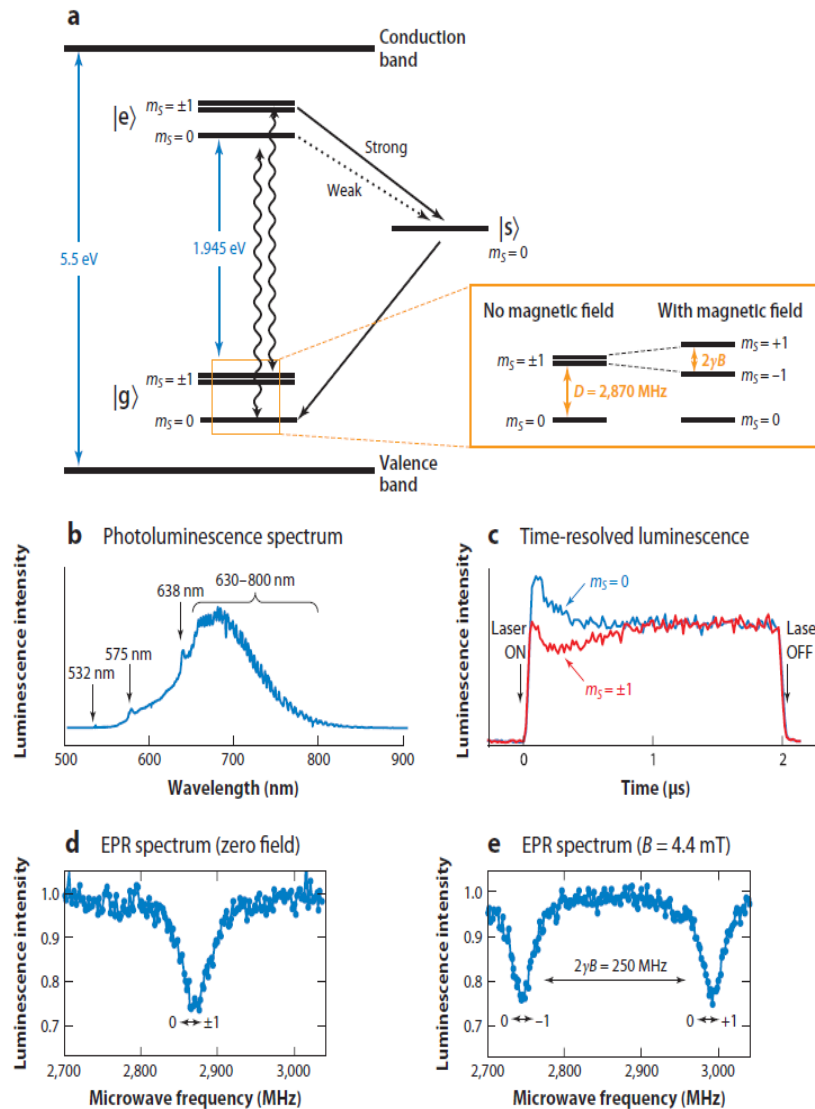


Figure 6. Characteristics of the nitrogen-vacancy (NV) center.

(a) Energy-level diagram of NV<sup>-</sup>.  $|g\rangle$  denotes the electronic ground state,  $|e\rangle$  the electronic excited state, and  $|s\rangle$  the metastable singlet state. Wiggly arrows indicate the radiative transition, and black arrows indicate



strong and weak nonradiative decay via the singlet state. (Inset) The three spin sublevels with  $m_s = 0$  and  $m_s = \pm 1$  at zero and nonzero magnetic field  $B$ .  $D$  is the zero-field splitting and  $2\gamma B$  is the Zeeman splitting, where  $\gamma$  is the electron gyromagnetic ratio. By convention, the lower energy transition is associated with  $m_s = -1$ . (b) Photoluminescence spectrum of an ensemble of NV centers, showing excitation laser (532 nm), the NV0 zero phonon line (575 nm), the NV<sup>-</sup> zero phonon line (638 nm), and NV<sup>-</sup> vibrational side bands (630-800 nm). In typical experiments, nonresonant excitation at 532 nm is used, and luminescence is collected between 630 and 800 nm. (c) Time-resolved luminescence during a 2- $\mu$ s laser pulse. The curves show histograms of photon counts for an NV center excited out of the (blue)  $m_s = 0$  and (red)  $m_s = \pm 1$  spin state. (d, e) Electron paramagnetic resonance (EPR) spectrum of a single NV center at zero and nonzero magnetic field, recorded using the ODMR technique. Source [4].

### 3.6 NV center spin properties

In the absence of a magnetic field, two states of triplet levels with  $m_s = \pm 1$  are degenerate due to the axial symmetry of the NV center and are located above the  $m_s = 0$  state at distances  $D = 2.87$  GHz and  $D = 1.42$  GHz for the ground  $|g\rangle$  and excited  $|e\rangle$  states, respectively. The  $D$  parameter is called zero-field splitting. In the case of magnetic field applied, the degeneracy between the levels  $m_s = \pm 1$  is removed due to the Zeeman splitting and they are shifted in opposite directions, as shown in Figure 6 a (inset), which determines the sensitivity of the NV center to the magnetic field. The transitions between sublevels  $m_s = 0$  and  $m_s = \pm 1$  are determined by the spin-lattice relaxation time  $T_1$ , which is several ms at room temperature [41]. And, notably, the transitions between the ground  $|g\rangle$  and excited  $|e\rangle$  states and are strongly spin protecting [4].

Electrons at levels  $m_s = \pm 1$  of the excited state  $|e\rangle$  have a significant chance of decay through a nonradiative long-lived singlet state  $|s\rangle$ , in contrast to electrons with  $m_s = 0$ , which decay through a fast transition and contribute to fluorescence. As a result, approximately 30% optical contrast is formed between the states with  $m_s = \pm 1$  and  $m_s = 0$ . As can be seen from Figure 6 c, the optical contrast disappears with prolonged laser illumination (the initial emission peak in the presented histogram is due to fast radiative transitions, after which, due to singlet decay, a slow recovery occurs) [4].

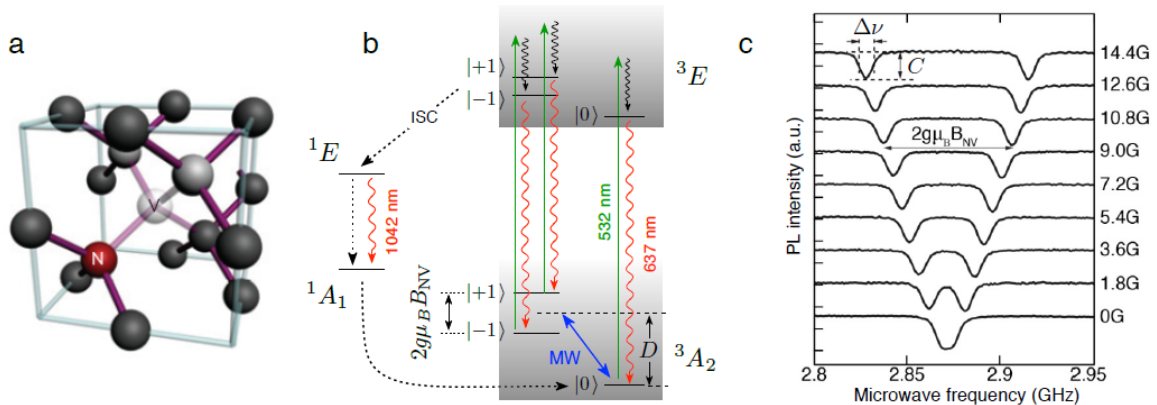


Figure 7. NV structure, energy levels, electron spin resonance

(a) Atomic structure of the NV defect in diamond. (b) Energy level scheme. The notation  $|i\rangle$  denotes the state with spin projection  $m_s = i$  along the NV defect axis. Spin conserving optical transitions from the  $^3A_2$  spin triplet ground state to the  $^3E$  excited state are shown with solid arrows. Such transitions are efficiently excited through non-resonant green illumination on the phonon sidebands. The dashed arrows indicate spin selective intersystem crossing (ISC) involving the singlet states  $^1E$  and  $^1A_1$ . The infrared transition occurring at 1042 nm between the singlet states is also shown. (c) Optically detected electron spin resonance (ESR) spectra recorded for different magnetic field magnitudes applied to a single NV defect in diamond. The ESR transitions are shifted owing to the Zeeman effect, thus providing a quantitative measurement of the magnetic field projection along the NV defect quantization axis. These spectra are recorded by monitoring the NV defect PL (photoluminescence) intensity while sweeping the frequency of the microwave field. Spectra for different magnetic fields are shifted vertically for clarity Source [42].

Due to the presence of such spin-dependent luminescence, NV center is one of the few defects or molecules that can be used to observe electron paramagnetic resonance (EPR) on a single spin [43], [44]. If we slowly sweep the frequency of the MW radiation until it enters resonance with the EPR transition, when excitation occurs from  $m_s=0$  to  $m_s=\pm 1$  states and the fluorescence intensity decreases, then the phenomenon of optically detectable magnetic resonance (ODMR) can be observed (Figure 6 d) [4]. ODMR occurs both in more technically simple experiments using continuous laser and microwave radiation, and in advanced pump-probe experiments that apply sophisticated pulsed magnetic resonance techniques.

The phenomenon of ODMR, when fluorescence is modulated depending on the magnetic interactions of a single electron spin, has formed the basis of many applications using NV centers for highly sensitive measurements of the magnetic field and other physical quantities with nanoscale spatial resolution. As can be seen in Figure 6 d, e, Figure 7 c, the magnetic field removes the degeneracy between levels  $m_s=\pm 1$  and leads to the appearance of two resonances in the ODMR spectrum, which are divided by the frequency  $2\gamma B_z$ , where  $B_z$  is the magnetic field parallel to the NV axis, and  $\gamma \approx 2\pi \times 28$  GHz/T is the electronic gyromagnetic ratio. Therefore, the absolute value of the magnetic field can be obtained by measuring the resonant frequencies of the ODMR [4].

### 3.7 Hyperfine splitting

The influence of the nitrogen and  $^{13}\text{C}$  carbon atoms located near the defect, the nuclei of which have small magnetic fields interacting with the spectral lines from the NV center, leads to the appearance of additional resonance conditions and the so-called fine structure – further splitting of the fluorescence spectrum into additional spectral lines (Figure 8).

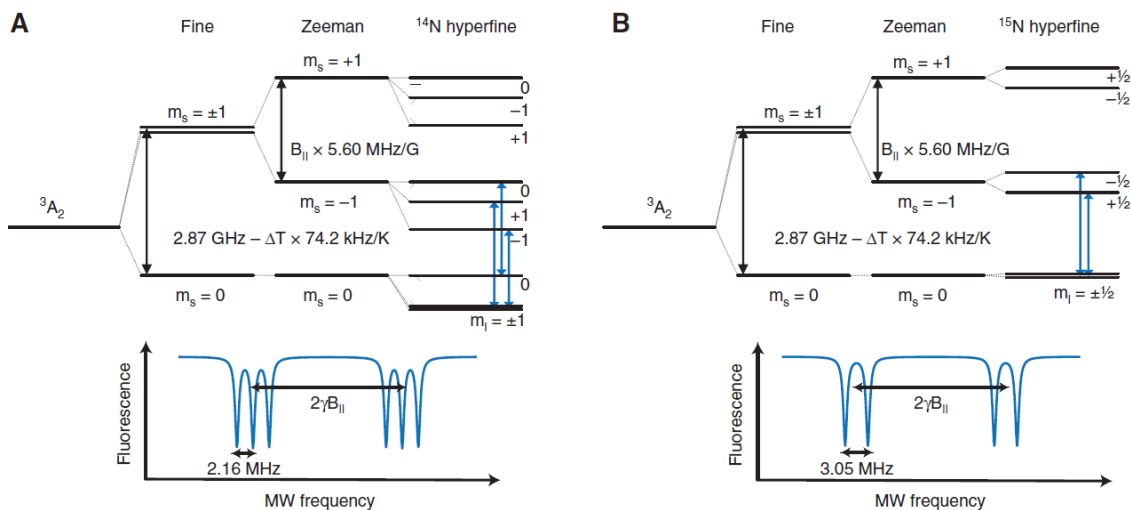


Figure 8. NV ground-state configurations and ODMR Spectra.

(A)  $^{14}\text{N}$  hyperfine states and (B)  $^{15}\text{N}$  hyperfine states. Schematic ODMR spectra are shown with Zeeman splitting and hyperfine splitting for  $^{14}\text{N}$  and  $^{15}\text{N}$ . The energy levels for  $^{14}\text{N}$  are further shifted by quadrupolar interactions Source: [32].

### 3.8 NV center spin Hamiltonian

To describe the interaction of the NV center with the surrounding physical fields, we need to consider its electronic ground-state Hamiltonian [38]:



$$\mathcal{H} = \mathcal{H}_0 + \mathcal{H}_{\text{nuclear}} + \mathcal{H}_{\text{elec|str}}. \quad (\text{eq 3.1})$$

Here, the interaction with an external magnetic field  $B$  is represented by the term  $\mathcal{H}_0$ . The next term  $\mathcal{H}_{\text{nuclear}}$  describes the interactions of the NV center with the spin of the nucleus of the nitrogen atom. The third term  $\mathcal{H}_{\text{elec|str}}$  is responsible for the interaction of the NV center electronic spin with the deformation of the crystal and the electric field.

If we assume that the z-axis is directed along the NV center axis,  $\mathcal{H}_0$  can be written as follows [38]:

$$\mathcal{H}_0/h = DS_z^2 + \frac{g_e\mu_B}{h} (\vec{B} \cdot \vec{S}) \quad (\text{Eq. 3.2})$$

Here  $h$  – is Planck's constant,  $D \approx 2.87$  GHz is zero-field-splitting parameter, resulting of the electronic spin-spin interaction inside the NV center,  $\mu_B$  is the Bohr magneton,  $g_e \approx 2.003$  is the electronic g-factor,  $S = (S_x; S_y; S_z)$  is the electronic spin-1 dimensionless operator.

In many cases, for the purpose of simulating the behavior of the spin of an NV center in the presence of a magnetic field, it is sufficient to take into account the simplest Hamiltonian  $\mathcal{H}_0$ , neglecting the other components.

Additional coupling terms create the spin of the nucleus  $I$  of the nitrogen atom of the NV center. For the  $^{14}\text{N}$  isotope  $I = 1$ , and for the  $^{15}\text{N}$  isotope  $I = 1/2$  [38]

$$\begin{aligned} \mathcal{H}_{\text{nuclear}}/h = & A_{\parallel} S_z I_z + A_{\perp} (S_x I_x + S_y I_y) \\ & + P[I_z^2 - I(I + 1)/3] \\ & - \frac{g_I \mu_N}{h} (\vec{B} \cdot \vec{I}), \end{aligned} \quad (\text{Eq. 3.3})$$

Here  $P$  is the nuclear electric quadrupole parameter, and in the case of the  $^{15}\text{N}$  isotope, for which  $I = 1/2$ , the last term vanishes, since there is no quadrupole moment for spins  $< 1$ .  $A_{\parallel}$  and  $A_{\perp}$  denote the magnetic hyperfine axial and transverse coupling coefficients, respectively.  $I = (I_x; I_y; I_z)$  is the dimensionless nuclear spin operator,  $g_I$  is the nuclear g factor of the nitrogen isotope used, and  $\mu_N$  is the nuclear magneton.

The Hamiltonian describing the interaction of the electron spin of the NV center with the electric field  $E$  and the stress of the crystal, causing its deformation, is as follows [38]

$$\begin{aligned} \mathcal{H}_{\text{elec|str}}/h = & (d_{\parallel} E_z + \mathcal{M}_z) S_z^2 \\ & + (d_{\perp} E_x + \mathcal{M}_x) (S_y^2 - S_x^2) \\ & + (d_{\perp} E_y + \mathcal{M}_y) (S_x S_y + S_y S_x) \\ & + (d'_{\perp} E_x + \mathcal{N}_x) (S_x S_z + S_z S_x) \\ & + (d'_{\perp} E_y + \mathcal{N}_y) (S_y S_z + S_z S_y). \end{aligned} \quad (\text{Eq. 3.4})$$

Here  $\mathcal{M}_z$ ,  $\mathcal{M}_x$ ,  $\mathcal{M}_y$ ,  $\mathcal{N}_x$  and  $\mathcal{N}_y$  are the spin-strain coupling parameters;  $d_{\perp}$ ,  $d'_{\perp}$  and  $d_{\parallel}$  are the transverse and axial dipole moments, respectively, the data on the experimental values of which are given in the Table 3.



**Table 3.** Compiled constants for the electronic ground state of the NV<sup>-</sup> center in diamond. Source [38]

Constant	Description	Value
$g_{\parallel}$	Axial $g$ factor	$2.0028 \pm 0.0003$
		$2.0029 \pm 0.0002$
$g_{\perp}$	Transverse $g$ factor	$2.0028 \pm 0.0003$
		$2.0031 \pm 0.0002$
$A_{\parallel}$	<sup>14</sup> N axial magnetic hyperfine constant	$\pm 2.32 \pm 0.01$ MHz
		$2.30 \pm 0.02$ MHz
		$-2.14 \pm 0.07$ MHz
	<sup>15</sup> N axial magnetic hyperfine constant	$-2.166 \pm 0.01$ MHz
		$-2.162 \pm 0.002$ MHz
		$-3.1$ MHz
$A_{\perp}$	<sup>14</sup> N transverse magnetic hyperfine constant	$3.01 \pm 0.05$ MHz
		$3.03 \pm 0.03$ MHz
	<sup>15</sup> N transverse magnetic hyperfine constant	$+2.10 \pm 0.10$ MHz
		$-2.70 \pm 0.07$ MHz
		$-3.1$ MHz
		$3.01 \pm 0.05$ MHz
$P$	<sup>14</sup> N nuclear electric quadrupole parameter	$3.65 \pm 0.03$ MHz
		$-5.04 \pm 0.05$
		$-5.01 \pm 0.06$
		$-4.945 \pm 0.01$
		$-4.945 \pm 0.005$
$d_{\parallel}$	Axial dipole moment	$3.5 \pm 0.02 \times 10^{-3}$ Hz/(V/m)
$d_{\perp}$	Transverse dipole moment	$0.165 \pm 0.007$ Hz/(V/m)
		$0.175 \pm 0.030$ Hz/(V/m)
		$0.17 \pm 0.025$ Hz/(V/m)

The last two terms, which are proportional to  $d_{\perp}E_i + N_i$  for  $i = x, y$ , can usually be neglected for the purposes of magnetometry. This is because the energy level shifts, they are responsible for are suppressed by the zero-field-splitting parameter  $D$ , since they are off diagonal in the  $S_z$  basis.

During measurements, the bias field  $B_0$  is often used, which is chosen in such a way as to operate in the linear Zeeman regime, when the energy levels are maximally sensitive to changes in the magnetic field and when terms proportional to  $d_{\perp}E_i + M_i$  can be neglected in  $H_{\text{elec|str}}$  for  $i = x, y$  [38]

$$d_{\perp}E_i + \mathcal{M}_i \ll \frac{g_e\mu_B}{h} B_0 \ll D \quad (\text{Eq. 3.5})$$

In this case, only the first term remains in the term  $H_{\text{elec|str}}$ , which can be combined with the temperature-dependent parameter  $D$ , because it acts on the spin in a similar way. The values of all  $H_{\text{elec|str}}$  parameters responsible for the electric field and deformation do not exceed 1 MHz, except for special cases of operation in the presence of the large electric fields or highly deformed diamonds. In all other cases, the spin of the NV center in the ground state for each of the hyperfine states can be described using the Hamiltonian  $H_0$ .

If the magnetic field  $B = (0;0;B_z)$  is oriented along the main axis of the NV center, the Hamiltonian  $H_0$  can be represented in matrix form with eigenstates  $|m_S=0\rangle$ ,  $|m_S=-1\rangle$  and  $|m_S=+1\rangle$  as follows [38]:



$$\mathcal{H}_0^{(z)}/h = \begin{pmatrix} D + \frac{g_e\mu_B}{h} B_z & 0 & 0 \\ 0 & 0 & 0 \\ 0 & 0 & D - \frac{g_e\mu_B}{h} B_z \end{pmatrix}. \quad (\text{Eq. 3.6})$$

Where the field-dependent transition frequencies are [38]:

$$\nu_{\pm} = D \pm \frac{g_e\mu_B}{h} B_z. \quad (\text{Eq. 3.7})$$

Figure 9 shows the energy diagram of the ground state NV center spin of the in the presence of an axial magnetic field [38].

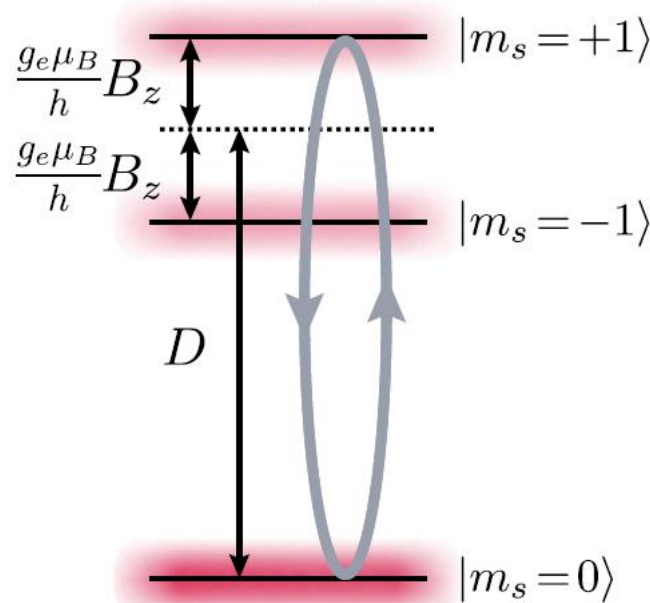


Figure 9. Energy level diagram for the NV<sup>-</sup> ground-state spin in the presence of an axial magnetic field. Energy level diagram for the NV<sup>-</sup> ground-state spin in the presence of an axial magnetic field  $B_z$  and ignoring nuclear spin, as described by equation (3.7). Population in the  $|m_s=0\rangle$  state results in higher fluorescence under optical illumination than population in the  $|m_s \pm 1\rangle$  states. In this diagram, resonant MWs (gray oval) address the  $|m_s=0\rangle \rightarrow |m_s=+1\rangle$  transition. These two levels compose the pseudo-spin-1/2 subspace. Source [38].

During magnetometry experiments, it is usually sufficient to choose one of the two transitions  $|m_s=0\rangle \leftrightarrow |m_s=-1\rangle$  or  $|m_s=0\rangle \leftrightarrow |m_s=+1\rangle$ . This allows to simplify the mathematical description of the picture by presenting the system not as a three-level, but as a two-level one. The frequency of the second transition can be calculated by knowing the frequency of the first. Such a simplification is possible for operations that are short compared to the longitudinal relaxation time  $T_1$  [38].

The fact that both magnetic and electric fields act on the spin with a vector dependence through magnetic and electric terms in the Hamiltonian makes it possible to use NV centers not only to measure the magnitude of these fields, but also their direction. And this is important for some applications, in particular for navigation. NV centers are very sensitive to magnetic fields and only moderately sensitive to electric fields, due to the much stronger magnetic interaction caused by the Zeeman effect than indirectly caused by spin-orbit coupling and the Stark effect electrical interaction. Other physical quantities



can also contribute to the splitting of energy levels through the parameter  $D$ , which characterizes the splitting in zero field, caused by the confinement of the electronic wave function. So, the value of  $D$  can be influenced by such quantities as temperature, pressure, deformation. The parameter  $D$  is sensitive to the vibrations of the surrounding atoms, as well as to the expansion and compression of the crystal [38].



#### 4. MAGNETOMETRY INTRODUCTION & OPERATION REGIMES DEPENDING ON THE MAGNETIC FIELD AMPLITUDE

Since the physical quantity to which NV centers primarily respond is a magnetic field, the main application of NV center sensors is found in magnetometry. The mode of operation of the NV centers devices, even when they are used to measure other physical quantities, also significantly depends on the characteristics of the surrounding magnetic fields and, as a rule, requires the application of a certain bias magnetic field. This chapter will briefly describe the weak magnetic field regime and strong magnetic field regime, which define the main operating modes and affect the sensitivity of the sensors to the magnetic fields to be measured, electric field, or any other quantities.

Magnetometry is a measurement of the absolute value of the magnetic field, its direction, or the measurement of the magnitude of the projection of the magnetic field on a certain axis. All magnetometers must have one or more parameters that depend on the external magnetic field, regardless of their complexity. The simplest magnetically sensitive device is a compass, the arrow of which reacts to the surrounding magnetic field, deviating depending on the magnitude of its flat projection. In a giant magnetoresistance sensor, the applied alternating magnetic field determines the resistance, just as the voltage that appears on the pickup coil varies with it. In atomic magnetometers using gaseous alkaline elements the position of the energy levels of the ground state of the electron, determined by the Zeeman splitting is sensitive to the magnetic field. Similarly, color centers in diamond, such as NV centers, have magnetically sensitive electronic levels. In devices based on them, the magnetic field is determined by finding the frequencies of transitions between energy levels, which change depending on the applied magnetic field. There are various methods that allow to determine the transition frequency both directly by applying frequency-tunable microwave electromagnetic radiation and registering changes in dispersion, fluorescence intensity or absorption, and interferometrically, by measuring the frequency-dependent phase of the transition. [38].

If the hyperfine interaction with neighbouring nuclear spins in the diamond lattice is neglected, the spin Hamiltonian of the ground state of the NV center can be expressed as follows [42]:

$$\mathcal{H} = hDS_z^2 + hE(S_x^2 - S_y^2) + g\mu_B \mathbf{B} \cdot \mathbf{S} \quad (\text{Eq. 4.1})$$

Here D and E are the zero-field splitting parameters.

E is an off-axis zero-field splitting parameter, highly dependent on the diamond matrix. It characterizes the splitting caused by local deformations, which reduce the  $C_{3v}$  symmetry of the NV center. In pure CVD diamonds,  $E \approx 100$  kHz, while in nanodiamonds characterized by strong local deformation, it is on the order of several MHz (Figure 10 e). But at the same time the condition  $E \ll D$  is always fulfilled.

Represented in Eq. (4.1) Hamiltonian can be divided into terms [42]

$$\mathcal{H} = \underbrace{hDS_z^2 + g\mu_B B_{NV} S_z}_{\mathcal{H}_{\parallel}} + \underbrace{g\mu_B (B_x S_x + B_y S_y)}_{\mathcal{H}_{\perp}} + hE(S_x^2 - S_y^2), \quad (\text{Eq. 4.2})$$

Here  $B_{NV} = B_z$  is the projection of the magnetic field directed along the axis of the NV center (Figure 10 a). The two frequencies  $\nu_{\pm}$  corresponding to the EPR frequencies can be find by calculating the Hamiltonian energy eigenvalues for any magnetic field  $\mathbf{B}$ . Figure 10 b shows the dependence of the EPR frequencies  $\nu_{\pm}$  on the magnetic field amplitude  $B = \|\mathbf{B}\|$  for different directions of the magnetic field ( $\theta$  is the angle between



the axis of the NV center and the magnetic field,  $D = 2.87$  GHz and  $E = 5$  MHz – are typical values for NV defects) [42].

Depending on the magnitude of the amplitude field, the so-called weak and strong modes of operation can be distinguished.

#### 4.1 Weak magnetic field regime

If the magnetic field amplitudes are small and the condition  $H_{\perp} \ll H_{\parallel}$  is satisfied, the resonant frequencies can be determined as [42]:

$$\nu_{\pm}(B_{\text{NV}}) = D \pm \sqrt{\left(\frac{g\mu_B}{h} B_{\text{NV}}\right)^2 + E^2} \quad (\text{Eq. 4.3})$$

Such an approximate formula is valid if the transverse component of the magnetic field  $B_{\perp} = (B_x^2 + B_y^2)^{1/2}$  is much less than the coefficient  $hD/g\mu_B \approx 100$  mT. Figure 10 with a dotted line shows the characteristic obtained by the simplified equation (4.3), along with the full calculation. It can be seen that equation (4.3) is well satisfied for amplitudes less than 5 mT.

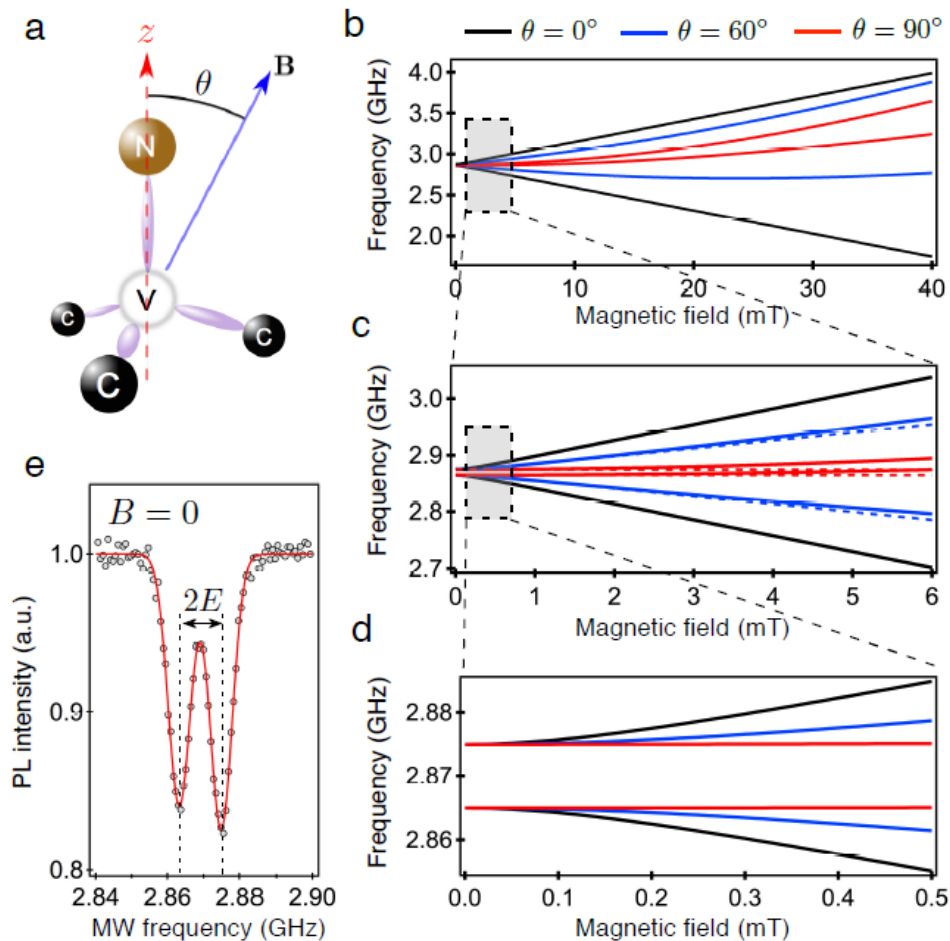


Figure 10. Weak magnetic field regime.

(a) A magnetic field  $\mathbf{B}$  is applied with an angle  $\theta$  with respect to the NV defect axis  $z$ . (b) ESR frequencies  $\nu_{\pm}$  as a function of the magnetic field amplitude  $B = \|\mathbf{B}\|$  for different angles  $\theta$ . The solid lines are obtained by diagonalizing the full Hamiltonian described by Equation (4.1), while using  $D = 2.87$  GHz and  $E = 5$  MHz. (c), (d) Weak magnetic field regime. In (c), the dotted lines correspond to the approximation given by equation (4.3). (e) Typical ESR spectrum recorded at zero-field for a single NV defect hosted in a diamond nanocrystal, leading to  $E \approx 5$  MHz. Source: [42]



In this mode, the resonant frequencies depend quadratically on the magnetic field if  $g\mu_B B_{NV} \sim hE$ . But when the magnetic field is so small that  $g\mu_B B_{NV} \ll hE$  NV center will be insensitive to magnetic field fluctuations and  $\nu_{\pm} \approx D + E$  (Figure 10 d). Thus, the zero magnetic field mode can be used to detect electric rather than magnetic fields, since the local deformation  $E$  protects the central spin from magnetic field fluctuations, and this leads to an increase in the coherence time of the NV center by an order of magnitude. To carry out highly sensitive magnetometric measurements, it is necessary to impose a bias field  $B_{bias}$ , which compensates for the splitting caused by deformation and makes it possible to achieve a linear dependence of the resonant frequencies on the magnetic field ( $B_{bias} \gg hE/g\mu_B$ ). The above features allow you to switch diamond-defect-centre spins between electric- and magnetic-field sensing modes [42] [45].

The weak magnetic field regime is most appealing in NV sensors magnetometry. In this mode the resonant frequencies respond linearly to changes in the magnetic field. The value of the field projection parallel to the NV axis is found simply by measuring the spectral position of either of the two EPR lines [42].

## 4.2 Strong magnetic field regime

In the strong magnetic field regime, the magnetic field amplitudes are stronger and the condition  $H_{\perp} \ll H_{\parallel}$  is not fulfilled. In this case, the dependence of resonant frequencies on the magnetic field ceases to be linear, as at low fields. From the full spectrum of electron paramagnetic resonance (EPR), however, it is possible to obtain information about the magnetic field [46]. But the resonant frequencies exhibit a strong dependence on the direction of the magnetic field with respect to the axis of the NV center (Figure 10 b). The quantization axis no longer coincides with the axis of the NV center, since the magnetic field component perpendicular to the NV axis  $B_{\perp}$  leads to mixing of the electronic spin states. Then the eigenstates of the spin Hamiltonian are given by the superpositions of the spin sublevels  $m_S = 0$  and  $m_S = \pm 1$ , and the projection of the spin onto the NV center axis  $m_S$  is not a good quantum number. There is a strong modification of the spin dynamics of NV center under the action of optical illumination [47]. The optical contrast of the EPR disappears because the spin polarization caused by optical illumination and the spin state dependent photoluminescence are ineffective (Figure 11 a) [42].

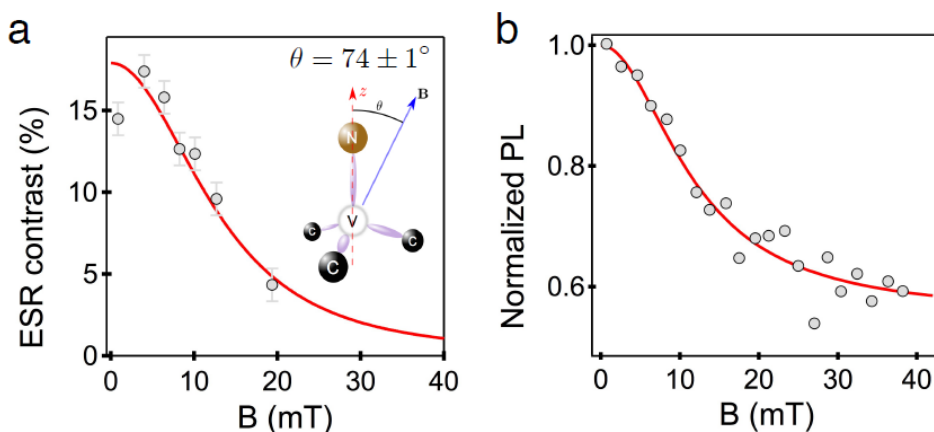


Figure 11. Strong magnetic field regime

(a) ESR contrast and (b) normalised PL intensity as a function of magnetic field amplitude applied with an angle  $\theta = 74^\circ$  with respect to the NV defect axis. The solid line is the result of a rate equation model developed in [47]. Source: [42]

Thus, the strong magnetic regime limits the possibility of magnetic field imaging based on energy level shifts under the action of the Zeeman effect. This complicates some tasks of magnetometry, for which strong magnetic fields are typical. For example,



visualization of ferromagnetic nanostructures when the fields exceed several tens of mT [42]. But in this case, to obtain an all-optical image of the magnetic field, the effect of a general decrease in the fluorescence intensity of the NV center can be used which accompanies a decrease in the optical contrast of the EPR with an increase of the magnetic field projection perpendicular to the NV axis [48] (Figure 11 b).



## 5. SENSING PROTOCOLS

A number of different experimental protocols have been developed to measure EPR frequency shifts induced by external influences. Among the most commonly used basic methods are the direct recording of the EPR spectrum by continuous-wave spectroscopy, various pulsed pump-readout experiments that make it possible to measure the time evolution of the spin states, and also the measurement of the spin relaxation time. This chapter will discuss some of these measurement protocols, adapted to measure both continuous and variable fields, as well as those that include special techniques to improve the sensitivity of the measurements.

### 5.1 Continuous-wave optically detected magnetic resonance (CW-ODMR)

The continuous-wave optically detected magnetic resonance (CW-ODMR) is the simplest and most widely used method in magnetometry (Figure 12a, b). In this method, microwave excitation, optical polarization, and readout occur simultaneously. Optical laser radiation, acting continuously, transfers NV centers to the ground state  $m_S = 0$ , which gives a high fluorescence intensity. At the same time, MW radiation tuned to resonance with one of the  $m_S = 0 \leftrightarrow m_S = \pm 1$  transitions switches the spin population to the  $m_S = \pm 1$  state, which reduces the emitted light. In the case of a change in the local magnetic field, the resonance characteristic depending on the excitation MW frequency shifts and the intensity of the registered fluorescence changes. [38].

Beyond the simplest implementation of CW-ODMR, where all centers of resonant lines are determined by scanning the MW frequency across the entire spectrum, it is possible to tune the MW frequency to the maximum slope of one of the resonant perturbations such that small changes in the magnetic field result in the largest changes in PL, as this is shown in Figure 15 a. Further increase in sensitivity can be achieved by additional modulation of the MW frequency to suppress noise. It is also possible to increase the contrast by simultaneously exciting several hyperfine transitions[38].

The main advantage of CW-ODMR is the simplicity of its technical implementation compared to pulse schemes, since this method does not require the use of complex precision equipment such as fast photodetectors or multi-channel timing switches and generators to provide MW phase control and pulsed laser excitation. When interrogating a large number of sensors with the same optical excitation power, the CW-ODMR protocol, if properly implemented, can show the same sensitivity as pulsed magnetometry methods. Another advantage is its greater resistance to MW inhomogeneities than that of pulsed methods [38].

Despite the fact that the use of ensembles of NV sensors makes it possible to obtain sensitivity for the CW-ODMR method comparable to that for the Ramsey method, its disadvantage is the broadening of the spectral line under the influence of high-power laser and MW radiation. The sensitivity of the CW-ODMR method will be optimal at such radiation powers at which the spectral linewidth is limited only by the dephasing time  $T_2^*$ . And the sensitivity of pulse schemes does not suffer from the continuous action of optical and MW radiation. In addition, the need to scan the frequency of MW radiation in a large range, while reading optical signals for a long time, makes the CW-ODMR method slow compared to pulsed ones [16].

Pulsed methods, in contrast to CW-ODMR, make it possible to optimize the sensitivity parameters, since the short duration of pump and readout laser pulses and short MW drive pulses makes it possible to achieve a compromise between the low photon detection rate associated with low optical power and the wide spectral line caused by high optical and microwave powers [49].

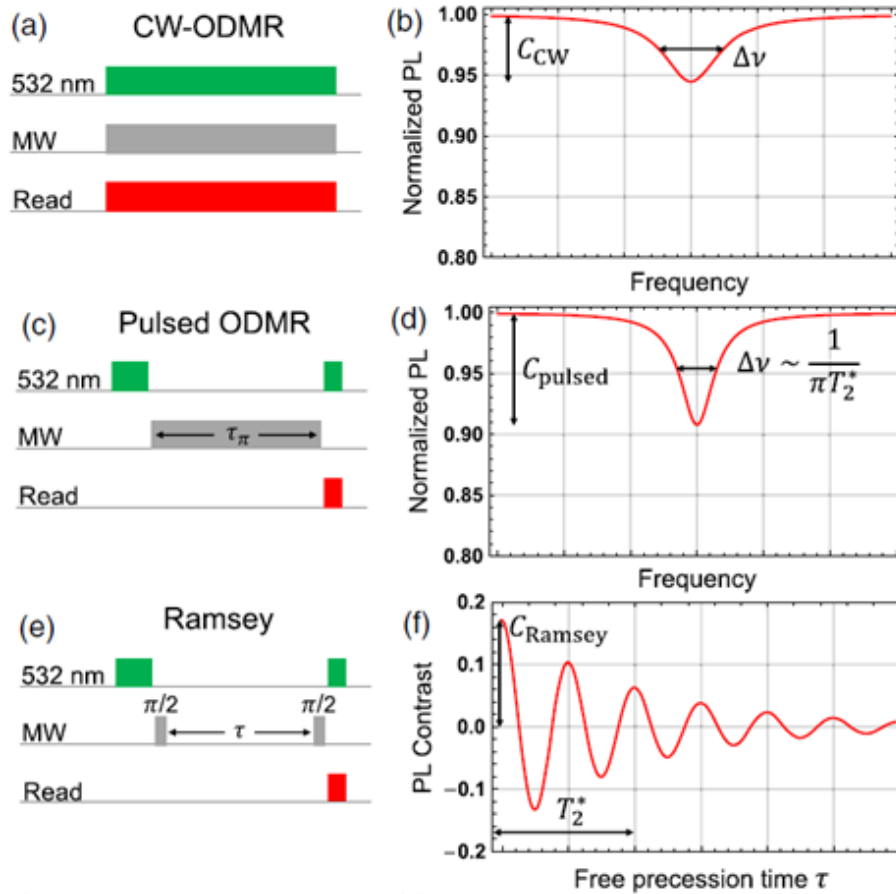


Figure 12. Overview of CW-ODMR, pulsed ODMR and Ramsey magnetometry protocols

(a) Schematic of CW-ODMR sensing protocol. (b) Representation of CW-ODMR spectrum with contrast  $C_{CW}$  and linewidth  $\Delta\nu$ . (c) Schematic of pulsed ODMR sensing protocol with MW  $\pi$ -pulse time  $\tau_\pi \sim T_2^*$ . (d) Representation of pulsed ODMR spectrum with contrast  $C_{pulsed}$  and linewidth  $\Delta\nu \sim 1/(\pi T_2^*)$ . (e) Schematic of Ramsey magnetometry protocol. (f) Representation of free induction decay associated with a Ramsey protocol vs free-precession time  $\tau$ . Fringes exhibit contrast  $C_{Ramsey}$  and decay exponentially with dephasing time  $T_2^*$ . Source: [38].

## 5.2 Pulsed ODMR

As an alternative to the CW-ODMR method, the Pulsed ODMR method was proposed in [49], which, like the Ramsey method, makes it possible to perform measurements limited only by the dephasing time  $T_2^*$ , avoiding optical and microwave broadening of the EPR spectral lines. However, this method is affected by temporal and spatial variations in the Rabi frequency. If the high MW field strengths needed to implement the Ramsey method are not available and the Rabi frequency variations are minimal, the Pulsed ODMR method is very attractive [38].

Figure 12 c shows a schematic of the pulse sequence used in the Pulsed ODMR protocol. First, the laser pulse transfers the NV spin to the  $m_S=0$  state, followed by an MW pulse with a duration  $\tau_\pi$  determined by the relation  $\Omega_R = \pi/\tau_\pi$ , where  $\Omega_R$  is the Rabi frequency. With the aid of a second laser pulse, the resulting spin population is optically read out. A change in the magnetic field causes a detuning of the resonant frequency, which leads to the incompleteness of the  $\pi$ -pulse and a change in the populations of  $m_S=\pm 1$  levels [38].



Since in the Pulsed ODMR protocol, unlike in CW-ODMR, optical and microwave excitation are not applied simultaneously and continuously, the effective power is much less, and there is no problem of EPR line power-broadening for the Pulsed ODMR method. It is possible to use a strong initiating laser pulse and improve the photon collection per measurement reducing the effect of shot noise on the sensitivity without using a constant optical excitation [16].

The contrast that the Pulsed ODMR method can provide is less than the contrast obtained by the Ramsey method (Figure 12 e, f) due to the use of the lower Rabi frequencies in it, since they must correspond to the spectral linewidth determined by  $T_2^*$  and cannot effectively excite the entire NV ensemble and control all the  $^{14}\text{NV}$  or  $^{15}\text{NV}$  ultra-fine transitions with a single tone. (The Ramsey method achieves this applying the higher Rabi frequencies  $\sim 2\pi \times 10$  MHz). If, however, in the Pulsed ODMR multi-tone pulses are used, the contrast may deteriorate due to the MW cross excitation when the resonance linewidth (limited by  $T_2^*$ ) and, hence, the Rabi frequency correspond to hyperfine splitting [38].

### 5.3 Ramsey measurements

As was noted, the fundamental limit of the width of the resonance line is determined by the dephasing time:  $\Delta\nu \approx \frac{1}{T_2}$ . To achieve this limit most effectively, eliminating the problem of power-broadening of the EPR line, Norman Ramsey's separated oscillatory fields method is used. This method, adapted for NV center magnetometry, makes it possible to separate in time the manipulation of the spin, the accumulation of the phase (the actual measurement of the magnetic field), and the readout of the result. It uses a two-level spin subspace, e.g.,  $\{|0\rangle, |1\rangle\}$ . First of all, the laser pulse transfers the spin of the NV center to the state  $|0\rangle$ . Then, an alternating magnetic field  $B_1(t)$  is applied, having a frequency  $\nu$ , resonant to the  $|0\rangle \leftrightarrow |1\rangle$  transition and polarized in the x-y plane. This field provokes oscillations of the population of the spins between the states  $|0\rangle$  and  $|1\rangle$  with the Rabi angular frequency ( $\Omega_R \propto B_1$ ). The resonant field  $B_1(t)$  acts during the time  $\pi/(2\Omega_R)$  – the so-called  $\pi/2$ -pulse. The  $\pi/2$ -pulse transforms the initial state  $|0\rangle$  into a superposition of equiprobable states  $|0\rangle$  and  $|1\rangle$ , that is,  $(|\psi\rangle = \frac{1}{\sqrt{2}}(|0\rangle + |1\rangle))$ . Then, during the time  $\tau$ , the free precession of the system occurs in the presence of an external magnetic field. As a result, a phase accumulates between the two states, which depends on the external magnetic field. The phase of the state  $|1\rangle$  with respect to the state  $|0\rangle$  is  $\varphi = \tau g\mu_B B/\hbar$  and it corresponds to the spin precession in the plane perpendicular to the spin quantization axis. As a result,  $|\psi\rangle = \frac{1}{\sqrt{2}}(|0\rangle + e^{i\varphi}|1\rangle)$ . After that, the second  $\pi/2$ -pulse is applied. It again projects the electron spin of the NV center onto the quantization axis. This makes it possible to convert the field-dependent phase accumulated as a result of free precession into the population difference between levels  $|0\rangle$  and  $|1\rangle$ . As a result, the fluorescence intensity is measured, which depends on the state of the spin [42].

Figure 13 shows the Ramsey sequence on the Bloch sphere. The states  $|0\rangle$  and  $|1\rangle$  are denoted, respectively, by the symbols  $|\uparrow\rangle$  and  $|\downarrow\rangle$  [38].

The readout accuracy of the obtained spin state projection  $S_z$  is fundamentally limited by quantum mechanical uncertainty. Measurements carried out in the basis  $\{|0\rangle, |1\rangle\}$  suggest only two possible outcomes: 0 or 1. As a result of the noted uncertainty, the projection measurement inevitably occurs with a loss of information caused by the so-called **spin projection noise**. Since this noise is related to the fundamental quantum-mechanical nature of the NV center, and it cannot be reduced by any means, it is assumed that the sensor, whose sensitivity is limited only by the projection noise, has a spin readout fidelity  $F = 1$ . Various other factors, such as **photon shot noise**, lead to a decrease in the fidelity  $F$  and sensitivity of the sensor to a magnetic field [38].

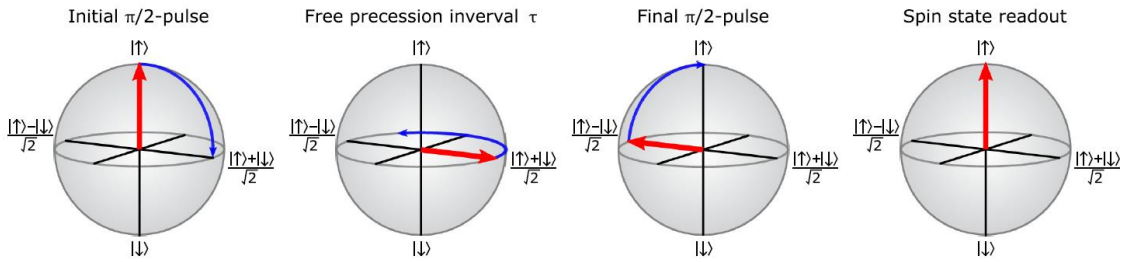


Figure 13. Bloch sphere depiction of Ramsey sequence.

After initialization to the spin state  $|\uparrow\rangle$ , a sinusoidally varying magnetic field rotates the state vector by  $\pi/2$ , thus preparing a superposition of  $|\uparrow\rangle$  and  $|\downarrow\rangle$  spin states. Next the Bloch vector undergoes free precession for duration  $\tau$ , accumulating a phase  $\varphi$  proportional to the static magnetic field being sensed. After time  $\tau$ , a second  $\pi/2$  pulse maps the accumulated phase onto a population difference between the  $|\uparrow\rangle$  and  $|\downarrow\rangle$  states. Here a  $\varphi = \pi$  phase accumulation is shown, which maps back to the state  $|\uparrow\rangle$ . Finally, a projective spin-state measurement detects the population difference, allowing determination of the static magnetic field sensed by the spin. Source: [38].

To obtain information about the magnitude of the magnetic field, the sequence of Ramsey pulses is usually repeated millions of times in order to collect a sufficient number of photons. Each measurement is carried out for different values of  $\tau$ , sweeping the free precession interval. The result is a contrast fluorescence signal oscillating at an EPR-transition frequency as a function of  $\tau$  referred to as **the Ramsey fringes** (Figure 14 a). The Ramsey fringes Fourier transform gives the dominant frequencies locations and allows to determine their deviations from the bias field caused by the measured magnetic field [32].

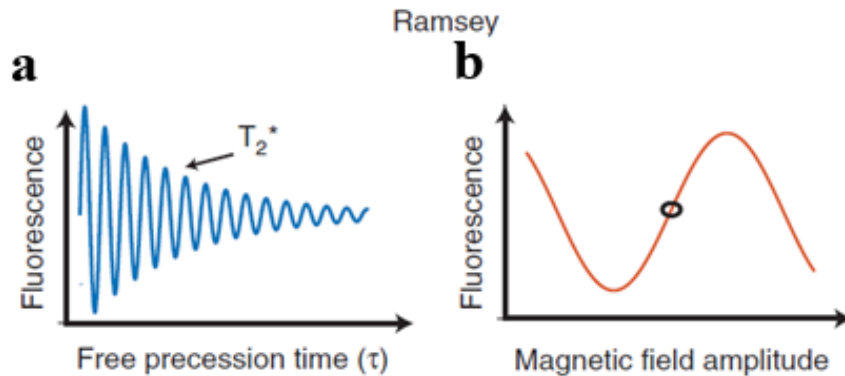


Figure 14. Ramsey free induction decay and Ramsey magnetometry curve

(a) Schematic Ramsey free induction decay (FID) to determine the dephasing time  $T_2^*$  and the optimal sensing time ( $\tau_{\text{sense}}$ ). (b) Schematic Ramsey magnetometry curve. Free precession time is fixed to be the point of maximum slope of the FID curve closest to  $T_2^*$ , indicated by a black circle. Accumulated phase from the sample field results in an oscillatory response of fluorescence with changing amplitude. Source: [32].

However, from the point of view of measurement speed, plotting the full Ramsey fringes characteristic and performing its Fourier transform is as inefficient as frequency sweeping in the ODMR method. To obtain a faster result, the free precession time is fixed at that point of the curve closest to  $T_2^*$ , which has the greatest slope, and therefore corresponds to the maximum sensitivity. Thus, a magnetometry curve is obtained, as shown in Figure 14 and Figure 15 b. The measurement protocol is the more sensitive, the steeper the magnetometry curve [32].



## 5.4 Rabi beat sensing

Rabi beat sensing is a generalization of the Pulsed ODMR method where during the interrogating time the spins are excited by multiple Rabi oscillations [50], [51]. The sensitivity of the Rabi method can approach that of the Ramsey method under optimal conditions, as in the special case of the Pulsed ODMR method. To obtain the best sensitivity at Rabi frequencies  $\Omega_R$  exceeding the width of the resonance line ( $\sim 1/T_2^*$ ), it is necessary to choose the interrogating time at the point of maximum slope of the Rabi magnetometry curve close to the dephasing time  $T_2^*$ , and the detuning close to the Rabi frequency ( $\Delta \sim \Omega_R$ ). But, since for the high values of  $\Omega_R$ , microwave field variations can be limited by the effective value of  $T_2^*$ , due to the strong sensitivity of this method to the temporal and spatial variations in the frequency of MW radiation, practical implementations of the method show the best results when  $\Omega_R \sim 1/T_2^*$  and the protocol is reduced to the Pulsed ODMR method [38].

## 5.5 AC detection. Spin-echo magnetometry

The application of the Ramsey sequence has proven itself well for the study of static magnetic fields. However, the sensitivity of measurements can be significantly increased when measuring alternating fields with frequencies in the range from kilohertz to megahertz using the Hahn spin echo method. In this method, the free precession time is interrupted in the middle of the interval by an additional microwave  $\pi$ -pulse, which makes it possible to reverse the dephasing caused by static fields and thus get rid of low-frequency noise. The decay of the spin echo is determined by the coherence time  $T_2$ , which is much longer than the dephasing time  $T_2^*$  and can reach several hundred microseconds in pure crystals. This highly sensitive method has demonstrated a sensitivity of several nT [4].

If several  $\pi$ -pulses are applied during the interrogating interval, a simple spin echo sequence will be extended to a multi-echo. Multiple spin echoes protocols act as a narrowband lock-in amplifier whose detection frequency is controlled by the interval between pulses. By applying such a sequence having a narrow band filter profile, the coherence time can be brought up to several milliseconds. The method is suitable for working with high-frequency megahertz signals of nuclear spins and can be applied to nano-resolution NMR. [4].

## 5.6 Relaxometry

Magnetic resonance relaxometry makes it possible to study even higher frequency signals (from megahertz to gigahertz). Such a measurement protocol is based on the measurement of the spin relaxation time  $T_1$ , which directly reflects the amount of magnetic noise at the resonant frequency. The method does not require MW driving, which makes it particularly easy to use. An example of a relaxometric experiment is shown in Figure 15 c. In the presence of paramagnetic gadolinium ions  $Gd^{3+}$ , the decay occurs much faster [52]. Gadolinium is characterized by spin ( $S=7/2$ ), it produces gigahertz fluctuations causing strong magnetic noise at the resonant frequency of the NV center (2.9 GHz) [4].

In addition to the relaxation time  $T_1$ , the spin-lock decay time  $T_{1\rho}$  (spin-lattice relaxation in a rotation frame in the presence of an external RF pulse in the transverse plane) can be measured in a similar way, which makes it possible to measure magnetic signals up to 100 MHz with high spectral resolution (less than 10 kHz) and sensitivity (less than 100 nT) [4].

## 5.7 Double-quantum (DQ) coherence magnetometry

Double-quantum (DQ) coherence magnetometry makes full use of the spin-1 nature of the NV ground state, unlike the previously described protocols, when measurements are performed in a hypothetical single-quantum (SQ) subspace with pseudo-spin 1/2. In SQ magnetometry, the difference between the spin states  $|m_S = 0\rangle$  and  $|m_S = \pm 1\rangle$  is  $\Delta m_S = 1$ , and in the DQ method, the difference between  $|m_S = -1\rangle$  and  $|m_S = +1\rangle$  ( $\Delta m_S = 2$ ) is used. The sequence of pulses applied to implement this method is schematically shown in Figure 16. First of all, an equal superposition of states is created, for example,  $|+DQ\rangle = (1/\sqrt{2})(|+1\rangle + |-1\rangle)$ . This is followed by an interval of free precession under the action of the measured magnetic field. After mapping the population accumulated in  $|+DQ\rangle$  back to  $|0\rangle$ , the resulting difference between  $|0\rangle$  and  $|-DQ\rangle$  is optically read. Here  $|+DQ\rangle = (1/\sqrt{2})(|+1\rangle + |-1\rangle)$  is the so-called bright state, and  $|-DQ\rangle = (1/\sqrt{2})(|+1\rangle - |-1\rangle)$  – dark state [53], [38].

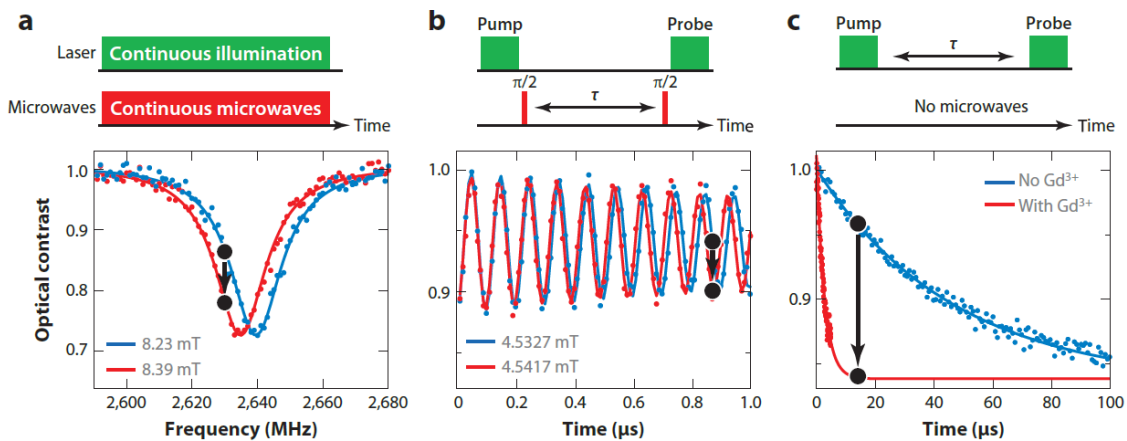
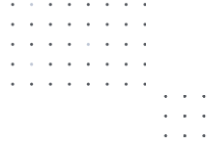


Figure 15. Sensing techniques and protocols

Sensing techniques and protocols, showing (top) pulse-timing diagrams and (bottom) example measurements. (a) Continuous-wave detection of the spectral line shift. The frequency difference between curves is 4.7 MHz, corresponding to a magnetic field difference of 0.16 mT. (b) Pulsed detection of the spin precession (Ramsey fringes) in a pump-probe experiment. The frequency difference between curves is 0.25 MHz, corresponding to a magnetic field difference of 9.0  $\mu T$ . Oscillations are shown relative to a 2,753-MHz carrier frequency. (c) Relaxometry measurement, showing  $T_1$  relaxation of a nitrogen-vacancy center in a 25-nm nanodiamond in the presence and absence of paramagnetic  $GdCl_3$  salt. The black dots mark changes in intensity caused by tuning the microwave frequency to the point of highest slope. The black arrow denotes the increase and decrease in fluorescence intensity as the resonance shifts up and down in frequency, respectively. Schematic of timing and duration of laser pulses, MW pulses, and readout sequences relative to the field being sensed for common NV diamond protocols. Swept parameters are indicated by arrows. Straight lines for the bias and sample fields indicate static magnetic fields, including the swept static bias field for Rabi and  $T_1$  relaxometry. Sinusoidal curves represent time-dependent sample fields, which are very high frequency for Rabi and  $T_1$  relaxometry. Source: [4]

The sensitivity of the DQ method is higher than that of the SQ methods, since the spin precession in the superposition of  $|+1\rangle$  and  $|-1\rangle$  is twice as fast as in  $|0\rangle$  and  $|\pm 1\rangle$  superposition. Another advantage of this method is the effective suppression of noise caused by axial electric fields, transverse magnetic fields, axial strain gradients and temperature fluctuations, which enter the of the Hamiltonian NV center via the parameter  $D$  ( $\partial D/\partial T \approx -74$  kHz/K) [54], [55]. These noise sources perturb transitions  $|0\rangle \leftrightarrow |\pm 1\rangle$  [38].

However, for diamonds with a high concentration of nitrogen impurities or with a natural concentration of the  $^{13}C$  carbon isotope, operation in the DQ mode leads to a reduction in the dephasing time and an increase in the width of the resonance line. This is due to a doubling of the sensitivity to the magnetic fields, as a result of which the dephasing of the spin ensemble in such sensors, with an increased content of the paramagnetic defects, occurs twice as fast as it would be in the SQ basis (i.e.  $T_{2,DQ}^* \approx T_{2,SQ}^* / 2$ ) [56]. Such an effect was observed both in single NV centers and in their ensembles [55], [38].



Therefore, the use of the DQ method is advisable when non-magnetic noise sources predominate (electric fields, inhomogeneities and deformations, temperature fluctuations). In this case, the dephasing time DQ  $T_{2,DQ}^*$ , insensitive to these noises, may exceed the corresponding time for SQ  $T_{2,SQ}^*$ . This makes it possible to further improve the sensitivity of measurements using the DQ method [38].

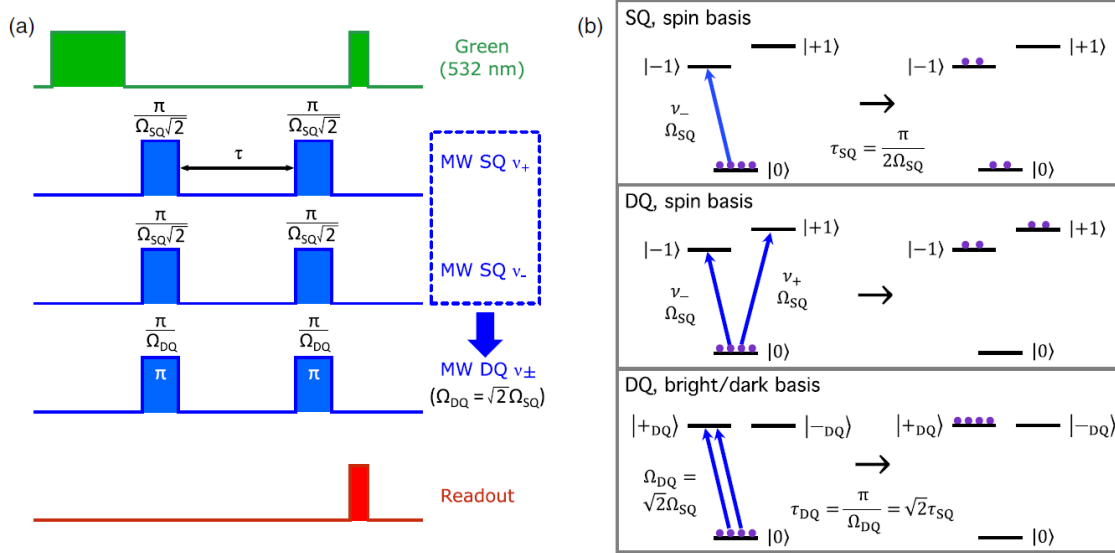


Figure 16. Double-quantum (DQ) coherence magnetometry

(a) Pulse sequence for Ramsey-type double-quantum (DQ) coherence magnetometry. The single-quantum (SQ)  $|0\rangle \leftrightarrow |+1\rangle$  and  $|0\rangle \leftrightarrow |-1\rangle$  transitions are driven by MWs at or near respective resonance frequencies  $\nu_+$  and  $\nu_-$ . For simultaneously applied resonant MWs with Rabi frequencies  $\Omega_+ = \Omega_- = \Omega_{SQ}$ , double-quantum (DQ) transitions occur between  $|0\rangle$  and an equal superposition of  $|+1\rangle$  and  $|-1\rangle$  with corresponding DQ Rabi frequency  $\Omega_{DQ} = \sqrt{2} \Omega_{SQ}$ . A DQ Ramsey sequence requires MW pulses of duration  $\tau_{DQ} = \pi/\Omega_{DQ} = \pi/(\Omega_{SQ}\sqrt{2})$  to prepare the state used for sensing. (b) Comparison between a conventional SQ  $\pi/2$  pulse on a single transition (top panel) and a DQ  $\pi$  pulse used to prepare the superposition state  $|+_{DQ}\rangle = (1/\sqrt{2})(|+1\rangle + |-1\rangle)$  for the sequence in (a) (lower two panels). The middle panel shows the DQ state preparation pulse in the bare spin basis, while the bottom panel shows the same pulse in the basis of  $|0\rangle$  and the bright and dark states  $|+_{DQ}\rangle$  and  $|-_{DQ}\rangle$ , i.e., the orthogonal superposition states, respectively, coupled to and blind to the MW drive. During a DQ Ramsey free-precession interval, spin population oscillates between  $|+_{DQ}\rangle$  and  $|-_{DQ}\rangle$  (as these states are not energy eigenstates), at a rate proportional to the magnetic field. Source: [38].

## 5.8 Spin-to-charge conversion (SCC) readout

Another technique that is used to improve the sensitivity of measurements is the use of NV center spin states readout methods alternative to conventional fluorescence-based readouts. One such technique is spin-to-charge conversion (SCC) readout. In this method, the spin state is transferred to neutral ( $NV^0$ ) and negatively charged ( $NV^-$ ) NV centers. Due to the differences in the wavelength dependences of the fluorescence intensity for the  $NV^0$  and  $NV^-$  centers, these charge states can be accurately read. The SCC method allows to collect more photons per readout than conventional methods (and therefore reduce the contribution of shot noise to the measurement) and provides highly accurate charge determination due to the ability to read the charge for a long time. This method is characterized by a slightly increased spin contrast. The readout fidelity it provides is close to the limiting accuracy determined by spin projection noise. The application of the SCC method has been shown both for single NV centers and for their small ensembles [38].

To carry out measurements using the spin-to-charge conversion method, it is necessary to be able to accurately control the state of charge of the NV center. The charge dynamics upon optical excitation points to power and wavelength selective



photoionization processes, which can be used to achieve controlled switching between the  $NV^-$  and  $NV^0$  states. Thus, in the near infrared range  $\sim 900\text{--}1000\text{ nm}$ , due to the absorption of two photons by an electron in the metastable singlet state,  $NV^-$  can be selectively ionized to  $NV^0$ . Red light with a wavelength of  $\sim 637\text{ nm}$  or a strong yellow light of  $\sim 589\text{ nm}$  can cause similar ionization by absorption of two photons by an electron in the triplet ground state, while green light of  $\sim 532\text{ nm}$  predominantly transfers (with a 70-75% probability) the single  $NV$  centers to the state  $NV^-$  [38].

Figure 17 shows the photon count histogram obtained for readout the charge of a single  $NV$  center. The histogram shows, at low excitation powers, a clear separation of photon distributions from  $NV^0$  and  $NV^-$ . So, if we introduce a photon detection threshold and simultaneously apply spectral filtering (using the presence of fluorescence in  $NV^-$  and its absence in  $NV^0$  under yellow excitation),  $NV^-$  can be distinguished from  $NV^0$  with an accuracy of more than 99%. Weak yellow lasers at  $\sim 594\text{ nm}$  provide  $NV^-$  state-of-charge readout. Such lasers at intensities below the  $NV^-$  saturation intensity ( $I_{\text{sat}} \sim 1\text{--}3\text{ mW}/\mu\text{m}^2$ ) practically do not excite the  $NV^0$  electronic spin transition characterized by the zero-phonon ZPL line at  $575\text{ nm}$ , but effectively excite, without causing ionization, the corresponding transition of the negatively charged  $NV^-$  center, for which the ZPL is  $637\text{ nm}$  [38].

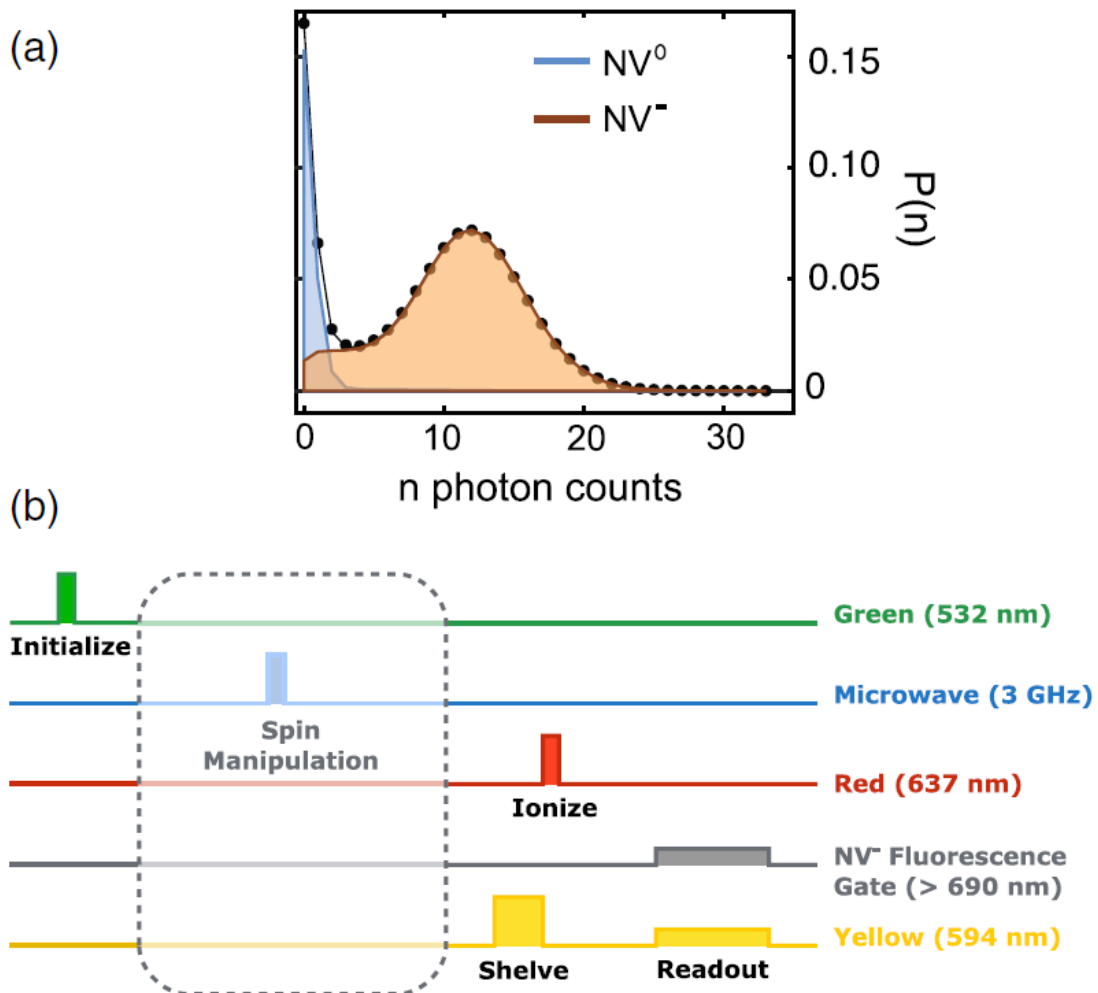


Figure 17. Spin-to-charge conversion (SCC) readout

(a) Probability histogram depicting photon emission from  $NV^0$  and  $NV^-$  under weak yellow excitation. The striking difference in the photon emission rate between  $NV^0$  and  $NV^-$  allows the  $NV$  charge state to be determined with fidelity  $\geq 99\%$ . (b) Schematic of the SCC readout protocol. Source: [38]



Figure 17b shows a schematic of the SCC readout protocol applied in [57]. After transferring the NV center to one of the spin positions of the ground state of the NV triplet ( $m_s = 0$  or  $m_s = \pm 1$ ) using a green laser and MW pulse, the spin population is excited to the upper triplet state by applying a moderate power ( $145 \mu\text{W}$ ,  $\sim 0.9 \text{ mW}/\mu\text{m}^2$ ) yellow “shelving” pulse  $594 \text{ nm}$ . Decaying, electrons with  $m_s=0$  will predominantly fall into the ground state, while electrons with  $m_s = \pm 1$  will find themselves in the singlet metastable level. After that, a resonant pulse of  $637 \text{ nm}$  with a duration of  $\sim 10 \text{ ns}$  and a high intensity ( $22.5 \text{ mW}$ ,  $\sim 140 \text{ mW}/\mu\text{m}^2$ ) ionizes the ground state population (transforms  $\text{NV}^-$  into  $\text{NV}^0$ ) without affecting the set  $m_s = \pm 1$  at the metastable level. The resulting NV charge is read by a weak yellow laser  $575 \text{ nm}$  with low intensity ( $\sim 1\text{--}10 \mu\text{W}$ ,  $\sim 6\text{--}60 \mu\text{W}/\mu\text{m}^2$ ), which is not capable of ionizing  $\text{NV}^-$  during readout, but at the same time is capable of exciting only  $\text{NV}^-$ , since the  $\text{NV}^0$  excitation energy is greater (its ZPL is  $575 \text{ nm}$ ) [38].

Despite the very high accuracy of the charge readout process itself (0.975), the resulting readout fidelity of the SCC method obtained in the experiment described in [57] is only 0.36, due to the imperfection of the spin-to-charge conversion. The conversion accuracy can only be enhanced by significantly increasing the spin reading time  $t_R$ . Thus, the best accuracy ( $F = 0.36$ ) was obtained at  $t_R = 700 \mu\text{s}$ , while conventional fluorescence-based readout is characterized by three orders of magnitude shorter reading time  $t_R \sim 300 \text{ ns}$ . Therefore, the use of the SCC method is recommended in protocols with the long measurement intervals, such as AC sensing or  $T_1$  relaxometry. An improvement in the resulting magnetic field sensitivity using SCC was only achieved for interrogating times greater than  $10 \text{ ns}$ . To make this method more efficient, it is necessary to increase the dephasing time by improving the properties of the spin ensemble [38].

Extending this method to large ensembles would be a logical next step in the development of magnetometry, because the accuracy of a single NV center readout shown by it significantly exceeds the conventional readout fidelity achieved for the large ensembles of NV centers ( $F \lesssim 0.015$ ). Its possible advantage over other methods when working with NV ensembles may be decreasing of the background fluorescence, which reduces sensitivity and arises due to the presence of incorrectly oriented NV centers in large ensembles. Such unused  $\text{NV}^-$  centers can preferably be converted to  $\text{NV}^0$  during the ionization step. Potentially, this can lead to a twofold increase in sensitivity compared to conventional readouts. Problematic for advancing of this method are the already noted long measuring times, as well as the required high optical intensity ( $\gtrsim 150 \text{ mW}/\mu\text{m}^2$ ), which will complicate its application for the large bulk samples ( $\gtrsim 100 \times 100 \mu\text{m}^2$ ). In addition, the possibility of mitigating the additional complex charge dynamics characteristic of diamonds with a high NV content requires further studying. [38].

## 5.9 Ancilla-assisted repetitive readout

Another alternative method for the resulting readout is the ancilla-assisted repetitive readout, which uses an auxiliary nuclear spin during the readout process, onto which the initial information about the electronic spin state of the NV center is mapped before transferring it back to the electron spin and finally reading it using fluorescence. Applying conventional readout methods, even with the best existing photon collection efficiency, the average number of photons that can be detected from each NV center is less, and sometimes much less than one. This is due to the rapid (about  $500 \text{ ns}$ ) repolarization of the electron spin of the NV center, which significantly limits the number of photons emitted by it before useful information about its spin state is lost. Thus, the dominant factor affecting the readout fidelity is photon shot noise. Since, in the proposed method, the state recorded on the auxiliary nuclear spin can be repeatedly mapped back to the electron spin, the accuracy of the cumulative readout is significantly improved (Figure 18 a, b). For the first time, this method was implemented using, as an auxiliary spin, the nucleus of the neighboring  $^{13}\text{C}$  atom. However, for the purpose of scaling the method

(working with an ensemble of NV centers), it is preferable to use the nuclei of  $^{14}\text{N}$  or  $^{15}\text{N}$  atoms of the NV center itself, because the connection with the auxiliary spin depends on the distance to it, and for ensembles the distances to the different neighboring  $^{13}\text{C}$  atoms can vary greatly[58], [38].

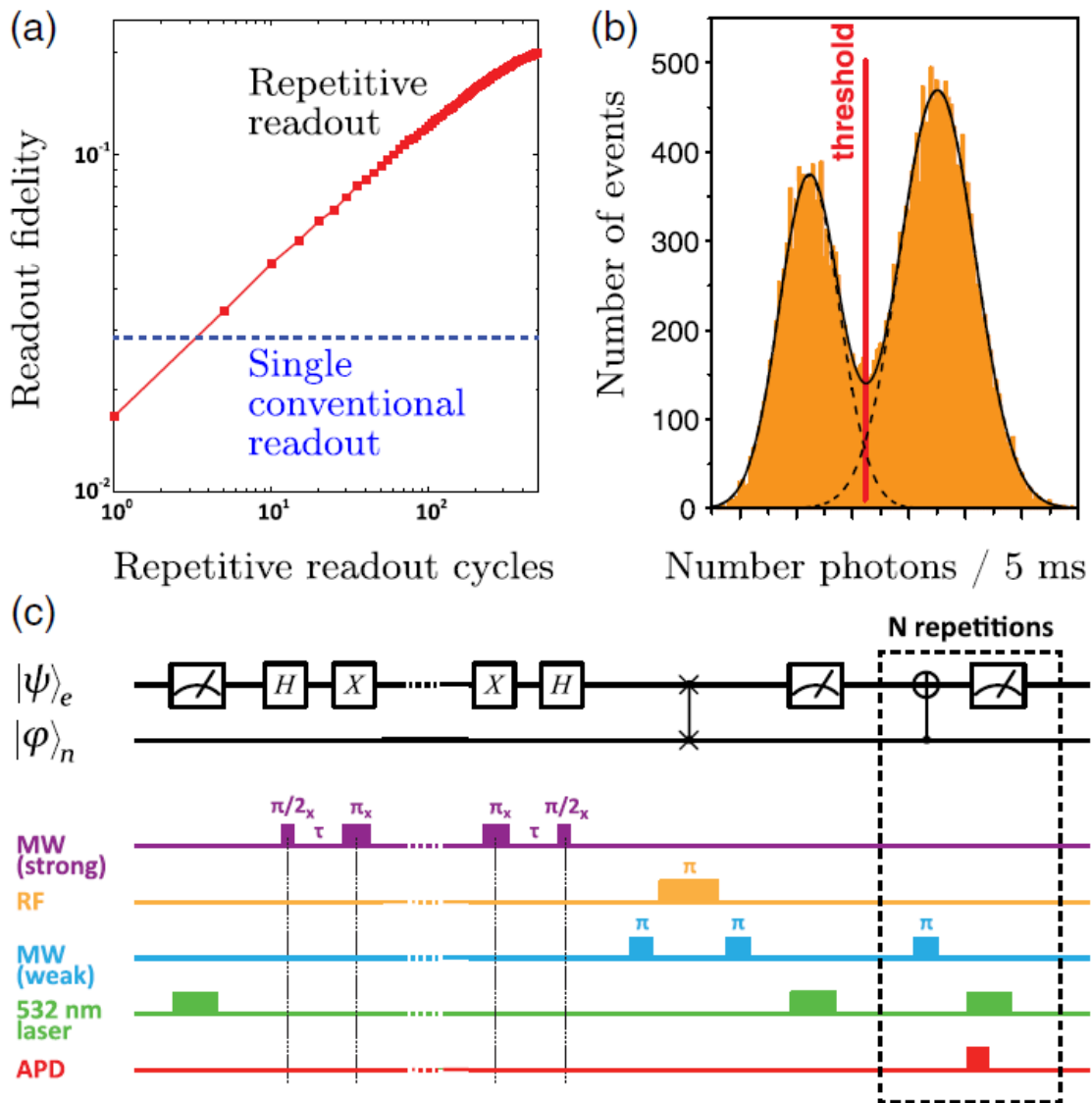
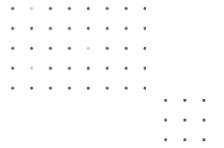


Figure 18. Ancilla-assisted repetitive readout

Overview of ancilla-assisted repetitive readout. (a) Readout fidelity  $F$  is improved with the number of repetitive readout cycles. Fidelity for repetitive readout (red) is plotted relative to a single conventional readout (dashed blue). (b) The clear difference in total number of collected photons associated with the initial ms states allows determination of ms with fidelity approaching 1 in some implementations. Here  $F \approx 0.92$  [59]. (c) Quantum circuit diagram and magnetometry pulse sequence with detection via ancilla-assisted repetitive readout. Application of an RF  $\pi$  pulse between two weak MW  $\pi$  pulses maps the NV<sup>-</sup> electronic spin superposition onto the ancilla nuclear spin. Subsequently, the superposition state may be repeatedly mapped back onto the electronic spin via a weak MW  $\pi$  pulse and optically read out without destroying the ancilla spin's quantum state. Source: [38].

The quantum circuit diagram for the ancilla-assisted repetitive readout protocol is shown in Figure 18 c, where the state of the electronic NV spin is denoted by index  $e$ , and the spin state of the nitrogen atom nucleus is denoted by index  $n$ . After the final MW pulse, the state of the electron NV spin is mapped onto the state of the nuclear spin using the SWAP gate (CNOT $_{e|n}$  - CNOT $_{n|e}$  - CNOT $_{e|n}$ ). Here CNOT stands for a controlled NOT gate. The SWAP gate is implemented by a sequence of MW - RF - MW  $\pi$ -pulses [58] Microwave  $\pi$ -pulses flip the electron spin, while radio frequency pulses flip the nuclear





spin. Such a sequence swaps the states of the electronic and nuclear spins. In this case, the auxiliary nuclear spin retains information about the electronic spin state. After that, the optical pulse again initiates the electron spin into the  $m_S = 0$  state and a series of repeated readouts is carried out, during each of which the state of the nuclear spin is again copied into the electronic one by applying a microwave pulse (a CNOT $|n\rangle$  gate). The electronic spin is optically read, and the nuclear one continues to store the recorded state, allowing this process to be repeated up to hundred times (the number of such possible repetitions is fundamentally limited by the lifetime of the nuclear spin  $T_{1;n}$ ). Each read cycle lasts about  $\sim 1 \mu\text{s}$ , and the initial RF pulse used in the SWAP gate is  $\sim 50 - 60 \mu\text{s}$ . Such a large number of readings brings the total readout fidelity to values close to unity. Thus, in the experiment [59]  $F = 0.92$  (Figure 18 b) [38].

To implement the described method with ensembles of NV centers, a number of technical difficulties must be solved, such as the creation of a large bias magnetic field strictly aligned along a single NV symmetry axis, excluding the possibility of measuring for more than one orientation. The bias field makes it possible to minimize the coupling between the nuclear and electron spins of NV (fields of 2500 and 6500 G, respectively, were used in [51] and [52]). Since even small angular deviations affect the nuclear spin and reduce the  $T_{1;n}$ , the implementation of ensemble measurements requires a very uniform magnetic field over the entire probing volume on a scale of  $\sim (100 \mu\text{m})^3$ . It is also necessary to soften the spatial inhomogeneities of the control MW and RF pulses so that they could control the entire ensemble as uniformly as possible. Despite these technical difficulties in implementation and the long measurement time required for repeated readings, the ancilla-assisted repetitive readout can be considered a promising method that can increase the sensitivity of ensemble measurements [38].

## 5.10 Geometric phase magnetometry

In addition to the dynamic phase, under the action of DC or RF magnetic fields, the NV center can accumulate a geometric phase [60]. The possibility of controlling and reading the geometric phase of the NV center was demonstrated in [61], [62], [63], [64], [65]. A protocol using geometric phase measurements for DC magnetometry is presented in [66] (Figure 19). During the measurement interval, divided into two parts by a  $\pi$ -pulse, the phase of MW Rabi drive sweeps adiabatically along a closed phase-space loop. The  $\pi$ -pulse helps to get rid of the accumulated dynamic phase, while the geometric phase carries information about the magnetic field. The sensitivity of this method does not exceed the sensitivity of the optimized Ramsey method, but it avoids the  $2\pi$ -phase ambiguity inherent to the Ramsey method and, therefore, makes it possible to measure the field in a wide dynamic range [38].

A comparison of the concepts of magnetic field measurements using dynamic and geometric phases is shown in Figure 19. In the case of magnetometry using the dynamic phase, the Bloch vector  $\mathbf{s} = (s_x, s_y, s_z)$ , shown by the blue arrow, precesses around a fixed Larmor vector  $\mathbf{R} = (0, 0, \gamma B)$  shown by the red arrow. During the precession time  $T$ , a dynamic phase proportional to the magnetic field accumulates between two  $\pi/2$  pulses ( $\phi_d = \gamma B T$ ). After that, it is converted into the population difference ( $P = \cos(\phi_d)$ ) and optically readout. This method leads to an ambiguous result due to the  $2\pi$ -periodicity of the phase. An infinite number of magnetic field values give the same signal (shown as black dots in the). The measurement of the magnetic field using the geometric phase uses the Berry sequence. In this case, after preparing the Bloch vector by transferring the spin state to a superposition using a  $\pi/2$  pulse, an additional non-resonant excitation rotates the Larmor vector  $N$  times around the  $z$  axis:  $\mathbf{R}(t) = (\Omega \cos \rho(t), \Omega \sin \rho(t), \gamma B)$ ,  $\rho(t) = 4\pi N t/T$ . As a result, the spin acquires a geometric phase proportional to the solid angle described by the Larmor vector  $\phi_g = N 2\pi (1 - \cos \theta)$  and the number of rotations  $N$ . In the middle of the measurement interval, after applying a  $\pi$



-pulse that cancels the dynamic phase, the direction of rotation of the Larmor vector changes to the opposite to double the geometric phase. Finally, the accumulated phase is converted into an optically readable population difference  $P = \cos\phi_g$ . The received signal is the chirped oscillation depending on the amplitude of the magnetic field, which, due to the slope changing with the magnetic field, does not lead to uncertainty [38].

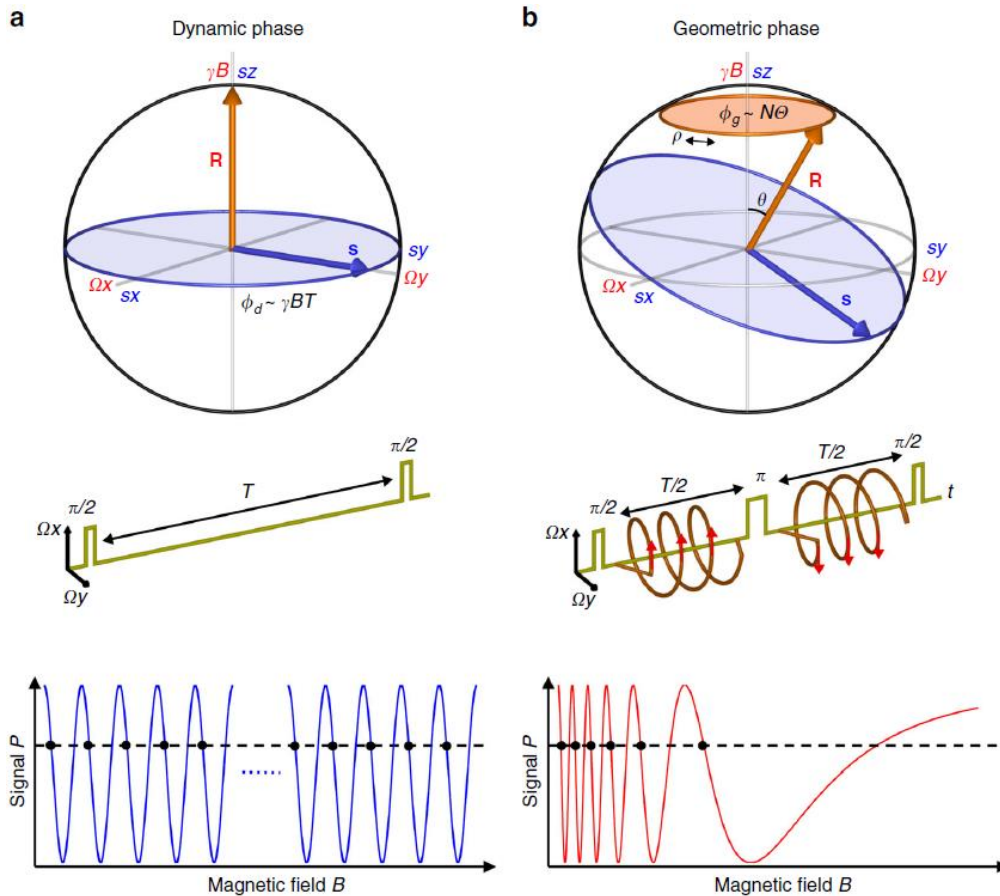


Figure 19. Geometric phase magnetometry

Comparison of dynamic and geometric phase magnetometry. For dynamic phase magnetometry (i.e., Ramsey), the Bloch vector (blue arrow) is optically prepared and then rotated by a  $\pi/2$  pulse to the equator. The Bloch vector then precesses about the fixed Larmor vector (orange arrow) before being mapped into a population difference by a second  $\pi/2$  pulse and read out optically. (b) For geometric phase magnetometry, the Bloch vector is optically prepared and then rotated to the equator. Additional off-resonant driving then rotates the Larmor vector about the z axis. As the spins precess, a geometric phase proportional to the product of the solid angle (orange disk) and the number of Larmor vector rotations is acquired in addition to the dynamic phase. To cancel the dynamic phase while continuing geometric phase accrual, a  $\pi$  pulse and a reversal of the off-resonant drive are inserted at the sequence midpoint. Last, the Bloch vector is mapped onto a population difference by a second  $\pi/2$  pulse and read out optically Source: [66], [38].

### 5.11 Summarized representation of different NV measurement protocols

The main feature that distinguishes various measurement protocols is the spectral characteristics of the fields that can be measured by them. In Table 4 measurement protocols are generalized into two categories. The first category includes DC protocols designed to measure either static or weakly changing fields, or broadband near-DC signals. The second category includes protocols sensitive to alternating AC fields, which measure narrowband signals with frequencies up to  $\sim 10$  MHz. The possibility of their use for some special applications at frequencies up to  $\sim 100$  MHz was also experimentally shown. The sensitivity of both types of protocols is limited by the spin relaxation times of NV centers. So, in the case of DC measurements, the sensitivity



depends on the dephasing time  $T_2^*$  of the ensemble (usually on the order of 1  $\mu\text{s}$ ), and the sensitivity of AC measurements is determined by the coherence time  $T_2$  (exceeding  $T_2^*$  by 1-2 orders of magnitude). By using dynamic decoupling protocols, the characteristic time of AC sensing can be extended up to the longitudinal spin relaxation time  $T_1$  [67]. However, such an increase in the characteristic time and, as a result, the sensitivity of these protocols, leads to a limitation of their application to the measurement of narrow-band AC fields. Relaxometry protocols that allow phase-insensitive measurements of signals at frequencies of  $\sim\text{GHz}$  are also limited by the time  $T_1$  [38].

**Table 4.** Operational regimes and selected applications of broadband DC and AC sensing protocols employing  $\text{NV}^-$  ensembles in diamond. Source: [38].

	Broadband dc sensing	ac sensing
Common techniques	Ramsey cw-ODMR pulsed ODMR	Hahn echo, dynamical decoupling
Relevant relaxation	Inhomogeneous spin dephasing ( $T_2^*$ )	Homogeneous spin decoherence ( $T_2$ ) and longitudinal relaxation ( $T_1$ )
Frequency or bandwidth	0 to $\sim 100$ kHz (pulsed), 0 to $\sim 10$ kHz (cw)	Center frequency $\sim 1$ kHz to $\sim 10$ MHz; bandwidth $\lesssim 100$ kHz
Example magnetic sensing applications	Biocurrent detection, magnetic particle tracking, magnetic imaging of rocks and meteorites, imaging of magnetic nanoparticles in biological systems, magnetic imaging of electrical current flow in materials, magnetic anomaly detection, navigation	Single biomolecule and protein detection, nanoscale nuclear magnetic resonance, nanoscale electron spin resonance, magnetic resonant phenomena in materials, noise spectroscopy

Schematically, the various types of protocols considered are systematized in Figure 20. It displays, commonly used in protocols timing schemes and durations of initiating and readout laser pulses and driving MW pulses, the frequency characteristics of the fields measured by them, as well as of the bias fields. Arrows indicate swept parameters, straight lines indicate static fields and swept static bias fields for  $T_1$  relaxometry and Rabi sensing, and sinusoids indicate variable measured fields, which are very high-frequency in the case of relaxometry and Rabi sensing [32].

	CW ODMR	Pulsed ODMR	Ramsey	Hahn echo	Dynamical decoupling	Rabi	$T_1$ relaxometry
Laser							
Microwave							
Readout							
Bias field							
Sample field							
Swept parameter	Microwave frequency	Microwave frequency	Free precession time, $\tau$	Spin evolution time, $\tau$	Spin evolution time, $\tau$	Microwave pulse duration, bias field	Laser pulse delay, bias field

Figure 20. NV measurement protocols. Source: [32].

## 6. CHARACTERISTIC COHERENCE TIMES FOR NV CENTERS

NV centers and their ensembles are characterized by the following specific times, which limit the possibilities of their use both in magnetometry and for other applications [32]:

1.  $T_1$  – the time of longitudinal spin relaxation – is an intrinsic characteristic of the NV sensor, in the case of ensembles, it depends on the density and the depth of the NV centers;
2.  $T_2^*$  – dephasing time – determines the width of the ODMR spectral line, limits the phase accumulation time for the Ramsey method, sets the spectral filter function for Rabi and relaxometry sensing;
3.  $T_2$  – coherence time – in protocols with dynamic decoupling, it limits the phase accumulation time, which depends on the pulse sequence and the magnetic noise spectrum, in extreme cases it can reach the value of  $T_1$ .

The characteristics of these times and methods for measuring them are described in the following subsections.

### 6.1 $T_1$ Relaxation time

The spin relaxation time of the NV center  $T_1$ , sometimes called the spin-lattice relaxation time, is the time during which the spin polarized either by a green laser into the state  $m_S=0$  or by an MW  $\pi$ -pulse into the states  $m_S = \pm 1$  decays to the state of thermal equilibrium because of the interactions with phonons of the diamond lattice. Due to the effect of phonons, the spin-lattice relaxation time  $T_1$  is temperature sensitive [41].

The following protocol is used to measure the relaxation time  $T_1$  (Figure 21). A laser pulse brings the NV center to the  $m_S = 0$  state, and after some variable waiting time  $\tau$ , another laser pulse reads the fluorescence depending on the spin state of the NV center. If, after spin polarization to the state  $m_S = 0$ , an optional MW  $\pi$ -pulse is applied, it will transfer the spin of the NV center to one of the  $m_S = \pm 1$  states. This version of relaxometry makes it possible to measure the decay from the states  $m_S = +1$  or  $m_S = -1$ . Plotted as a function of  $\tau$ , the fluorescence intensity exhibits an exponential decay [16].

To find the relaxation time, the resulting graph can be fit to the following equation, in which  $P$  is the time-varying polarization, and  $P_0$  is the maximum polarization after the spin state initiation [16]

$$P(\tau) = P_0 e^{-\tau/T_1}. \quad (\text{Eq. 6.1})$$

Thus,  $T_1$  is the time during which the population decrease  $e$  times ( $\approx 37\%$ ) from its initial state under the influence of lattice phonons [16].

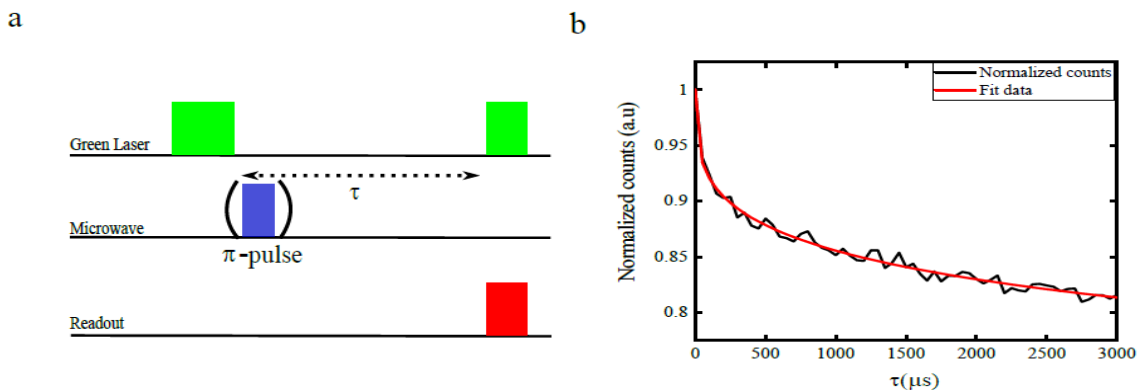


Figure 21. Spin-phonon relaxation time.

Figure a) shows schematic diagram of the pulse sequence to measure  $T_1$  time measurement. In figure b) an example graph for  $T_1$  time measurement with single NV center is shown. Source: [16].

## 6.2 $T_2$ coherence time

The spin coherence time of the center NV  $T_2$  is the time it takes for the spin to lose its coherence. It is determined by the interaction with spin impurities in diamond, such as the nuclear spins of the  $^{13}\text{C}$  isotope, the electronic spins of donor nitrogen, and, in cases where dense ensembles are used, the spins of neighboring NV centers. While the  $T_1$  relaxation is a spin-lattice process,  $T_2$  is a spin-spin process, so  $T_2$  is sometimes referred to as the spin-spin relaxation time. For the different NV centers in a diamond sample, this time can vary significantly due to its dependence on the local spin environment [16].

To measure the coherence time  $T_2$ , the Hahn pulse echo method is used (Figure 22). After the laser pulse initiates the NV center spin to the state  $m_S = 0$ , by applying the MW  $\pi/2$ -pulse, it is transferred to the superposition of the states  $m_S = 0$  and  $m_S = +1$ . Then, during the time  $\tau/2$ , the system freely evolves, accumulating the phase due to the fluctuations of the magnetic field caused by the local spin bath. If these fluctuations are slow on a time scale of  $\tau/2$ , then the next MW  $\pi$ -pulse will result in phase refocusing after a new free precession time period of  $\tau/2$ . Thus, after two free evolution times  $\tau/2$ , the spin of the NV center gets decoupled from the weakly fluctuating noise. Then the spin state of the NV center is transferred by a new MW  $\pi/2$ -pulse to the measured state and read out by the second laser pulse. For noises with frequencies higher than that determined by the period of free precession  $\tau$  refocusing will not work effectively [16].

By gradually increasing the free precession time  $\tau$ , the dependence of the intensity of the collected fluorescence on  $\tau$  can be plot, which decreases exponentially, in accordance with the equation [16]:

$$I(\tau) = I(0)e^{(-\tau/T_2)^p} \quad (\text{Eq. 6.2})$$

Here  $I(\tau)$  – is the fluorescence collected after the period of free evolution  $\tau$ ;  $I(0)$  – is the initial maximum fluorescence,  $p$  – is a free parameter that depends on the type of noise, and  $T_2$  – is the coherence time [16].

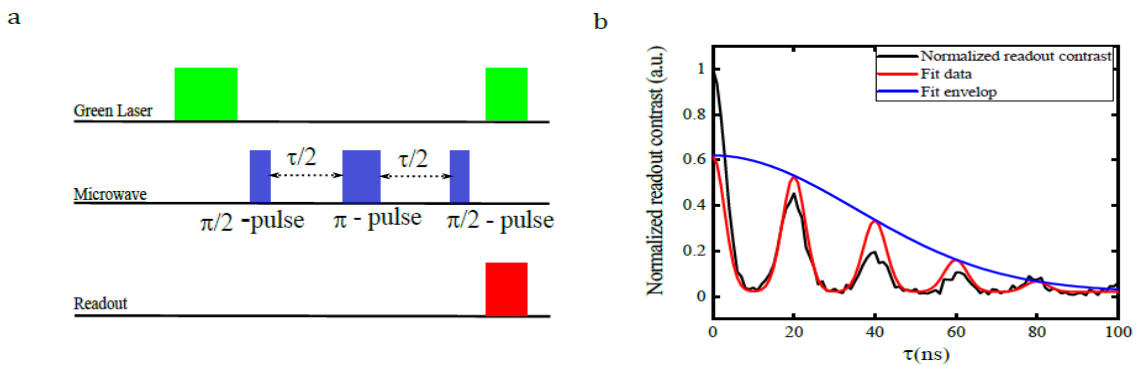


Figure 22. Hahn echo pulse scheme and graph.

Figure a) depicts Schematic diagram for Hahn echo pulse sequence. In figure b), an example graph for  $T_2$  time measurement with single NV center is shown. Source: [16].

As a rule, the dominant source of local field fluctuations is the Larmor precession of the  $^{13}\text{C}$  isotope nuclei located near the NV center spin. If the free evolution time period  $\tau$  is a multiple of the Larmor precession periods of  $^{13}\text{C}$  nuclei, the phase contributions from each individual  $^{13}\text{C}$  atom are compensated. As a result, collapses and revivals of the observed decoherence curve can be observed, which, in  $^{13}\text{C}$ -dominated samples, are a consequence of the dipole-dipole interaction. From such a plot, the true spin decoherence of the NV center can be obtained by plotting the envelope of the Larmor resonant peaks [16].

### 6.3 $T_2^*$ dephasing time

The dephasing time  $T_2^*$  in the nuclear magnetic resonance technique is usually called the time during which, due to inhomogeneities in the environment, a spin or an ensemble of spins are dephased. For the NV centers, the dominant inhomogeneities are the temporal fluctuations of the local magnetic field and the variations in the surrounding spin bath experienced by each NV center [16].

The Ramsey sequence is used to measure the dephasing time  $T_2^*$  of a single NV center (Figure 23 a). The resulting free induction decay (FID) Ramsey curve has an exponential decay and contains beats of the hyperfine nitrogen transitions. There are two such beats for the  $^{15}\text{N}$  nitrogen isotope and three for the  $^{14}\text{N}$  isotope (this case is shown in Figure 23 b). The FID envelope makes it possible to extract the NV center dephasing time  $T_2^*$  [16].

In the case of an ensemble of NV centers, different local spin environments cause inhomogeneities that broaden the frequency components of Ramsey FID hyperfine transitions. Also, changes in the electric field and in the temperature in the local medium, which affect each spin of the ensemble of NV centers in different ways, lead to the broadening of the frequency components. As a result, each spin of the NV ensemble is characterized by its resonance line width  $\Delta\nu$  and, consequently, by different  $T_2^*$ , because  $\Delta\nu \propto 1/T_2^*$ . Therefore, as can be seen in Figure 23 c, the three hyperfine transitions on the FID curve of the  $^{14}\text{NV}$  ensemble are poorly resolved, and do not allow reliable construction of the Ramsey fringes envelope. Thus, the Ramsey method in the case of an ensemble of NV centers does not allow to effectively determine the dephasing time  $T_2^*$  [16].

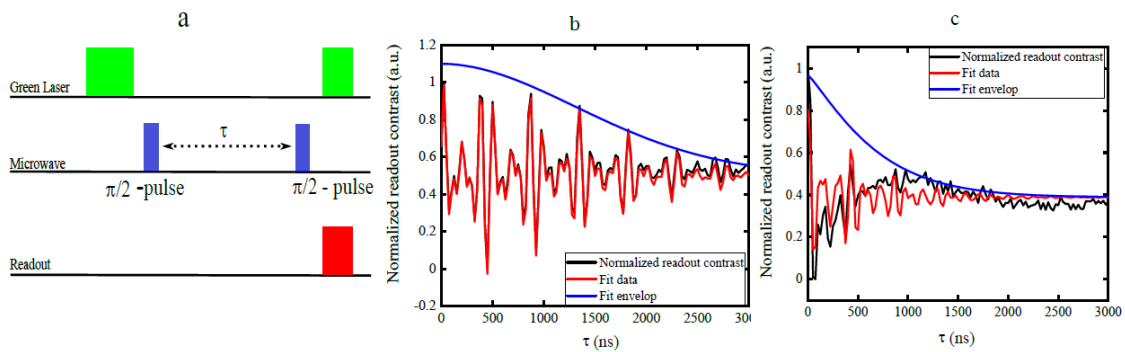


Figure 23. Dephasing time scheme and example graph.

In figure a), a schematic diagram for Ramsey pulse sequence is shown. Figure b), depicts an example graph for the Ramsey measurement performed with a single NV center. Figure c), shows graph of Ramsey measurement with NV ensemble shows that the Ramsey fringe fit is not at all fitting as in the case of single NV center shown in figure (b). For this reason, the  $T_2^*$  measurement for ensemble of NV centers is done in alternative method. Source: [16].

For the described reasons, another method is applied to find the dephasing time  $T_2^*$  of ensembles of NV centers [13]. This method uses ODMR spectra taken with a bias magnetic field carefully tuned so that hyperfine transitions can be clearly distinguished. Maintaining the laser power at the lowest possible level and gradually reducing the MW radiation power, a series of ODMR spectra for hyperfine transitions is obtained and the widths of their resonance lines are measured at the full width at half maximum (FWHM) of the spectral lines corresponding to these transitions. Then, by linear extrapolation of the resonance linewidths obtained for different MW powers, the value of the resonance linewidth at zero microwave radiation power ( $\Delta\nu$ ) is determined, which makes it possible to find the dephasing time using the relation [16]:

$$T_2^* = \frac{1}{\pi\Delta\nu}. \quad (\text{Eq. 6.3})$$



## 6.4 Typical coherence times

Figure 24 shows typical values of different characteristic times for the samples of the single NV centers grown by different methods and located in different spin environments [42]. Similar parameters for different NV samples are summarized in Table 5 (where 1 ppm corresponds to  $1.76 \times 10^{17} \text{ cm}^{-3}$  in the sample) [68].

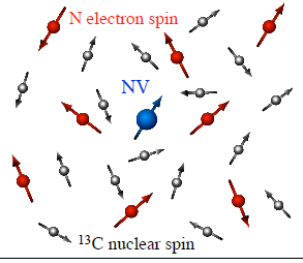
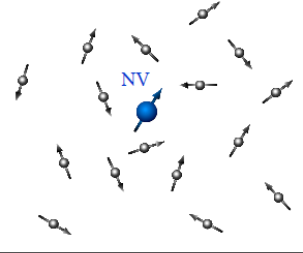
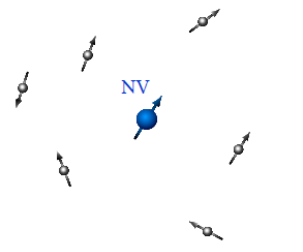
<p><b>HPHT</b></p> <p><math>[N] \sim 100 \text{ ppm}</math> <math>[^{13}\text{C}] = 1.1\%</math></p>		<p><math>T_2^* \sim 0.1 \mu\text{s}</math> <math>\eta_{dc} \approx 1.5 \mu\text{T} \cdot \text{Hz}^{-1/2}</math></p> <p><math>T_{2,\text{echo}} \sim 1 \mu\text{s}</math> <math>\eta_{ac} \approx 500 \text{ nT} \cdot \text{Hz}^{-1/2}</math></p>
<p><b>CVD</b></p> <p><math>[N] &lt; 1 \text{ ppb}</math> <math>[^{13}\text{C}] = 1.1\%</math></p>		<p><math>T_2^* \sim 3 \mu\text{s}</math> <math>\eta_{dc} \approx 300 \text{ nT} \cdot \text{Hz}^{-1/2}</math></p> <p><math>T_{2,\text{echo}} \sim 300 \mu\text{s}</math> <math>\eta_{ac} \approx 30 \text{ nT} \cdot \text{Hz}^{-1/2}</math></p>
<p><b><math>^{12}\text{C}</math> purified CVD</b></p> <p><math>[N] &lt; 1 \text{ ppb}</math> <math>[^{13}\text{C}] &lt; 0.01\%</math></p>		<p><math>T_2^* \sim 100 \mu\text{s}</math> <math>\eta_{dc} \approx 50 \text{ nT} \cdot \text{Hz}^{-1/2}</math></p> <p><math>T_{2,\text{echo}} \sim 2 \text{ ms}</math> <math>\eta_{ac} \approx 10 \text{ nT} \cdot \text{Hz}^{-1/2}</math></p>

Figure 24. Typical coherence times of single NV defect electron spins

Typical coherence times of single NV defect electron spins (blue arrow) hosted in different types of diamond crystals at room temperature with the corresponding magnetic field sensitivities  $\eta_{dc}$  and  $\eta_{ac}$ . The red arrows indicate the electron spin ( $S = 1/2$ ) of nitrogen impurities and the black arrows illustrate the nuclear spin of  $^{13}\text{C}$  atoms ( $I = 1/2$ ). The  $T_{2,\text{echo}}$  time is measured through standard spin-echo measurements, i.e. without applying multi-pulse dynamical decoupling protocols. The corresponding magnetic field sensitivities are obtained for a conventional detection of the NV defect PL, i.e. while using a large numerical aperture microscope objective. In such configuration the detected PL signal is  $\sim 2 \times 10^5$  counts/s. The coherence time is measured for native NV defect placed far away from the diamond surface. (ppm - part per million carbon atoms; ppb - part per billion carbon atoms) Source:[42].

**Table 5.** Summary of diamond sample parameters. Source: [68].

Type	Parameters				Temperature	$^{13}\text{C}$	concentration (ppm)
	$T_2^*$ (ns)	$T_2$ (SE) (ns)	$T_2$ (CPMG) (ns)	$T_1$			
HPHT	118				RT	Normal	16
CVD	291				RT	Normal	0.012
HPHT	$11 \times 10^3?$				RT	0.03	0.3
CVD	$18.2 \times 10^3$	$1.8 \times 10^6$			RT	0.3%	Single
Ntype	$1.5 \times 10^6$	$2.4 \times 10^6$	$3.9 \times 10^6$	7.4 ms	RT	0.002%	Single?
CVD			$6 \times 10^8$	>10 s	77 K	0.01%	0.00001
CVD			$5 \times 10^7$	>10 s	77 K	0.01%	0.01
CVD?	1 $\mu\text{s}$				RT	Normal	0.1
CVD		$631 \times 10^3$			RT	Normal	0.00015
CVD		$282 \times 10^3$			RT	Normal	0.0005
CVD		$92.6 \times 10^3$					Single
CVD	10 $\mu\text{s}$				RT	0.01%	3-4



## 7. SENSITIVITY

This chapter considers the main factors that affect the sensitivity of sensors based on NV centers. In the following subsections will be discussed the main sources of noise that are typical for sensors based on NV centers, the physical quantities to which these sensors are sensitive and whose change can also affect the sensitivity of measuring of other physical quantities in various regimes and conditions. Methods for improving the sensitivity are also presented, which can be applied both at the stage of manufacturing sensors and at the stage of measurements through the use of various improved measurement techniques.

### 7.1 Spin projection noise and photon shot noise

As was noted earlier, the fundamental factor limiting the sensitivity of all quantum sensors is the spin projection quantum noise, which is a consequence of the internal statistical distribution of quantum measurements. Photon shot noise is added to it in cases where the reading of the spin state is carried out optically. The detection efficiency of the spin-selective photoluminescence, which is limited by the non-ideal quantum efficiency of the NV center radiative transition and the collection efficiency of the detecting optics, is about  $\epsilon \sim 10^{-3}$ . Thus, for most of the proposed magnetometry schemes based on NV sensors, photon shot noise prevails over spin projection noise [42].

### 7.2 Physical quantities which are measured by sensors on NV centers

Apart from the magnetic field measuring, various studies have demonstrated or proposed the application of NV center sensors to measure several other physical quantities:

- Magnetic moments (nuclear and electronic spins) [69];
- Electric fields [70], [45];
- Orientation [71];
- Temperature For variation of temperature the rate of change of the axial zero-field splitting parameter D is  $dD/dT=74.2 \text{ kHz/K}$  [54], [72];
- Pressure The rate of change with pressure (p) of the axial zero-field splitting parameter D is  $dD/dp=1,46 \text{ kHz/bar}$  [73];
- Strain [74], [37], [75], [76], [77].

The best sensitivities achieved are shown in Table 6.

**Table 6.** The best sensitivities achieved with sensors on NV centers.

Magnetic field	$0.43 \text{ pT} \times \text{Hz}^{-1/2}$	[78]
Electric field	$200 \text{ V} \times \text{cm}^{-1} \text{Hz}^{-1/2}$	[45]
Temperature	$76 \text{ mK} \times \text{Hz}^{-1/2}$	[79], [80]
Strain	$\sim 10^{-7} \text{ Hz}^{-1/2}$	[4], [77]
Orientation	$0.1^\circ \text{ Hz}^{-1/2}$	[71]
Pressure	$6.8 \text{ bar} \times \text{Hz}^{-1/2}$	[4][73]





For all these physical quantities, the limited by shot noise sensitivity of a single NV center sensor  $\eta_s$ , is determined by the dependence [31]:

$$\eta_s \propto \frac{1}{C_s \sqrt{RT_2^*}} \quad (\text{Eq. 7.1})$$

Here  $C_s$  – is the optical contrast, which depends on the intrinsic photophysical properties of the color defect and which for a single NV center is approximately  $C_s \approx 20\%$ , and  $R$  – is the number of registered photons [31].

### 7.3 Dependence on temperature

In magnetometric measurements using NV centers, it is necessary to take into account the non-linear temperature dependence of the zero-field splitting parameter  $D$ . At a room temperature, it is characterized with linearised thermal shift,  $dD/dT = -75 \text{ kHz/K}$  [54]. For DC measurements in the basis of  $\{|m_s=0\rangle; |m_s=+1\rangle\}$  used in most protocols, temperature shifts of  $D$  are indistinguishable from energy level splits caused by an external magnetic field, which makes it difficult for the magnetometer to operate accurately. Thus, the level shift caused by a change in the ambient temperature by only 10 mK is equivalent to the shift caused by a change in the magnetic field by  $\sim 30 \text{ nT}$ . As shown in [56], the use of magnetometric protocols involving the  $\{|m_s= -1\rangle; |m_s=+1\rangle\}$  basis helps to overcome the problem of the temperature dependence of the parameter  $D$ , since in this case, temperature fluctuations affect the measured level splitting only in the second order. In addition, the observed temperature dependence of the zero-field splitting parameter  $D$  is applied in thermometry based on NV centers [72].

### 7.4 Ways to improve sensitivity

The sensitivity can be improved by the following methods [31].

- 1) Improving the collection efficiency of the resulting photoluminescence [38].
- 2) With the help of such additional methods for increasing the accuracy of registration of the spin states as
  - infrared absorption readout [81];
  - photoelectric detection [82];
  - spin-to-charge conversion [57].
- 3) Increasing the spin dephasing time  $T_2^*$ . This is the only parameter that makes it possible to optimize the sensitivity of NV center sensors at the stage of preparing of the initial diamond samples, since it is determined mainly by the magnetic interactions with the paramagnetic impurities located inside or on the surface of the diamond [31].
 

In order to achieve a long dephasing time, the produced diamond samples should have the most ideal spinless lattice possible and be characterized by an extremely low impurity content. Also, due to the action of the induced surface electron spin bath, the state of charge and the coherence time of the NV centers are strongly affected by the distance between the NV centers and the diamond surface. Some of the negative surface effects can be mitigated by specific chemical terminations and special surface treatments [31].
- 4) Also, in the case of AC sensing, the sensitivity can be improved by applying the dynamical decoupling protocols that increase the characteristic time of the sensor to a coherence time  $T_2$ , which exceeds the dephasing time  $T_2^*$  by several orders of magnitude [38].



5) Increasing the number of NV centers in imaging applications allows to improve the sensitivity in a simple way. Though, the best spatial resolution is provided by a single NV center. The shot noise-limited sensitivity for an ensemble of N defects  $\eta_e$  is defined as [31]:

$$\eta_e \propto \frac{1}{C_e \sqrt{NRT_2^*}} \quad (\text{Eq. 7.2})$$

Therefore, increasing the density of the NV centers, as well as maintaining high spin coherence, is the main task from the point of view of material science. However, such an increase in sensitivity can be accompanied by a decrease in the contrast of spin readout, since the orientation of the NV centers is equally probable in all four directions, but only a quarter of them make a useful contribution to the recorded signal. Due to background luminescence, both from misaligned NV centers, and from other impurities, or neutrally charged  $NV^0$  defects, for large NV ensembles, the spin readout contrast usually drops to  $C_e \approx 1\%$  [31].

The spin readout contrast of the NV ensembles can be improved in the following ways [31]:

1. at the stage of a crystal growing, to create a diamond with a predominant orientation of NV centers along a certain axis;
2. to increase the conversion efficiency of the neutrally charged ( $NV^0$ ) to negatively charged ( $NV^-$ ) centers.

## 7.5 Diamond growth technique to optimize the performance of NV-based quantum sensing

To optimize the performance of quantum measurements using NV centers, it is necessary to solve the following problems [31]:

1. Further reduction of decoherence by improving the technology of diamond matrix growth, which has already achieved significant success through isotopic purification and defect engineering, but is still far from reaching the theoretical limit of coherence time ( $T_1$ ), especially for the samples with high nitrogen concentration or for near-surface NV centers.
2. Strict control over the density and state of charge of the formed NV centers. To improve sensitivity, for many applications that work with the dense NV ensembles, the ratio between NV centers and other nitrogen-containing defects is critical. Apart from this, the environment of the defect should contribute to a higher probability of a negative charge of the NV center state than of a neutral one.
3. Creation of crystals with a preferred orientation of NV centers, which technically simplifies the operation of the device, increases the sensitivity and limits the background noise.
4. Control over the spatial localization of the created defects or their ensembles in-plane and in-depth, which allows to include them in nanostructures or cavities and improve the characteristics of wide-field NV ensemble imaging.

Various technological methods for creating diamond samples optimized for highly sensitive NV ensemble magnetometry are summarized in the Table 7 [38].



**Table 7.** Summary analysis of diamond engineering parameters and methods for high-sensitivity ensemble-NV<sup>-</sup> magnetometry. Colored lines indicate methods that may be employed to optimize each parameter. Source: [38].

Diamond material optimization		
Parameter optimized	Method	Method description and evaluation
N-to-NV conversion efficiency $\chi$	CVD synthesis	Common synthesis method that can produce high-quality ensemble-NV diamonds. Relatively easy to control dimensions and concentrations of electronic and nuclear spins. May introduce strain and unwanted impurities, which can limit achievable $\zeta$ , $\chi$ , and $T_2^*$ . Effective for producing NV <sup>-</sup> -rich-layer diamonds.
NV-to-NV <sup>-</sup> charge state efficiency $\zeta$	HPHT synthesis	Common synthesis method that can produce high-quality ensemble-NV diamonds with lower strain and fewer lattice defects than CVD. Control over doping and impurity concentration may be more difficult than in CVD. Not intrinsically amenable to creating NV <sup>-</sup> -rich-layer diamonds. Ferromagnetic metals may incorporate into diamond.
Paramagnetic impurities	Irradiation	Diamond treatment method that, combined with subsequent annealing, converts substitutional nitrogen to NV centers. Electrons are preferred irradiation particle. Dose should be optimized for diamond's nitrogen concentration to create high $\zeta$ without degrading $\chi$ . Generally recommended with annealing for producing NV <sup>-</sup> -rich diamonds.
Strain	LPHT annealing	Low-pressure annealing that, combined with prior irradiation, converts substitutional nitrogen to NV centers. Heals some diamond lattice damage. NV <sup>-</sup> centers are created effectively at $\sim 800$ °C; additional treatment at $\sim 1200$ °C may eliminate some unwanted impurities. Generally recommended with irradiation for producing NV <sup>-</sup> -rich diamonds.
Nuclear spins	HPHT treatment	High-pressure annealing may reduce strain and eliminate some unwanted impurities. May enable increases in $\zeta$ and $\chi$ . Recommended for diamonds with balanced aspect ratios.
	Isotopic enrichment	Diamond synthesis with isotopically enriched source (gas for CVD and typically solid for HPHT) allows reduction of unwanted nuclear spin concentration (e.g., <sup>13</sup> C) and selection of nitrogen isotope ( <sup>14</sup> N or <sup>15</sup> N) incorporated into NV <sup>-</sup> . CVD diamonds with [ <sup>13</sup> C] $\approx 20$ ppm have been synthesized. Recommended for achieving long $T_2^*$ .
	Surface treatment	Surface termination with favorable atomic elements can stabilize the desired NV charge state near the surface and extend relaxation times. Generally recommended.
	Preferential orientation	CVD synthesis of diamond with NV centers preferentially oriented along a single axis. At present, preferential orientation is only maintained in unirradiated diamonds, largely hindering its capability to produce NV <sup>-</sup> -rich diamonds. Not generally recommended.

## 7.6 Engineering NV defects close to surfaces

In order to minimize the distance between the sensor and the measured object, highly coherent NV defects must be located within a few nanometers from the diamond surface. The proximity of sensitive NV centers to the surface is extremely important for practical applications of NV magnetometry, since dipole magnetic fields decay with distance as the third inverse power [42].

To create NV centers at specified depths and in controlled locations, the ion implantation method is most often used, followed by high-temperature annealing [33]. However, this method has a number of disadvantages such as “ion straggling” (internal uncertainty of the resulting depth associated with the randomness of the ion scattering process, proportional to the square root of the implantation depth) [26]; low (compared to the natural defects) spin coherence, especially at shallow depths ( $\leq 20$  nm); low efficiency of conversion of implanted nitrogen atoms into NV centers at low implantation energies used to create defects at shallow depths (1% NV yield at the depths  $< 8$  nm) [23], which leads to a deterioration of the spin coherence and productivity of the shallow NV centers [42].

To solve some of these problems, alternative methods are being sought for producing defects in diamond, such as the method proposed in [24], of “ $\delta$ -doping” of diamond with nitrogen at a precisely defined depth directly during diamond growth. In this experiment an NV layer was obtained at a depth of 5 nm with a thickness of 2 nm, characterized by  $T_2 > 100$   $\mu$ s [42].



## 7.7 Sensitivity of CW-ODMR method for DC magnetic fields

The sensitivity for the case of measuring of an external DC magnetic field by the simplest ODMR method is determined by fixing the MW frequency at the maximum slope of one of the EPR PL dips, where the optimal response of the spin-dependent signal to a constant magnetic field can be obtained. Thus, an infinitely small variation of the magnetic field  $\delta B$  during the measurement time  $\Delta t$  will lead to the following change in the fluorescence of the NV center:  $\left(\frac{\partial I_0}{\partial B}\right) \times \delta B \times \Delta t$ . Here  $I_0$  is the NV defect PL rate. The readout noise, mainly determined by the photon shot noise, is:  $\sqrt{I_0 \times \Delta t}$ . The magnetic field sensitivity, limited by photon shot noise and defined as **the minimum DC magnetic field detectable at a signal-to-noise ratio of unity**, is obtained by comparing of these two expressions [42]:

$$\eta = \delta B \sqrt{\Delta t} = \frac{\sqrt{I_0}}{(\partial I / \partial B)} \approx \frac{h}{g\mu_B} \frac{\Delta\nu}{C\sqrt{I_0}}. \quad (\text{Eq. 7.3})$$

Here  $\Delta\nu$  is the width of the EPR resonance line and  $C$  is the optical contrast (Figure 7 c). The way to improve the sensitivity to a magnetic field lies through an increase in the detection efficiency PL NV center  $I_0$  or a decrease in the width of the resonance line  $\Delta\nu$ , since the optical contrast, as was noted earlier, can hardly be changed, because this parameter is determined by the intrinsic photophysical properties of the NV center (the non-ideal branching ratio to the singlet states) and for a single NV center is approximately  $C \approx 20\%$  [42].

## 7.8 Sensitivity for a Pulsed ODMR and Ramsey-type NV magnetometry

The use of the Ramsey sequence makes it possible to improve the sensitivity to the magnetic field by increasing the free precession time  $\tau$ , during which the phase  $\phi$ , which depends on the measured magnetic field, is accumulated. But such an increase in  $\tau$  entails a decrease in the spin readout contrast, due to the influence of the magnetic field noise created by the environment of the NV center and randomizing  $\phi$  in time with the time constant  $T_2^*$ . It is shown that at  $\tau \approx T_2^*$  the optimal sensitivity determined by these two competing factors is achieved [83]. In addition, since in this scheme the readout laser does not act constantly, the rate of detected photons is reduced by the duty cycle of laser pulses  $t_L/\tau$ , where  $t_L$  is the duration of the readout laser pulse, usually set to  $\approx 300$  ns, in order to optimize the contrast of the readout signal, and the duration of the free precession interval is  $\tau \approx T_2^*$ . Thus, the time-averaged rate of detected photons is  $I_0 t_L / T_2^*$ . Introducing these coefficients into equation (7.3), we obtain the optimized value of the sensitivity to the DC magnetic field [42]:

$$\eta_{dc} \sim \frac{\hbar}{g\mu_B} \frac{1}{C\sqrt{I_0 t_L}} \times \frac{1}{\sqrt{T_2^*}} \quad (\text{Eq. 7.4})$$

A similar sensitivity to a magnetic field can, as was noted earlier in section 5.2, be demonstrated by the Pulsed ODMR method. The sensitivity obtained by this method in [49] for pure diamond samples with  $T_2^* \approx 100$   $\mu\text{s}$  is  $\eta_{dc} \approx 40$  nT Hz<sup>-1/2</sup> [42].

More general formula for determining the sensitivity of Ramsey-like measurement sequences, derived for measurements using an ensemble of NV centers and taking into account the possibility of using different measurement bases ( $\{m_s=0; m_s=\pm 1\}$  or  $\{m_s=-1; m_s=+1\}$ ) is given in [38]:



$$\eta_{\text{Ramsey}}^{\text{ensemble}} \approx \underbrace{\frac{\hbar}{\Delta m_s g_e \mu_B \sqrt{N} \tau}}_{\text{spin projection limit}} \underbrace{\frac{1}{e^{-(\tau/T_2^*)^p}}}_{\text{spin dephasing}} \underbrace{\sqrt{1 + \frac{1}{C^2 n_{\text{avg}}}}}_{\text{readout}} \underbrace{\sqrt{\frac{t_I + \tau + t_R}{\tau}}}_{\text{overhead time}} \quad . \quad (\text{Eq. 7.5})$$

Here:

$N$  – the number of NV centers in the ensemble;

$\Delta m_s = 1$  in the case of using an effective subspace with  $S = 1/2$ , and the basis of  $\{m_s=0; m_s=\pm 1\}$ ;

$p$  – is the stretched exponential parameter, which depends on the source of dephasing and is equal to 1 for resonant lines that have the shape of a Lorentzian and 2 for resonant profiles that can be approximated by a Gaussian;

$C = (a - b)/(a + b)$  – is the measurement contrast characterizing the visibility of the Ramsey interference fringe;

$a$  and  $b$  – are the average numbers of photons received from the states  $m_s = 0$  and  $m_s = \pm 1$ , respectively, from one NV center during one count;

$n_{\text{avg}} = (a + b)/2$  – the average number of photons collected per NV center per measurement;

$t_I$  – the spin-state initialization time;

$t_R$  – the readout time;

$\tau$  – the interrogation free-precession time.

## 7.9 Sensitivity to AC magnetic fields

AC magnetic fields measuring methods, such as the Hahn-echo dynamic decoupling method mentioned in the sections 5.5 and 6.2, by introducing additional  $\pi$ -pulses in the middle of the free precession interval, remove the quasi-constant noise accumulated during the previous part of the interval, induced by paramagnetic impurities that exist in the crystal. Even better results are obtained by using more complex schemes, such as Carr-Purcell-Meiboom-Gill (CPMG) pulse sequences [84], [85] which, by periodically flipping the direction of the sensitive spin, further reduce the inhomogeneous dephasing. As a result, the spin coherence time exceeds  $T_2^*$  by several orders of magnitude, which leads to a significant increase in the sensitivity of NV center sensors to alternating magnetic fields [83]:

$$\eta_{ac} = \eta_{dc} \sqrt{\frac{T_2^*}{T_2}} \quad . \quad (\text{Eq. 7.6})$$

Under ambient conditions, for a single NV center in ultrapure diamond, it was possible to achieve  $T_2 \approx 2$  ms, and a sensitivity to an alternating magnetic field  $\eta_{ac} \approx 10$  nT Hz<sup>-1/2</sup> [46], which makes it possible to measure the field from a single electron spin at room temperature or to detect the small ensembles of nuclear spins. However, the described method is effective only if the frequency of oscillations of the measured alternating magnetic field coincides with the frequency of the applied pulse sequence. Nevertheless, variations of this basic method are possible, using advanced multi-pulse sensing sequence protocols that allow the measurement of fluctuating (incoherent) magnetic fields [42].



## 7.10 Parameters limiting sensitivity

The following parameters limit a sensitivity for sensing methods [38]:

1. Dephasing time  $T_2^*$ . In currently implemented applications, designed for broadband magnetometry using ensembles of NV centers, this parameter, as a rule, is  $T_2^* \lesssim 1 \mu\text{s}$ , which is many times less than the physical limit for this value –  $T_2^* \leq 2T_1$ . Indeed, for NV ensembles with a longitudinal relaxation time  $T_1 \approx 6 \text{ ms}$ , the maximum theoretically achievable dephasing time would be  $T_2^* \approx 12 \text{ ms}$ , which would lead to an increase in sensitivity by about  $\approx 100$  times.
2. Readout fidelity  $F$ . Another effective method of increasing the sensitivity is to increase the readout fidelity  $F = 1/\sigma_R$ , since improving the fractional fidelity leads to the same fractional sensitivity improvement. Here, the parameter quantifying the readout noise  $\sigma_R=1$  when the readout noise is defined only by the spin projection noise and  $\sigma_R>1$  when there are other added noises contributing to the readout imperfection. Considering that for commonly used methods of fluorescence readout at 532 nm the readout fidelity  $F$  for NV ensembles is  $\geq 67$  times less than the theoretical limit due to spin projection noise (i.e.,  $\sigma_R=1$  and  $F=1$ ) it can be concluded that significant improvements in this parameter can be made and, consequently, in the sensitivity of measurements. For example, multiple readout methods when working with single NV centers show  $\sigma_R < 5$ , reaching  $\sigma_R = 1.1$ .
3. Number of the sensors  $N$ , density of the sensors, and interrogation volume. Despite the fact that theoretically the number of sensors  $N$  can be increased without restrictions, a number of practical considerations prevent this. Many technical noises, such as noise from fluctuations in the intensity of the excitation laser or noise from timing jitter in the electronics of the device scale as the number of photons, which, in turn, scale as the number of sensors in the ensemble  $N$ . As a result, to obtain a sensitivity limited by photon shot noise with increasing of  $N$ , becomes difficult as photon shot noise scales slower (like  $\sqrt{N}$ ). Since the number of photons needed to initialize the spins increases linearly with  $N$ , another problem with large ensembles is the need to impractically increase the laser power. An increase in  $N$  can be achieved by increasing either the sensor density or the interrogation volume. Both approaches are associated with various difficulties – fundamental or technical. By increasing the density of NV centers, we increase the dephasing caused by dipolar coupling and decrease the  $T_2^*$ . Increasing the interrogation volume, on the other hand, will tighten the requirements for the uniformity of the driving MW field in order to equally manipulate the spins and the bias magnetic field (to maintain  $T_2^*$ ), and also increase the cost of the diamond. In addition, as  $N$  increases, the spatial resolution deteriorates. Considering that the sensitivity is scale as  $1/\sqrt{N}$ , the gain in sensitivity with increasing  $N$  will not be so significant. We can expect to get about a fivefold increase in sensitivity in this way. Existing devices exploit no more than a few percent of the NV centers contained in the bulk diamond, which leads to doubts about the prospects of increasing  $N$  for practical applications.
4. The measurement overhead time  $t_o = t_i + t_r$ . It is expected that by reducing the overhead time to an achievable value of  $\sim 1 \mu\text{s}$ , the sensitivity can increase by about  $\lesssim 3$  times, under the condition  $T_2^* \sim t_o$ .
5. Precession rate. The relative precession rate can be doubled compared to applying the standard equivalent  $S = 1/2$  subspace by using the full  $S = 1$  spin of the NV center, i.e.,  $\Delta m_S = 2$ . But, since the spin dynamics of the NV center is fixed, further improvement is unlikely.

An analysis of the proposed and applied methods for increasing the sensitivity of NV ensembles to a magnetic field is summarized in Tables 8 and 9 [38].



**Table 8.** Dephasing time  $T_2^*$  optimization. Source: [38].

Method	Method description and evaluation
Double-quantum (DQ) coherence magnetometry	Doubles effective gyromagnetic ratio. Removes dephasing from mechanisms inducing shifts common to the $ m_s = \pm 1\rangle$ states, such as longitudinal strain and temperature. Minor additional MW hardware usually required. Generally recommended.
Bias magnetic field	Suppresses dephasing from transverse electric fields and strain at bias magnetic fields of several gauss or higher. Generally recommended.
Spin-bath driving	Mitigates or eliminates dephasing from paramagnetic impurities in diamond. Each impurity's spin resonance must be addressed, often with an individual rf frequency. Additional rf hardware is required. Recommended for many applications.
Dynamical decoupling	Refocuses spin dephasing using one or more MW $\pi$ pulses, extending the relevant relaxation time from $T_2^*$ to $T_2$ , with fundamental limit set by $2T_1$ . Recommended for narrow band ac sensing; generally precludes dc or broadband magnetic sensing.
Rotary echo magnetometry	Extends measurement time using a MW pulse scheme but offers reduced sensitivity relative to Ramsey. Not recommended outside niche applications.
Geometric phase magnetometry	Offers increased dynamic range, using a MW spin-manipulation method, at the cost of reduced sensitivity relative to Ramsey. Not recommended outside niche applications.
Ancilla-assisted upconversion magnetometry	Employs $NV^-$ hyperfine interaction to convert dc magnetic fields to ac fields to be sensed using dynamical decoupling. Operates near ground-state level anticrossing ( $10^3$ G) and offers similar or reduced sensitivity relative to Ramsey. Not generally recommended.

**Table 9.** Readout fidelity optimization  $F=1/\sigma_R$ . ( $\sigma_R = 1$  corresponds to readout at the spin-projection limit.). Source: [38]

Spin-to-charge conversion readout	Maps spin state to charge state of NV, increasing number of photons collected per measurement. Allows $\sigma_R \approx 3$ for single NV centers, and initial results show improvement over conventional readout for ensembles. Substantially increased readout time likely precludes application when $T_2^* \lesssim 3 \mu s$ . Requires increased laser complexity. Technique is considered promising; hence, further investigation is warranted.
Ancilla-assisted repetitive readout	Maps $NV^-$ electronic spin state to nuclear spin state, enabling repetitive readout and increased photon collection. Allows $\sigma_R$ to approach 1 for single NVs; no fundamental barriers to ensemble application. Substantially increased readout time likely precludes application when $T_2^* \lesssim 3 \mu s$ . Requires high magnetic-field strength and homogeneity. Technique is considered promising, although further investigation is warranted.
Improved photon collection	Improves $\sigma_R$ by reducing fractional shot noise contribution, subject to unity collection and projection noise limits. Near 100% collection efficiency is possible in principle, making this mainly an engineering endeavor. While many schemes are incompatible with wide-field imaging, the method is generally recommended for optical-based readout of single-channel bulk sensors.
NIR absorption readout	Probabilistically reads out initial spin populations using optical absorption on the $^1E \leftrightarrow ^1A_1$ singlet transition. Demonstrated $\sigma_R$ values are on par with conventional ensemble readout, and prospects for further improvement are unknown. Technique is best used with dense ensembles and an optical cavity but is hindered by non- $NV^-$ absorption and nonradiative $NV^-$ singlet decay. Further investigation is warranted.
Photoelectric readout	Detects spin-dependent photoionization current. Best for small 2D ensembles; has not yet demonstrated sensitivity improvement with respect to optimized conventional readout.
Level-anticrossing-assisted readout	Increases the number of spin-dependent photons collected per readout by operation at the excited-state level anticrossing. Universally applicable, but at best offers a $\sqrt{3}$ improvement in $\sigma_R$ . Not recommended outside niche applications.
Green absorption readout	Probabilistically reads out initial spin populations using optical absorption on the $^3A_2 \leftrightarrow ^3E$ triplet transition. Performs best with order unity optical depth. Demonstrations exhibit contrast below that of conventional readout by a factor of 3 or more. Prospects are not considered promising.
Laser threshold magnetometry	Probes magnetic field by measuring lasing threshold, which depends on $NV^-$ singlet state population. Moderately improved collection efficiency and contrast are predicted compared to conventional readout. Challenges include non- $NV^-$ absorption and system instability near lasing threshold. Prospects are not considered promising.
Entanglement-assisted magnetometry	Harnesses strong $NV^-$ dipolar interactions to improve readout fidelity beyond the standard quantum limit. Existing proposals require 2D ensembles, impose long overhead times, and exhibit unfavorable coherence time scaling with number of entangled spins. While existing protocols are not considered promising, further investigation toward developing improved protocols is warranted.

## 8. EQUIPMENT CHOICE AND ITS IMPACT ON INSTRUMENT PERFORMANCE

This chapter will present some of the considerations that influence the choice of the equipment needed for NV center sensors measurements. The requirements for lasers used both for initialization of the NV centers and for the accumulated phase shift readout and although requirements for the microwave radiation sources necessary to transfer the quantum system of the NV center to the state of superposition are discussed. The technical methods of creating a bias field, which is necessary for measurements in most of the regimes usually applied are considered. The following subsections describe the optical structures and cameras used both for supplying initiating laser radiation to the surface of a crystal containing the NV centers and for collecting fluorescence from them. Considerations are also given on the configuration of the mount of the diamonds used as sensitive elements in various measuring schemes.

### 8.1 Laser

Due to its availability and performance, the 532 nm solid-state green laser is the most common in quantum magnetometry applications. A limitation for pulsed readout methods can be the low intensity of the green pump laser, typically  $\sim 10 - 1000 \text{ W/cm}^2$ , for a few millimeter illuminated field of view. To transfer the electrons of the NV center from the ground to the excited state ( ${}^3A_2 \rightarrow {}^3E$ ), any laser excitation with wavelengths in the range from 637 to  $\sim 470 \text{ nm}$  can be used due to the wide phonon sideband, which spans hundreds of nanometers. Various types of lasers were used in experiments with NV centers: 532 nm frequency-doubled Nd:YVO<sub>4</sub> and Nd:YAG lasers, helium-neon lasers with a wavelength of 594 nm, lines of argon-ion lasers (457, 476, 488, 496 and 514 nm), LED and diode lasers 520 nm and 637 nm and supercontinuum lasers with an acoustooptic tunable filter. Researches were also carried out to find the characteristics of laser radiation (wavelengths, power) leading to the most favorable ratio of NV<sup>-</sup>/NV<sub>0</sub> charge states and absorption cross section<sup>3</sup> [86]. In order for the sensitivity to a magnetic field to reach the limit of photon shot noise, it is necessary to achieve maximum stability of the laser radiation intensity and of all the optics used, since the main readout signal from NV centers is the fluorescence intensity [32].

By increasing the intensity of the laser radiation, it is possible to achieve both an improvement in the fluorescence intensity of NV centers and in photon shot noise, as well as in the shape of the ODMR line. In magnetometry experiments, the polarization of the laser should favor the selection rules for optical absorption for the chosen orientation of the NV center. The  ${}^3A_2 \rightarrow {}^3E$  transition is dipole-allowed when the radiation is polarized in a plane perpendicular to the axis of the NV center. If it is necessary to interrogate all orientations of NV centers, such a laser polarization is chosen that addresses all the NV orientations with comparable strength. When choosing the laser power, it is necessary to take into account the fact that the photon shot noise limit increases as the square root of the laser power, while the heating of the sensitive diamond and of the measured sample is proportional to the laser power. Therefore, to avoid being limited by the quantization noise, the analog-to-digital conversion characteristics (bit depth) should also improve as the fractional photon shot noise improves. [32].

The power of laser radiation affects various magnetometry protocols in the following way [32]:

1. Changing the laser intensity changes the width and shape of the resonance lines in CW-ODMR measurements.

---

<sup>3</sup> The absorption cross section is the ability of a particle to absorb a photon of a particular wavelength and polarization.



2. In pulsed experiments, in order to avoid the need to increase the initialization and readout times of optical spin states and, as a consequence, the deterioration of the temporal resolution of the experiment, the laser intensity should ideally be close to the optical saturation.

## 8.2 Microwave source

The principal features for characterization of microwave control include microwave bandwidth and feed efficiency, as well as control area and homogeneity within it [68].

Antennas used in NV center magnetometry must produce MW radiation that satisfies the selection rules for the transitions between  $^3A_2$  sublevels, which require right- or left-circularly polarized microwave radiation. As possible options for MW antennas, a loop or a pair of crossed MW stripline resonators can be used, which are exited in phase or in  $90^\circ$  out of phase to achieve the circular or linearly polarized microwave field required by the measurement protocol [32].

The basic design of MW antenna (the pieces of one or two straight wires) is shown in Figure 25 a, b. The advantage of this method is its simplicity, while the obvious disadvantage is the low level of homogeneity of the generated radiation. Other commonly used design – the loop antenna is presented in Figure 25 c. It can greatly improve the microwave uniform area, but has a limited frequency bandwidth, which is its intrinsic drawback [68].

Also, for measurement applications based on NV sensors, special devices such as the inset-fed rectangle microstrip patch antenna, the tunable loop gap resonator, and the strip antenna coplanar waveguide resonator have been developed (Figure 25 d, f). For the case when, in the absence of an external magnetic field, the energy levels  $m_S=+1$  and  $m_S=-1$  are degenerate and a linearly polarized microwave control field cannot resolve them, antennas with circular polarization were proposed (Figure 25 g). In cases where the crystal contains NV centers orientated in all possible directions, it is necessary to specially plan the experiment, since without this, even circularly polarized antennas cannot be directly used for measurements. Antennas specially designed and adapted to specific experimental conditions, for example, allowing to achieve greater uniformity along the z axis of the NV center or MW antennas in the 60–90 GHz range, are also presented in the studies. The goal of many proposed alternative design solutions for microwave antennas is to increase their efficiency, optimize the uniformity of the generated field and bandwidth [87], [88], [89], [90], [91], [92], [93]. The technical data of the various antennas developed are summarized in Table 10 [68].

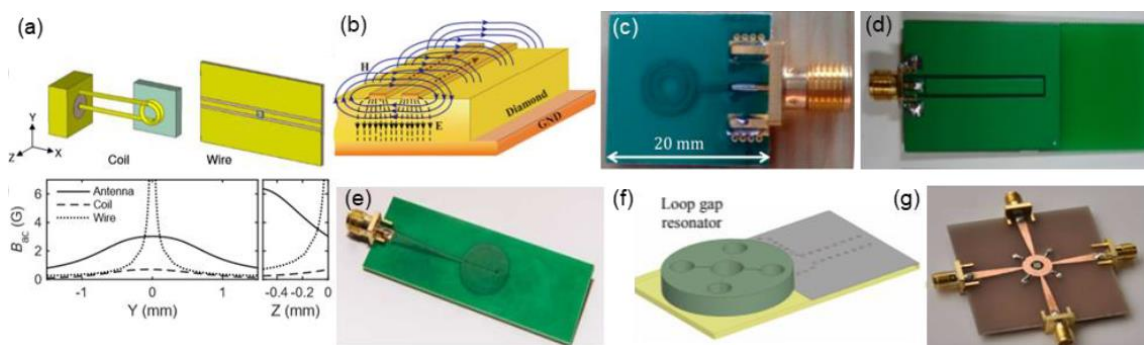


Figure 25. Microwave sources

(a) Single wire scheme and coil scheme. (b) Two-wire scheme. (c) Double loop antenna. (d) Coplanar waveguide resonator. (e) Planar ring antenna. (f) S-band tunable loop gap resonator. (g) Circular polarization antenna Source: [68].

To obtain optimal measurement sensitivity, a compromise must be made between the power of the microwave radiation and the power of the laser. Since an increase in the



MW power improves the CW ODMR contrast but increases the width of the resonance lines, and a high optical pump power leads to a weak contrast (because the laser quickly pumps parts of the NV center populations that were removed by the MW drive), but it improves the shape of the resonance lines. Sensitivity is also influenced by the microwave intensity noise, which, similarly to fluorescence intensity noise, affects the contrast and the linewidth of the ODMR spectrum [32].

**Table 10** Summary of microwave antenna parameters. Source: [68].

Scheme	Generated magnetic field strength	XY uniform area	Z uniform length	Bandwidth	S11	Q
Multiple wires						
Double loop antenna	5.6 G @ 0.5 W	$0.95 \times 1.2 \text{ mm}^2$	-	40 MHz	-25 dB	70-120
inset-fed rectangle microstrip patch antenna	0.8 G @ 1 W	$1 \times 1 \text{ mm}^2$	0.5 mm?	60 MHz	-20 dB	-
coplanar waveguide resonator	3.7 G @ ?	$>2 \times 2 \text{ mm}^2$		Small	-	-
large-area microwave antenna	3 G @ 1 W	$1 \text{ mm}^2$	$>0.4 \text{ m}$	400 MHz		7
coplanar waveguides	6-10 G @ 1 W	small		15.8 GHz	~ -20 dB	
dielectric resonator antenna	2.8 G @ 5.2 W	Diameter 2.4 mm	1.7 mm	~ 50 MHz	0.1	

Also critical in CW ODMR measurements is the sweeping speed of the microwave frequency. When the MW driving frequency is swept along the resonance curve, the NV center needs sufficient time to re-balance according to the changed conditions after the probe frequency is updated. The response rate of the NV center, which is usually controlled by the optical pumping rate, must exceed the MW modulation rate also in lock-in detection experiments to combat fluorescence intensity noise. [32].

The characteristics of the microwave field affect the performance of various applied magnetometry techniques in different ways, which must be taken into account when setting its operating modes [32]:

1. When working with the CW ODMR method, increasing the MW driving power improves the contrast but broadens the spectral line.
2. When working with pulsed methods – Ramsey sequences, Hahn echo and other dynamical decoupling sequences, pulse errors and spatial inhomogeneity of MW can reduce contrast and degrade sensitivity.

### 8.3 Static magnetic field

Both permanent magnets and electromagnets can be used to create the bias field required for most magnetometry experiments. Whereas permanent electromagnets allow for higher  $B_0$  values in a more compact device, electromagnets allow the bias field to be arbitrarily adjusted over a range of up to a few teslas. The disadvantages of using permanent magnets include the need to take into account the temperature drift of the  $B_0$  value created by them, while electromagnets can contribute to the heating of the sample and the system, they require a stable current source and sometimes water cooling. Electromagnets can be designed in the form of a set of Helmholtz coils, C-frame/H-frame electromagnets or solenoids [32].

The bias field is chosen in accordance with the needs of a particular experiment and the characteristics of the samples being measured. Thus, for thermometry experiments or for electric field measuring, the bias field is not required and  $B_0=0$  is chosen (Figure 4 B). When studying magnetically soft samples, it is necessary to set the minimum bias field, since their magnetization can change under the action of an applied magnetic field. Another advantage of a small bias field is that it usually has a small gradient across the field of view. To study, for example, paramagnetic minerals, a large bias field can be useful. This is due to the properties of paramagnetic particles whose magnetization



scales with  $B_0$  until saturation. The fluorescence contrast of NV centers can be improved by choosing  $B_0 \sim 30\text{--}50$  mT due to the polarization of nitrogen nuclei. The choice of the bias field value so that the AC sample frequency matches the spin transition frequency of the NV center is recommended for  $T_1$  relaxometry and Rabi imaging [32].

The direction of the bias field also plays a very important role for various magnetometry applications. To optimize measurement parameters such as optical polarization, fluorescence, and contrast from the preferred orientation of the NV center, it is necessary to align  $B_0$  along the axis of the NV center (crystallographic direction [111]), which will allow readout from NV centers orientated along this axis, ignoring the rest orientations (Figure 4 C). In order to obtain complete information about the vector magnetic field by reconstructing it from eight resonant frequencies, the magnitude and direction of the bias magnetic field is adjusted so that the spectra and resonant frequencies from the different NV center orientations do not overlap (Figure 4 D). Alignment of the bias field in accordance with the crystallographic direction [110] or [100] leads to the degeneration of resonant frequencies from different orientations of NV centers and, as a consequence, to an improvement in contrast. If with a diamond cut along [100] the bias field is aligned along the [100] direction, the resulting resonant shift will be three times less than in the case of the bias field aligned along the [111] orientation, and the direction of the magnetic field projection will be perpendicular to the chip (Figure 4 E). If the configuration of a particular experiment or the features of the sample under study do not allow proper orientation of the bias field, the overlap of the resulting spectral lines can make it difficult to extract information about the vector magnetic field. Then, the selection rules of the  ${}^3A_2 \rightarrow {}^3E$  optical transition can help evaluate the contribution of fluorescence from each orientation of the NV center [32].

The main requirement for the bias field is its homogeneity. In case of ununiform field, the following problems arise [32]:

1. Deterioration of contrast and sensitivity in pulse experiments due to the space-dependent pulse errors.
2. Broadening the width of the resonance line in each pixel in a wide-field, two-dimensional magnetic field imaging schemes.
3. To determine the measured magnetic field, the bias field must be subtracted from the result obtained, and its inhomogeneity will complicate this task.

#### 8.4 Optics for illumination and fluorescence collection

The conditions of magnetometry experiments impose different requirements on the methods of NV sensors illuminating with a pump laser. For example, for quantum diamond microscopy (QDM), side illumination using an objective with a long working distance, low magnification and large field of view is a good method. This way the beam will illuminate a large enough area without clipping the lens. Also, in the case of microscopes with high magnification, it is possible to control the polarization of the laser and obtain parallel beams emerging from the objective by focusing the pump laser on the back aperture of the objective, which, however, threatens with burns. To avoid excessive exposure of the sample, as well as the sensor, it is possible to apply illumination via total internal reflection in the diamond, reduce the optical intensity by covering the surface of the diamond with a reflective layer, or use cylindrical lenses to form a laser beam into a light sheet [32].

A confocal light path and an objective can be used to collect fluorescence from NV centers. But, due to the high refractive index of diamond (2.4), the total reflection angle is small ( $24.6^\circ$ ), and the collected fluorescence may be significantly insufficient (Figure 27 a). To solve this problem and improve the efficiency of fluorescence collection, various methods have been proposed, which can be roughly divided into two categories [68]:

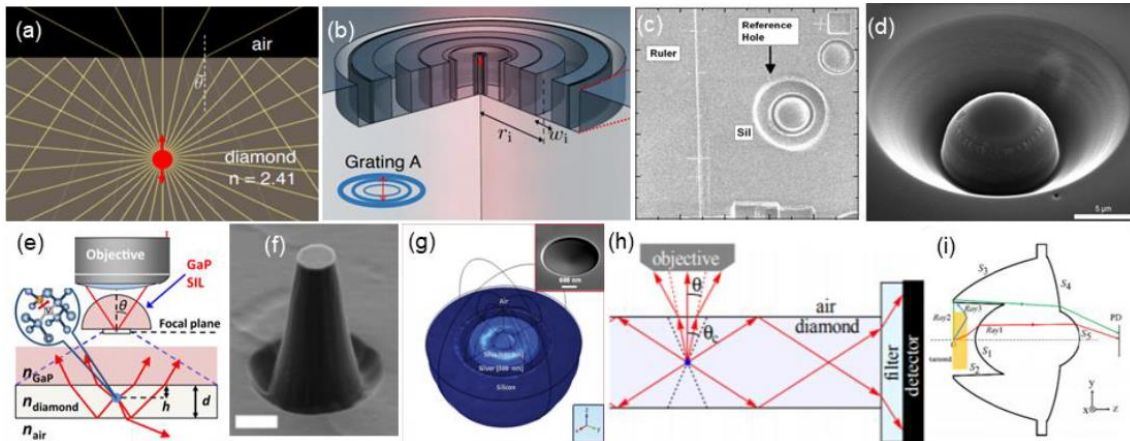


Figure 27. Optics for illumination and fluorescence collection

(a) Schematic diagram of the total reflection. (b) Chirped circular dielectric gratings. (c-e) Different solid lens SIL schemes. (f) Optical waveguide schemes. (g) Optical waveguide with a nanodiamond in the middle. (h) Side collection scheme. (i) TIR lens scheme. Source: [68].

1. Collection of fluorescence from a single diamond within a volume from  $\text{nm}^3$  to  $\mu\text{m}^3$ . To increase the efficiency of fluorescence extraction, the surface surrounding the diamond is specially treated and modified by providing it with the solid immersion lens (SIL), a dielectric antenna, an optical waveguide or a chirped circular dielectric gratings (Figure 27 b). Other researchers have proposed to apply for this purpose all-dielectric nanoantennas, circular bullseye gratings, plasmonic gratings and cavities, as well as to place a diamond directly into an optical waveguide using an objective lens for PL collection (Figure 27 g).
2. Methods for collecting fluorescence from an ensemble of NV centers. One method involves the use of a compound parabolic concentrator CPC, which allows a one-sided fluorescence collection, but frontal fluorescence cannot be collected efficiently (Figure 27 h). Collection of fluorescence from five faces can be achieved using the scheme with total internal reflection lens (TIR) (Figure 27 i). To reduce the effect of the high refractive index of diamond, an anti-reflective coating is applied.

When performing QDM imaging, the best photon collection efficiency can be achieved by the maximum available numerical aperture (NA) of the microscope objective. Objectives with a large numerical aperture are also typically characterized by high magnification and short working distance, which can be even less than the thickness of a diamond. Image quality can be degraded by optical aberrations during fluorescence imaging through a diamond chip. In addition, it is important to reduce the chromatic aberrations of the microscope as it displays broadband NV fluorescence ( $\sim 637\text{--}800\text{ nm}$ ). In pulse magnetometry experiments, it is necessary to take into account the characteristics of the acousto-optic modulator (AOM) used as an optical switch, the main of which are the rise time, extinction ratio and efficiency [32].

## 8.5 Camera

In order to ensure the quality of the NV-imaging and to achieve high sensitivity to the magnetic field, the imaging system must collect a large number of photons, for which it is necessary to optimize the performance of all elements responsible for the passage of the optical signal – the delivery of the excitation light, the collection of the resulting fluorescence, the throughput of the imaging optics and, at the last stage – the operation of the sensor (camera), its capacity of registering most of the incoming photons. The main parameters that limit camera performance are quantum efficiency (QE) – the ratio of the number of charge carriers collected to the number of photons reaching the sensor



surface, fill factor (FF) – the size of the photo-active area within a pixel (Figure 28 a) and the full well capacity (FWC) – the finite amount of charge that can be stored in a pixel without signal degradation. The last parameter is of decisive importance, it determines the maximum achievable signal-to-noise ratio (SNR), limited by shot noise. The corresponding dependence is shown in Figure 28 b. Typical camera sensors have FWC in the range ( $10^4 - 10^5$ ) implying  $SNR \leq 300$ . If a sufficiently large number of fluorescence photons enter the camera during one exposure, it is desirable to choose sensors with the maximum FWC to provide the most sensitive ODMR magnetometry [94].

The parameters of cameras with different types of sensors that determine the sensitivity of wide-field magnetic imaging are summarized in Table 11 [94].

**Table 11.** Camera sensor parameters used for determination of achievable SNR and magnetic field sensitivity. Source: [94]

Camera #	Sensor type	Pixel size ( $\mu\text{m}$ )	Array size (pixels)	QE (%)	FPS with full resolution	FWC ( $e^-$ )	ADC (bits)
1	CMOS	$5.3 \times 5.3$	$1280 \times 1024$	$\sim 60$	60	$8 \times 10^3$	10
2	CMOS	$4.8 \times 4.8$	$1280 \times 1024$	30-55	224	$1 \times 10^4$	10
3	EM-CCD	$16 \times 16$	$512 \times 512$	$> 90$	56	$1.8 \times 10^5$	16
4	CMOS	$128 \times 128$	$128 \times 128$	$\sim 50$	10 000	$1 \times 10^8$	14
5	Lock-in	$39.6 \times 39.6$	$280 \times 292$	60-80	$3\ 800^a$	$3.5 \times 10^5$	$2 \times 10^b$

FPS – the maximum number of frames that a camera is able to capture per second

ADC – the digital resolution of the analog-to-digital converter

a Internally up to 1 000 000 FPS (modulation frequency  $\leq 250$  kHz).

b Separate in-phase and quadrature output images.

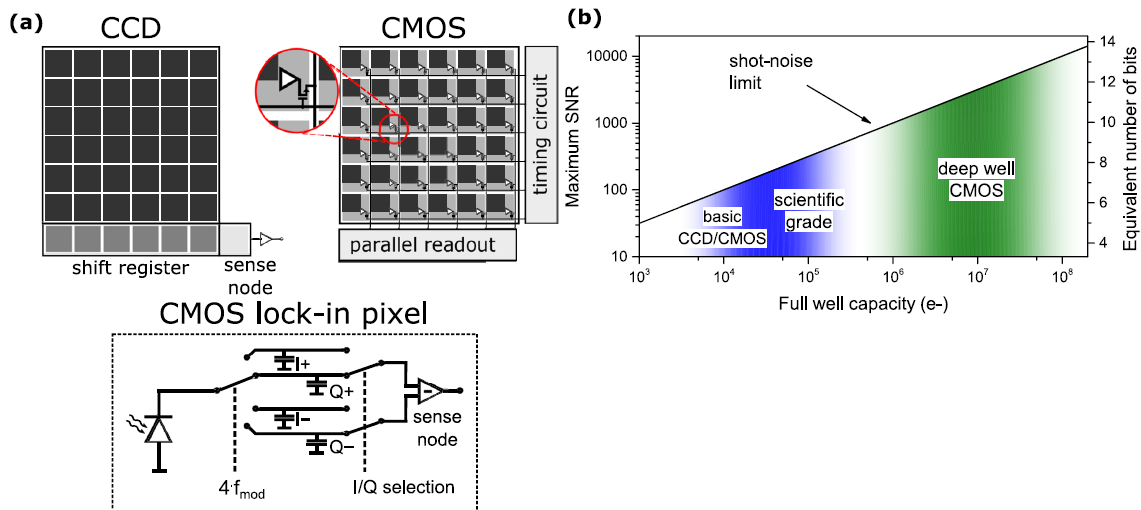


Figure 28. Camera sensor operation

(a) Illustrative diagram of camera sensor operation. Photo-active area is shaded black. For a CCD matrix, the collected charge is transferred downwards line-by-line to the shift register and then consecutively converted to a voltage and digitized. CMOS sensors use in-pixel transistors for charge conversion, which enables high-speed, random-access readout at the cost of a limited photo-active surface. Lock-in sensor uses four charge-storage capacitors to encode the signal phase, each for a quarter period of modulation frequency. (b) Maximum achievable SNR as a function of a pixel FWC. Left shaded area covers most common camera sensors. Right axis indicates the minimum ADC resolution needed to resolve pixel value without compromising SNR. Source: [94].

Thus, the characteristics of cameras that are important for applications in magnetometry and should be taken into account are [32]:

- the expected rate of photon collection from the layer of NV centers;



- quantum efficiency;
- pixel size;
- camera readout noise;
- dark current noise;
- well depth;
- frame frequency;
- data transfer rate;
- global/rolling shutter capabilities;
- software and external triggering.

For experiments that require a high photon count rate, when it is necessary for the camera to process a large number of photoelectrons per second without saturating, the main factors will be quantum efficiency, number of pixels, the pixel well depth and frame rate. [32].

The experimentally achievable temporal resolution is limited by the camera frame rate. For pulsed experiments, the camera frame rate is especially important, since the possible repetition rate of the experiment and the sensitivity depend on it. This parameter can be increased using only part of the sensor. However, to maximize the number of photoelectrons per second, it is preferable to use the full camera sensor so as not to reduce the product of the frame rate and the number of pixels. If the photon count rate is low, then the quantum efficiency should be maximized, and the readout and dark current noises reduced [32].

The microscope magnification for the desired field of view is determined by the camera sensor size. If the camera pixels are too far apart for the microscope magnification, the pixel size should be chosen so as not to degrade the spatial resolution determined by the optical diffraction, for this reason the diffraction-limited spatial resolution should be oversampled by at least twice. If the camera sensor area exceeds the effective image area, the resulting image may contain vignetting – darkened corners [32].

The minimum camera exposure time and maximum camera frame rate for pulsed experiments should be balanced with the optical readout time  $t_R$  based on the following considerations [32]:

1. If the frame rate of the camera is too low to acquire a new frame at the rate required to complete each experiment and determined by the measurement time, the sensitivity of the pulsed experiment is lost.
2. If the minimum exposure time exceeds the readout time  $t_R$ , the readout laser must be turned off for a period determined by the difference between these times.

## 8.6 Diamond mounting and configuration

There are two approaches to fixing the diamond sensor and the sample being measured in, for example, magnetometry applications such as quantum diamond microscopy [32]:

1. Fixing a diamond sensor in a microscope so that the measured sample is independently moved and manipulated using special kinematic stages. The advantage of this approach is the ability to keep the position of the sensitive chip constant relative to the entire optics, as well as relative to the magnetic bias and WM fields. This reduces the setup time for new measurements, facilitates the change of samples, and ensures better reproducibility of experiments.
2. Attaching the diamond sensor directly to the sample and moving the diamond and the sample together in the field of view of the microscope. This method of fixation provides a more reliable minimum separation of the sample and the sensitive element.

With an upright microscope setup, the sample mounting and manipulation is generally easier than with an inverted microscope [32].



## 8.7 General design considerations

Equipment parameters and characteristics that optimize sensor performance for various measurement techniques are summarized in Table 12 [32].

**Table 12:** General hardware considerations that apply to all measurement techniques. Source: [32]

Design choice	Considerations
Diamond	<ul style="list-style-type: none"> <li>– NV density affects the sensitivity</li> <li>– Inhomogeneity in strain, density, and magnetic environment spoils the sensitivity</li> <li>– Match the NV layer thickness and sample thickness</li> </ul>
Laser	<ul style="list-style-type: none"> <li>– Field of view sets laser intensity</li> <li>– Laser intensity noise can limit sensitivity</li> <li>– Laser polarization addresses different NV orientations</li> <li>– Homogeneous illumination is desirable</li> </ul>
Microwaves	<ul style="list-style-type: none"> <li>– Amplitude and phase instability affect sensitivity</li> <li>– Amplitude homogeneity is desirable</li> </ul>
$B_0$ field	<ul style="list-style-type: none"> <li>– A <math>B_0</math> gradient can cause varying sensitivity uniformity</li> </ul>
Optics	<ul style="list-style-type: none"> <li>– Microscope objective sets the collection efficiency and optical diffraction limit</li> <li>– Microscope components set the magnification and field of view size</li> </ul>
Camera	<ul style="list-style-type: none"> <li>– Pixel size should oversample other resolution limitations (e.g., optical diffraction)</li> <li>– Frame rate <math>\times</math> well depth <math>\times</math> number of pixels set the best possible sensitivity</li> <li>– Transfer rate and buffer size can throttle the maximum experiment rate</li> <li>– Camera efficiency is worse than photodiode efficiency</li> </ul>
Diamond mount	<ul style="list-style-type: none"> <li>– Aim for high thermal and mechanical stability during an experiment</li> </ul>
Magnetic environment	<ul style="list-style-type: none"> <li>– Mitigate background field (e.g., Earth's field, electronics, etc.)</li> </ul>

## 9. NAVIGATION WITHOUT EXTERNAL REFERENCES

Two approaches can be distinguished on which GPS-independent navigation systems are built:

- The first option – inertial navigation systems (INS) – navigation device that uses motion sensors (accelerometers), rotation sensors (gyroscopes) and a computer to continuously calculate by the position, the orientation, and the velocity (direction and speed of movement) of a moving object without the need for external references. A basic inertial navigation system can also be upgraded with magnetic sensors which provides a heading reference similar to a magnetic compass.
- The second option – map-based navigation using magnetic field measurements – navigation system, which uses magnetometers to allows analyse small anomalies in Earth's magnetic field, then overlay that data with known maps of Earth's magnetic field and determine the position.

It is also possible to combine these methods or build hybrid navigation systems that use (when possible) the GPS signal to more accurately determine coordinates and eliminate accumulated errors.

A vector magnetometer that measures the magnetic field vector in a given direction is also commonly used to reduce INS drift. Therefore, in addition to orthogonal gyroscopes and accelerometers, INS measuring units often contain three orthogonal magnetometers, which, by measuring the strength and direction of the local magnetic field, allow determining the north direction [95].

Magnetometers are affected by local perturbations of the Earth's magnetic field, induced by nearby magnetic objects, and are not accurate enough to completely replace gyroscopes in inertial systems, but if the so-called sensor fusion is applied - a combination of their data with gyroscopes data, the accuracy of the calculated orientation can be significantly improved. With this approach, the navigation system continues to be autonomous from any external infrastructure. Although it only allows to reduce the rate of accumulation of errors and does not lead to absolute positioning accuracy. According to [95] the application of sensor fusion, allowed to reduce the error accumulated over 60 s from over 150 m to around 5 m.

### 9.1 Inertial navigation systems

Inertial navigation systems (INS) use a combination of sensors such as accelerometers and gyroscopes (angular velocity sensors) to determine the coordinates of an object and its movement characteristics – height, orientation, position and velocity. They may also be able to measure other environmental parameters such as temperature or magnetic fields [96].

Figure 29 shows a block structure of an inertial navigation system. It consists of an inertial measurement unit (IMU), a navigation computer that processes the information received from the sensors and instrumental support electronics. IMUs typically contain three orthogonal accelerometers that measure the linear acceleration of an object and three orthogonal gyroscopes that measure its angular velocity. To navigate with respect to the inertial reference frame, the direction in which the accelerometers point is constantly monitored.

However, the currently existing INS continue to need further development. In many of their characteristics, such as weight, size, power requirements and heat dissipation, they are still inferior to GPS receivers. Also, an important problem, the solution of which is





constantly being improved by both instrumental and software ways, is the accumulation of navigation errors over time.

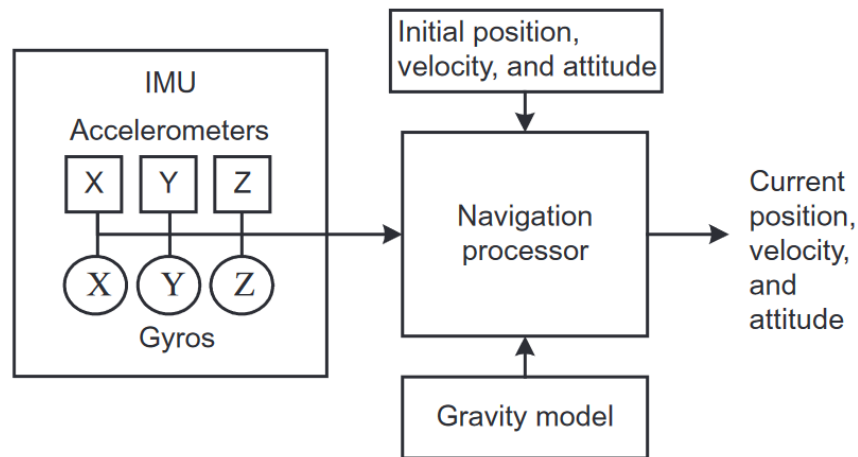


Figure 29. Basic schematic of an inertial navigation system. Source: [97].

Inertial navigation systems are divided into two main types [96]:

1. Gimbaled or stabilized system. In it, inertial sensors are fixed on a stable platform, which is mechanically isolated from the rotational movement of the vehicle. Such systems are recommended to be installed on submarines, ships and other objects that require very accurate navigation data.
2. Strapdown systems. In this type of system, the sensors are rigidly attached to the vehicle body, making the whole structure simpler and more reliable. Such systems are cheaper, have less weight and size than gimbaled systems, but the processing complexity in the analysis of their sensor data increases significantly.

Extremely accurate inertial sensors are required to provide sufficient accuracy for the purposes of unaided inertial navigation (dead-reckoning) in estimating the position and velocity of an object. The unbounded error growth in the navigation algorithm is a result of the various errors in the measurements of the inertial sensors themselves such as noise, bias, misalignments, gyroscopic g-sensitivity<sup>4</sup>, scale factor errors and temperature dependencies. Typically, position errors when performing pure inertial sensor integration are dominated by gyroscope performance.

Since the accelerometer measures the total acceleration, to obtain the linear acceleration of the system due to motion, from the accelerometer measurements must be subtracted the pseudo-acceleration due to gravity using data on the system's attitude. The ability of the INS to accurately estimate the system's attitude is extremely important for determining the linear acceleration and, therefore, also the velocity and position of the system. To obtain data on the velocity of the system, the resulting linear acceleration measurement must be integrated, and to obtain the position of the system, the linear acceleration must be integrated twice.

Currently, inertial navigation systems mainly use optical and electromechanical devices as sensors. However, the development of quantum technologies, which has been observed in recent years, promises the broad prospects for their application, including as inertial sensors. It can be expected that due to these new advanced technologies, a new type of inertial navigation systems based on quantum sensors will appear in the foreseeable future [98].

Inertial measurements, which are based on the data on the energy state of electron or nuclear spins in a solid crystal lattice, are mainly at the experimental stage. The

<sup>4</sup> Acceleration sensitivity when gyroscope experiences the bias shift at a constant linear acceleration.



development of innovative technologies for creating sensors for measuring acceleration and angular velocity based on this principle, in particular using NV centers in diamond, although at an early stage and still facing huge problems, is currently developing rapidly. These technologies have both applied value in terms of the possibility of their application in new inertial devices, and a great theoretical and research value [99].

## 9.2 Map-based navigation using magnetic field measurements

Another alternative to GPS navigation, although less accurate, could be navigation using Earth's magnetic field data. The idea of this method is to extract data about the location of the object using magnetometry measurements of the surrounding field and accurate maps of anomalies and variations in the Earth's magnetic field, applying machine learning (ML). Despite the possible influence of noise, as well as numerous local and wide-range distortions, it is assumed that such a method may be practical [100].

The attractiveness of this method, despite the problems mentioned above, is primarily due to the fact that the magnetic field, being worldwide and all-penetrating, is always available for measurements. It, especially when acting at a distance, is almost impossible to deliberately distort or suppress. Alternative similar methods of navigation, timing solutions, and positioning can use terrain tracking, cameras and computer vision, or star navigation, but all these methods are limited by the visual environment, inaccessibility of the topography over the water and subjected to weather. Data on the magnetic field can always be measured by high-precision magnetometers and compared with the detailed maps of magnetic anomalies available to determine the position of the object.[100].

The use of much more accurate (on the order of one meter) mobile GPS navigation is not always available, and, meanwhile, there are tasks for which high accuracy, compared to availability, plays a secondary role. The method of magnetic navigation at this stage can be characterized by an accuracy of up to one kilometer, and researches are carried out to improve it.

As a sensor for magnetic fields differences measuring, magnetic anomaly navigation uses a scalar magnetometer, the measurement data of which is compared with the magnetic field maps, that allow to extract the information necessary to obtain the location of the object. There are many maps of the Earth's magnetic field, compiled with varying accuracy and quality based on geophysical researches, mainly for the purpose of studying the subsurface of the Earth and obtaining the information about mineral deposits or discovering resources such as oil or diamonds. The performance of magnetic navigation mainly depends on the accuracy of the maps used [101].

While the compass work is based on the magnetic field created by the Earth's core to cause its needle to point North, the field generated by the core is not suitable for absolute positioning applications, as it has very little spatial variations.

An ideal candidate for magnetic field map-based navigation is the crustal field, which is 1-5% of the total measured field near the Earth's surface and amounts to several hundred nano-Teslas. This field is almost static and allows to extract information about it with high spatial frequency [101].

The use of the magnetic field of the earth's crust for air navigation is especially promising, since, on the one hand, at the appropriate heights, artificial sources of the magnetic field distort measurements to a much lesser extent than it would be for objects located on the Earth's surface, and on the other hand, the field retains its high spatial-frequency composition, which is being lost at satellite heights. The use of absolute positioning according to the Earth's magnetic field is widely used for satellites, but it allows achieving an accuracy of the order of tens of kilometers, which would not be suitable for aviation. This is because the height increase actually acts as a low spatial-frequency filter for the Earth's magnetic field [101].

### 9.3 Dark Ice quantum magnetometer of Lockheed Martin

Lockheed Martin engineers Mike Di Mario and his team are developing a technology to measure and analyze small anomalies in the Earth's magnetic field using a quantum sensor based on NV centers in diamond to determine the position of an object without the need to send signals to satellites such as GPS. The advantage of an NV center-based sensor is the ability to measure a three-dimensional vector of the magnetic signal, unlike a compass which only gives a two-dimensional signal. Such a system cannot be hacked or jammed, it is completely passive, does not transmit anything and works in any weather at any point on the surface.

Developed by Lockheed Martin for magnetic anomaly navigation purposes, quantum magnetometer prototype received a name "Dark Ice". It uses synthetic diamond with NV center to measure the direction and strength of almost imperceptible magnetic field anomalies (Figure 30). The technology involves overlaying these magnetometry data on known maps of the Earth's magnetic field to localize the object. The data used to produce precise location information was supplied by the US National Oceanic and Atmospheric Association.

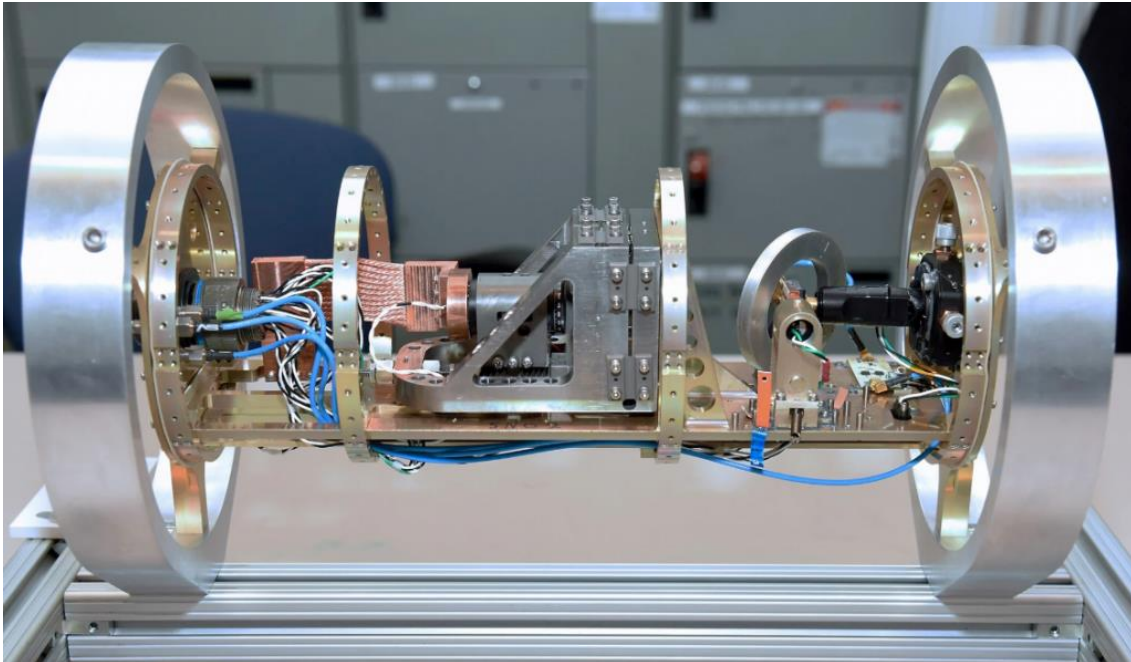


Figure 30. The "Dark Ice" quantum magnetometer. Source: [102].

Due to the fact that most of the currently used magnetic sensors installed on modern ships or aircraft are capable of measuring only the magnetic field strength and not the direction of its vector, they, as a rule, do not use magnetic anomalies for navigation. The real advantage offered by the new quantum technology is that in addition to having a very large bandwidth and dynamic range, it has an ability to produce a true magnetic field vector.

Dark Ice, due to its compactness and high sensitivity, can be reliably used both for military aviation and for search and rescue operations, or the detection of hard-to-reach watercraft.

Lockheed Martin researchers estimate that the mass production and application of this technology may take another three years due to a number of complex engineering and technical problems that have not yet been solved, mainly related to calibration.



Lockheed Martin has registered 21 patents in connection with this project [103]. Significant resources were invested in the development of the magnetometer prototype. The research results obtained were published in [31], [104].

Since the magnetometer is supposed for military use, one problem that is still being worked on is the need to filter out the magnetic field created by all the metal present on a battleship or aircraft carrier. Representatives of the oil and gas industry also see the potential of this technology for underwater exploration.

The industrialization of diamond production for quantum technologies is also still a challenge. Lockheed Martin is partnering with one of the leaders in the production of artificial diamonds, the European company Element Six (De Beers Group). Diamonds for the Dark Ice project are produced by chemical vapor deposition (CVD) method, followed by nitrogen ion irradiation and annealing. Although the description of the developed technology and the obtained results of its application, published in [104], testify to its success, the problem of quality control of each specific manufactured diamond sample during their production on an industrial scale is still not completely solved.

Since the navigation accuracy of the proposed technology, which is expected to reach 200 meters, will still be inferior to GPS-positioning, it may be used, on commercial ships or aircraft, mainly as a backup in conditions of GPS unavailability or as an addition to inertial navigation systems, helping to reduce the errors accumulated in them over time [105], [106].



## 10. ROTATION MEASUREMENT USING NV-CENTER SENSORS

Quantum technologies, as they develop, will play an increasingly important role compared to classical systems in rotation measurement applications where high-precision measurements are required. Potentially, devices based on NV centers, due to their small size, good coherence, and robust solid-state design, can compete with other sensors.

The principle of operation of a solid-state spin inertial sensor based on an NV center is to measure the phase difference, which accumulates over time, between an exciting microwave field and a rotating two-level system of electron spins. The measurement of the thus accumulated quantum geometric phase provides information on the rotation of the carrier. Such a quantum device can compete with conventional gyroscopes in many of its parameters and characteristics, such as sensitivity, size and cost [99].

### 10.1 Development of spin-based rotation measurement

Research to use quantum sensing based on NV centers for inertial measurements has been underway over the past few years. Thus, the methods for measuring a phase shift arising directly from the physical rotation using a single NV center spin were described in [61], [107], [108], [109]. Also, in [110] and [111] were described gyroscopes based on NV centers with sensitivity up to  $5 \times 10^{-3} \text{ rads}^{-1} \text{ Hz}^{-1/2}$ . The effect of rotation-induced pseudo-fields on the sample spins was studied in [107], [109]. In these experiments, a rapidly rotating diamond mounted on a rotor containing either a single NV center or an ensemble of them was used. An integrated rotation scheme using the nuclear spin of the  $^{14}\text{N}$  atom, which is the part of the NV center, whose operation is based on the double quantum pulse protocol, was proposed in [112]. It was characterized by a rotation sensitivity of  $4.7^\circ \text{ s}^{-1/2}$  and a zero-bias stability of  $0.4^\circ/\text{s}$  [99].

The development of quantum gyroscopes, potentially close to possible practical applications and promoting ever greater miniaturization and integration possibilities, is stimulated by ongoing scientific experiments in this area. The design of a quantum NV center gyroscope, which uses a bilateral layout design of coils to ensure uniform distribution of MW and RF fields, is described in [113]. A similar system that applies the nucleus of the  $^{13}\text{C}$  isotope to measure the rotation using the NV center is presented in [114]. Another experiment [115] measured the dynamic phase difference caused by the macroscopic rotation of diamond using the  $^{14}\text{N}$  nuclear spins of an ensemble of NV centers under sub-Hz rotation. This experiment applied a double quantum protocol based on the Ramsey sequence and its results were further confirmed by a commercially available MEMS gyroscope [99].

### 10.2 Sensing mechanism of spin-based rotation measurement

Figure 31 schematically depicts the principle of rotation measurement based on NV centers. The external field in a non-rotating frame determines the precession frequency  $\omega_0$ , which changes as the angular velocity of rotation changes. By measuring the  $\omega_0$ , the information can be obtained about the rotation by calculating it from the  $\omega_0$  and the known external magnetic field [99]:

$$\omega_0 = \omega_L \pm \Omega. \quad (\text{Eq. 10.1})$$

Here  $\omega_L$  – is the frequency of the Larmor precession depending on the applied magnetic field ( $\omega_L = \gamma B$ ),  $\gamma$  – the gyromagnetic ratio and  $\Omega$  – is the required angular velocity of rotation [116].

The precession frequency  $\omega_0$  is determined by measuring the energy difference between the resonant spectral lines of the NV center, which are shifted under the action of an applied magnetic field, and in the case of rotation, experience an additional shift

proportional to the rotation frequency. To ensure greater sensitivity, as a rule, the shift of hyperfine states formed under the influence of the nuclear spins are used. The method for determining the angular velocity of rotation will be discussed in more detail in Section 10.5 using the example of the nuclear spin gyroscope prototype proposed in [112].

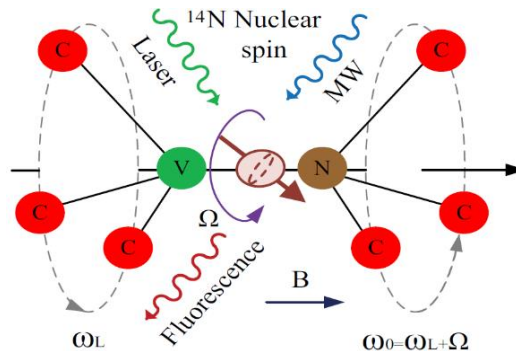


Figure 31. Mechanism diagram of NV-based rotation measurement.

In a non-rotating state, the spin magnetic moment precesses in the direction of the external magnetic field, and the precession frequency is proportional to the applied magnetic field (black arrow). In a rotating state, the precession frequency increases by a term proportional to the rotational angular velocity. The 532 nm laser is used for spin polarization, the microwave source is used for spin manipulation, and the detected fluorescence contains rotation information. Source: [99].

Despite the good optical and spin properties of the NV center, it is characterised by the limited coherence time, the dependence of the readout efficiency on the photonic structure and operating temperature (especially in the case of NV ensembles). A promising methodology is to use the neighboring nuclear spin of the  $^{14}\text{N}$  atom as a sensor, which has longer relaxation time and ability to polarization, control and readout with high fidelity enhanced by the quantum non-demolition detection (a measuring protocol that allows a nuclear spin to be readout without demolish its state, and thus enables its redetection to improve readout fidelity) [59].

In addition to possible practical applications, such as the creation of quantum gyroscopes for inertial navigation systems, research based on the measurement of rotation using NV centers is important for the development of quantum informatics, as well as for fundamental science, allowing a better understanding of many quantum-mechanical effects. In particular, experiments are being carried out to increase the sensitivity of mechanical measurements, when diamonds containing NV centers are captured in a liquid or in a vacuum to readout the spin, which can be considered as attempts to couple spins with the macroscopic motion of the particles. With the help of an NV center, a large quantum superposition of a nanomechanical resonator can be achieved [117], [118]. The rotation of a crystal whose natural quantization axis is given by the orientation of the NV center can effectively induce the qubit rotation [108]. In [119], a technique is presented that adiabatically measures the angular velocity using the coupling introduced by the Hamiltonian of the NV center spin system and the quantum geometric phase in the Bloch space (Figure 32). The Hamiltonian of the system evolves cyclically and depends on the magnetic field. The geometric phase, induced by the rotation of the NV center is accumulated non-linearly depending on the angle between the axis of the rotation, the axis of the NV center, and the direction of the MW field. The spin echo scheme is used to readout the resulting geometric phase [99].

Experiments to measure the geometric phase, which is accumulated by the electron spin, are carried out using both the Ramsey method and the spin echo method [61]. In [107], [108], [109], a special setup with a rotor, shown in Figure 33, was used to rotate the NV center in a magnetic field. In [115], nitrogen nuclear spins of the NV ensemble were used to measure the platform rotation speed [99].

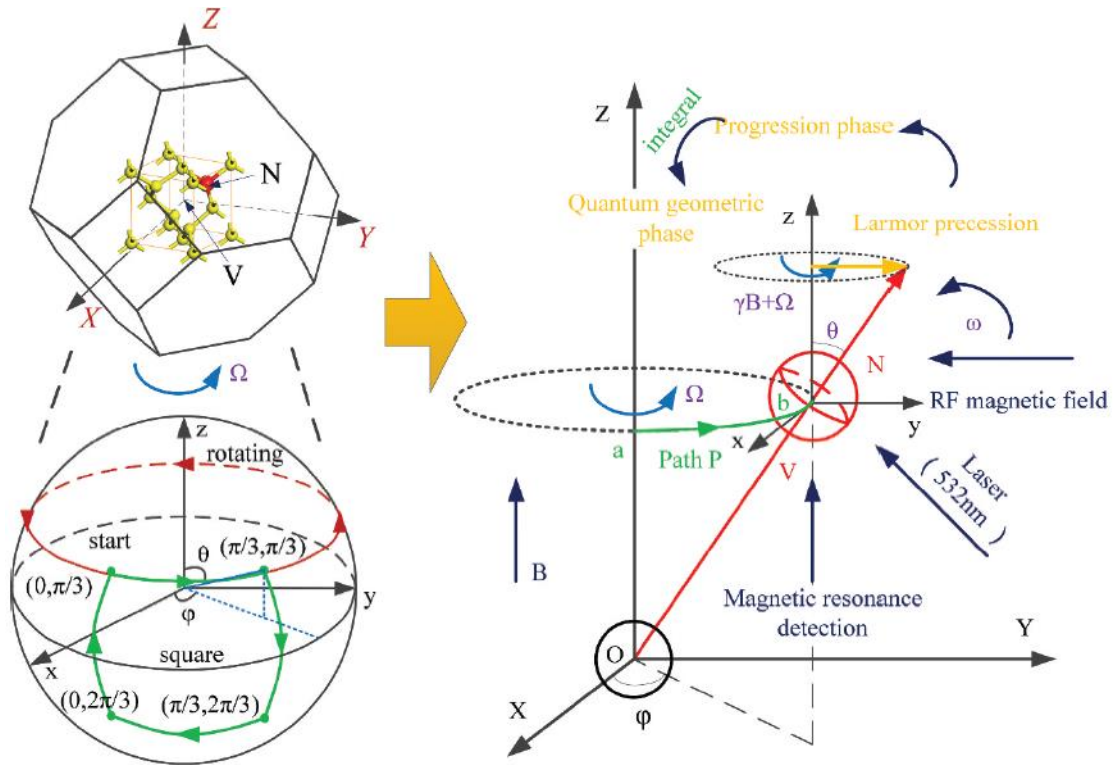
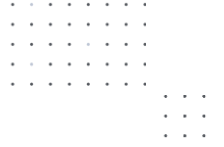


Figure 32. Schematic of rotation measurement.

In the external magnetic field, the physical rotation of the carrier causes a change in the spin precession frequency, and the angular velocity information can be obtained via the quantum geometric phase. Source: [99].

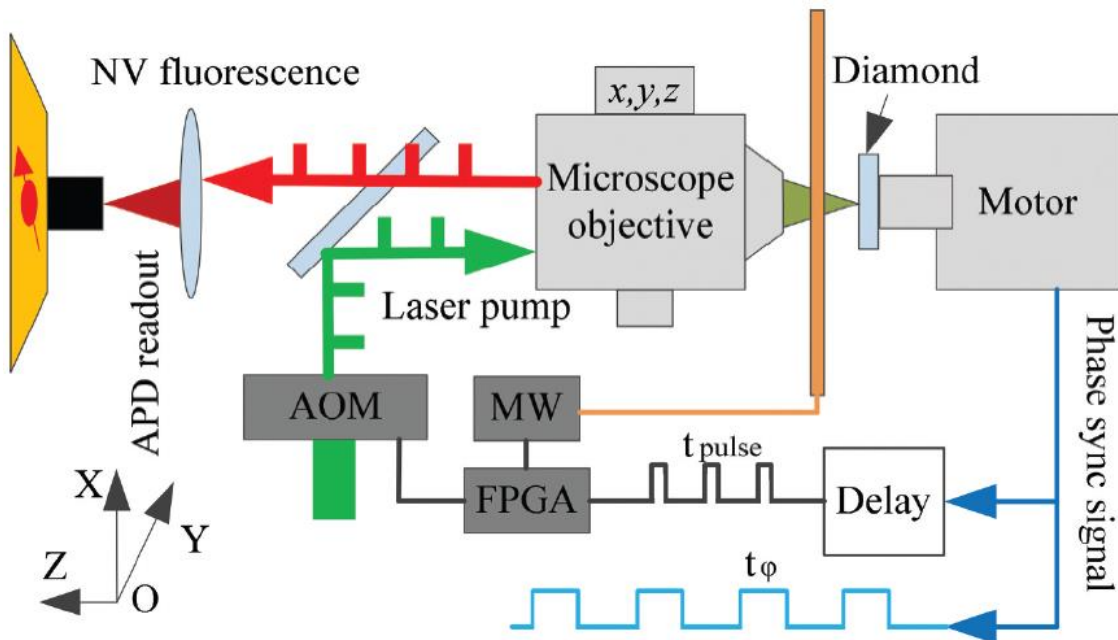


Figure 33. Principle of the rotating test bench.

A single NV center in diamond on the spindle of a rotor. NV centers are optically prepared and addressed by a scanning confocal microscope. MW (produced by the micro coil), magnetic field, and laser are coupled to the NV center. The fluorescence signal is collected by the detector, which contains the angular velocity information. Source: [99].



### 10.3 Sensitivity optimization of spin-based rotation measurement

The sensitivity of rotation measurements is defined as [111]:

$$\eta = \frac{\sqrt{T_2 + t_d}}{CT_2\sqrt{N}}, \quad (\text{Eq. 10.2})$$

Here  $N$  – is the number of sensors,  $T_2$  – is the coherence time,  $C$  – is the fluorescence collection efficiency,  $t_d$  – is the dead time (initialization time and readout time).

Table 13 compares different types of gyroscopes and the NV-based gyroscope in terms of size and measurement sensitivity [99].

**Table 13.** Comparison in sensitivity and size of some representative gyroscopes and the NV- based gyroscope [99].

Types	Sensitivity (rad/s/ $\sqrt{\text{Hz}}$ )	Size
(RLG) ring laser gyroscope	$10^{-11}$	Large
(FOG) fiber optical gyroscope	$10^{-9}$	Large
(AIG) atom interferometer gyroscope	$10^{-8}$	Large
(SERF) spin relaxation free gyroscope	$10^{-6}$	Medium
(MEMS) micro-electro-mechanical systems	$10^{-4}$	Small
NV-based gyroscope	$10^{-6}$	Small

It can be concluded that the new gyroscopes based on NV centers have the potential for miniaturization in the future and an average sensitivity.

To enhance the sensitivity of NV centers gyroscopes, methods are used that increase the coherence time, such as the application of the  $^{14}\text{N}$  nucleus spin, characterised by a much longer coherency, as well as increase in the number of sensors in the ensemble [99].

### 10.4 Nuclear magnetic resonance gyroscopes

The operation of nuclear magnetic resonance (NMR) gyroscopes is based on such a physical property of the atomic nucleus as the presence of a spin sensitive to an external magnetic field. This makes it possible to control transitions between different spin states using radio frequency electromagnetic radiation. Thus, it is possible to achieve polarization of the nuclear spin and the ability to manipulate its state. When exposed to a magnetic field, the spin-polarized nucleus precesses at a Larmor frequency, which depends on the atom and on the magnetic field applied to it. If the spin-polarized nuclei are additionally rotated, they will change the precession frequency in proportion to the applied angular velocity [120].

Initially, it was supposed to create a nuclear spin gyroscope based on the detection of the Berry geometric phase [121]. However, later experimental solutions appeared of gyroscopes of this type using the measurement of the dynamic phase resulting from a rotation-induced pseudo-magnetic field [115].

Berry phase shifts, or geometric phase shifts, are relative phase shifts of magnetic sublevels that occur when the symmetry axis of the system rotates around another axis that is not parallel to itself. This can occur during the evolution of a spin system in time under the action of a magnetic field rotating in space, the vector of which follows a nonzero solid angle. In addition to the phase due to adiabatic evolution under a static Hamiltonian, the eigenstate characterized by the magnetic quantum number  $m$  acquires a Berry phase equal to the product of the solid angle  $d\Omega$  traced by the field and  $m$ . The same effect occurs when the electric field rotates, if the quantization axis is determined





by the electric field. It has been applied to demonstrate a  $^{131}\text{Xe}$  nuclear-spin gyroscope which uses the interaction of nuclear quadrupoles with an electric field gradient. [110].

In the main aspects of their design and implementation, NMR gyroscopes have achieved significant development and improvement both in the methods for controlling atomic rotation and the applied magnetic field, and in the mechanisms for readout the resulting signal [120].

In terms of error budget, NMR gyroscopes approach the requirements of navigation systems. Another important advantage is their resistance to vibrations. They have a motion transduction mechanism that does not require a solid proof mass. It can be expected that within a decade the technology of NMR gyroscopes will reach a level of accuracy acceptable for highly dynamic applications [120].

Whether used for navigation or for keeping aircraft level, modern gyroscopes drift over time and need to be reset every hour or so. Drift-free quantum gyroscopes can be more reliable. Physicist Azure Hansen and a research team at the Colorado National Institute of Standards and Technology (USA) laboratory working on a quantum gyroscope capable of sensing rotational motion hope to have it on the market within a decade to enable safer navigation protocols on land, at sea, in the air, and even in space [122].

## 10.5 Diamond nuclear spin gyroscope

In this subsection, the principle of operation of the diamond nuclear spin gyroscope for rotation motion sensing will be considered in detail using the experimental development proposed in [112] as an example. The described gyroscope operates on the basis of the nuclear spin of the  $^{14}\text{N}$  atom of the NV center in diamond and uses a variation of the highly sensitive double quantum (DQ) Ramsey pulse protocol to readout the resulting signal.

### 10.5.1 The experimental setup description

Figure 34 schematically shows the experimental setup that provides the operation of the nuclear diamond gyroscope. The setup consists of a 35 cm diameter rotating platform controlled by a commercial rate table system (Ideal Aerosmith, 1291BL). A green diode laser 515 or 532 nm and a power of 80 mW, a photodetector and other optical components are fixed on the platform. A single-crystal diamond plate with a concentration of NV centers of  $\sim 4$  ppm and a thickness of 400  $\mu\text{m}$  is placed in an axial magnetic bias field of 482 gauss, created by two thermally compensated samarium-cobalt (SmCo) ring magnets ( $< 10$  ppm/ $^{\circ}\text{C}$ ). The orientation of the bias field along the symmetry axis of the NV center suggests optimal conditions for optical polarization and readout of  $^{14}\text{N}$  nuclear spins [123], while the configuration and arrangement of the magnets that create it minimizes magnetic field gradients in the sensing volume. Part of the setup, including the diamond and the magnets, is placed inside low-carbon-steel magnetic shields to reduce ambient magnetic field noise. An aspherical condenser lens is used both to illuminate a diamond region  $\sim 50$   $\mu\text{m}$  in diameter with a green laser and to collect fluorescence from NV centers. Passing through a bandpass filter from 650 to 800 nm, the fluorescence obtained from NV centers is focused on one of the channels of a balanced photodetector. For the purpose of balanced detection, a small part of the laser radiation is directed to another channel of the photodetector. A copper wire with a diameter of 160  $\mu\text{m}$ , located near the optical focus on the surface of the diamond, creates RF pulses that control the nuclear spin [112].

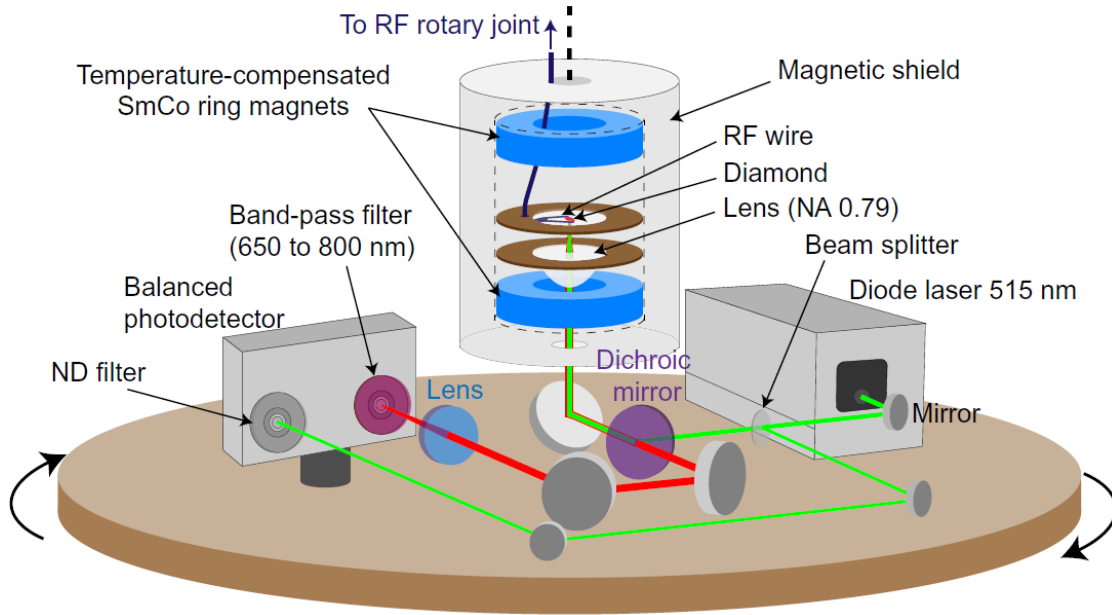


Figure 34. Diamond nuclear spin gyroscope experimental setup.

Electrical connections for the laser and the photodetector are wired to the rotating platform through slip-ring lines. RF signals are delivered to the platform via a single-channel RF rotary joint. NA, numerical aperture. ND, neutral density. Source: [112].

### 10.5.2 Rotation detection principle

The rotation sensing principle based on the precession rate shift measurement of  $^{14}\text{N}$  nuclear spins in the diamond NV center. The energy level diagram of the ground state of the NV center is shown in Figure 35 A. The nuclear spin states (inset)  $|m_I = \pm 1\rangle$  within the manifold of  $|m_S = 0\rangle$  electron spin state are degenerate in a zero magnetic field. Due to the nuclear quadrupole interaction, they are separated from  $|m_I = 0\rangle$  by  $\sim 4.94$  MHz. When an external magnetic field  $B$  is applied, the states  $|m_I = \pm 1\rangle$  split due to the Zeeman effect. The splitting frequency  $f_{\text{DQ}}$  between  $|m_I = +1\rangle$  and  $|m_I = -1\rangle$  can be expressed as [123]:

$$f_{\text{DQ}} = 2B\gamma_n \left( 1 - \frac{\gamma_e A_{\perp}^2}{\gamma_n D^2 - \gamma_e^2 B^2} \right), \quad (\text{Eq. 10.3})$$

Here  $\gamma_n$  and  $\gamma_e$  – are the nuclear and electronic gyromagnetic ratios of the  $^{14}\text{N}$  isotope, respectively;  $D$  – is NV center electron spin zero-photon splitting parameter;  $A_{\perp}$  is the hyperfine magnetic transverse constant [112].

After the initiation of  $^{14}\text{N}$  nuclear spins into a superposition of states  $|m_I = \pm 1\rangle$ , they precess around their quantization axis with a frequency  $f_{\text{DQ}}$ . When an additional rotation of the diamond around this axis occurs with a frequency  $\nu$ , the frequency of the nuclear precession in the diamond reference frame is equal to  $f_{\text{DQ}} + 2\nu$ . As can be seen in Figure 35A, each state  $|m_I = \pm 1\rangle$  is shifted by  $\pm \nu$ , resulting in a factor of 2 in the equation. Accurate measurement of these frequency shifts is required to detect rotation. It is performed using the Ramsey interferometry method [112].

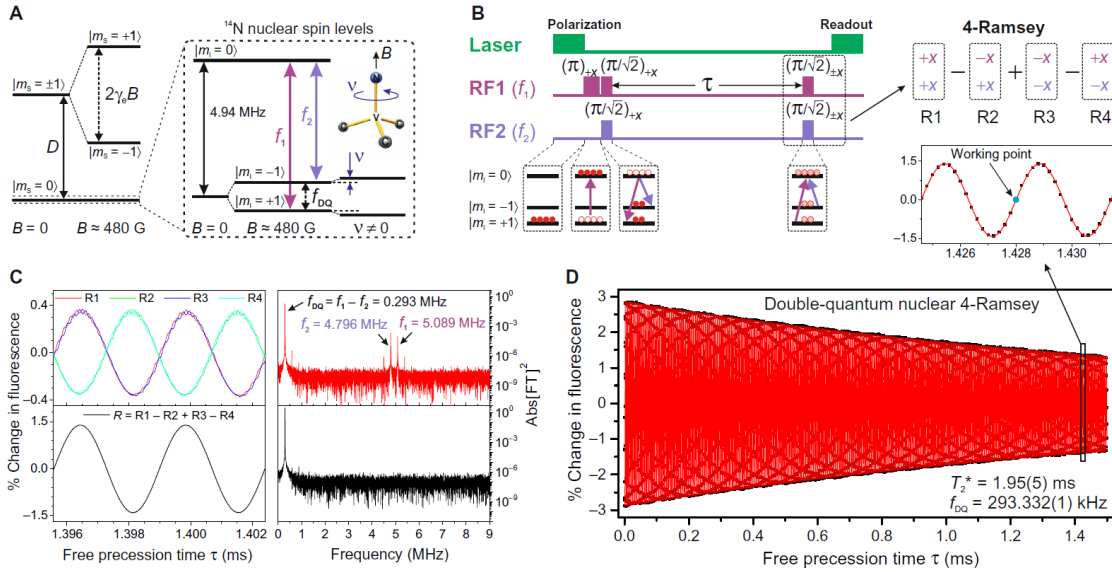


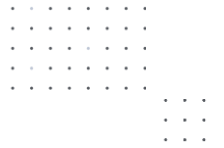
Figure 35. Nuclear spin gyroscope measurement protocol

DQ measurement protocol using  $^{14}\text{N}$  nuclear spins in diamond. (A) Energy-level diagram of the NV center ground state with and without a magnetic field  $B$  applied along the NV axis. The inset depicts the  $^{14}\text{N}$  nuclear spin levels, where the splitting between the  $|m_l = \pm 1\rangle$  sublevels depend on the applied field and on the rotation of the sample around the NV axis. Rotation sensing is based on the measurement of this interval. (B) DQ nuclear Ramsey pulse sequence. Inset: 4-Ramsey phase cycling measurement scheme. (C) DQ nuclear Ramsey fringes (R1, R2, R3, and R4) obtained by sequentially alternating phases of the last double quantum pulse as depicted in the inset of (B). The frequency-domain spectrum shows the square of the absolute value of the Fourier transform, which reveals DQ signal at  $f_{\text{DQ}}$  frequency and residual single-quantum (SQ) signals at  $f_1$  and  $f_2$  frequencies. Bottom left: DQ nuclear 4-Ramsey fringes obtained by combining four DQ sequential Ramsey measurements  $R = R1 - R2 + R3 - R4$  to cancel residual SQ signals. (D) DQ nuclear 4-Ramsey fringes. Symbols represent experimental data, while the solid line is an exponentially decaying sine wave fit. The oscillation frequency of the signal corresponds to the  $f_{\text{DQ}}$ , while an exponential decay time corresponds to the nuclear DQ spin coherence time  $T_2^* = 1.95(5)$  ms. Inset: Zoomed plot of DQ 4-Ramsey fringes near the working point; rotation measurements were performed at a fixed free precession time  $\tau \approx 1.4$  ms by monitoring changes in the fluorescence signal. Source:[112].

### 10.5.3 Measurement protocol description

A diagram depicting the sequence of DQ Ramsey pulse protocol used in this experiment is shown in Figure 35 B. First, the  $^{14}\text{N}$  nuclear spins are brought into the state  $|m_l = +1\rangle$  by a  $300 \mu\text{s}$  green laser pulse. At the next step, the population is transferred to the state  $|m_l = 0\rangle$  by an RF  $\pi$ -pulse with a frequency  $f_1$  and a duration of  $37 \mu\text{s}$ . After that, irradiation with a two-tone resonant RF  $\pi/\sqrt{2}$ -pulse with frequencies  $f_1$  and  $f_2$  corresponding to the nuclear spin states transitions induces DQ coherence between  $|m_l = +1\rangle$  and  $|m_l = -1\rangle$  states. During the subsequent interval of free precession  $\tau$ , there is an accumulation of a phase proportional to the measured value. The new two-tone resonant RF pulse transforms the phase accumulated between the two states of the nuclear spin  $|m_l = \pm 1\rangle$  into an optically readable population difference. As a result of applying such a pulse sequence, the population oscillates with a frequency  $f_{\text{DQ}} + 2\nu$  depending on a free precession time  $\tau$  [112].

Due to gradients of RF pulses across the sensing volume, residual single-quantum (SQ) transitions at frequencies  $f_1$  and  $f_2$  appear, which are sensitive to temperature fluctuations and degrade the reliability and performance of the measurement process. In the described experiment, in order to remove parasitic SQ signals, the "4 Ramsey" measurement protocol proposed in [124] for electron spins was extended to nuclear spins [112].



In the nuclear 4-Ramsey DQ method (Figure 35 B, inset), 4 Ramsey DQ sequences are formed one after the other with alternating second pulse phase. As seen in Figure 35 C (top right), the Fourier transform of the individual  $^{14}\text{N}$  DQ nuclear Ramsey signals (represented in Figure 35 C (top left)) includes residual SQ signals at the frequencies  $f_1$  and  $f_2$ , in addition to the DQ signal at the frequency  $f_{\text{DQ}}$ . These signals (from R1 to R4) were measured by sequentially alternating the phase of the second DQ pulse at each delay  $\tau$ . Combining four DQ Ramsey signals:  $R=R1-R2+R3-R4$  (Figure 35 C (bottom left)) results in the elimination of residual SQ signals, which can be observed in the Fourier transform of the combined DQ 4-Ramsey signal (Figure 35 C (bottom right)) [112].

The resulting  $^{14}\text{N}$  DQ nuclear 4-Ramsey fringes, which can be seen in Figure 35 D, are fit to an exponentially decaying sinusoidal function  $R(\tau) = Ae^{-\tau/T_2^*} \sin(2\pi f_{\text{DQ}}\tau + \phi)$ , from which the nuclear spin coherence time  $T_2^*=1.95(5)$  ms and the oscillation frequency  $f_{\text{DQ}}=293.332(1)$  kHz can be inferred [112].

To ensure the greatest sensitivity to changes in the phase of oscillations, the measurements were performed at a fixed free precession time  $\tau_{\text{wp}} = 1.428$  ms (labelled as working point on Figure 35 D, inset). To convert signal changes into frequency shifts, the calibration coefficient  $\alpha_0=4\pi \cdot \tau_{\text{wp}} \cdot A=6.56(6) \times 10^{-5}\%/(^\circ/\text{s})$  was used, determined by the amplitude  $A$  of the DQ 4-Ramsey fringes in the vicinity of the working point  $\tau_{\text{wp}}$ . The bandwidth of the presented diamond gyroscope under the conditions of the described experiment is  $1/(2T_{\text{cycle}})\approx 70$  Hz, where  $T_{\text{cycle}}$  is the duration of the DQ 4-Ramsey sequence [112].

## 11. ACCELERATION MEASUREMENT USING NV-CENTER SENSORS

Currently, studies are underway on the possibility of using sensors based on NV centers as accelerometers or gravimeters, which, along with magnetometers and gyroscopes, can be applied in inertial navigation systems and in other applications. The study of the possibility of a coupling between mechanical vibrations and the states of the spins of NV centers, except for its application in devices that measure acceleration, is important for experiments on the development of quantum information processes and for fundamental researches of mesoscopic quantum effects. This chapter will discuss some of these ideas for possible applications of sensors based on NV centers.

### 11.1 Spin-based acceleration measurement

The development of interferometric methods for measuring acceleration proceeded from waves to matter, which has shorter de Broglie wavelengths and, as a result, is more sensitive to phase shift changes. Thus, matter-wave interference with such particles as electrons, neutrons, and atoms was first demonstrated, and with the development of optomechanics, nanodiamond particles containing an NV center began to be considered in this context. It was shown that, due to their quantum mechanical properties, diamond particles can act as nanoscale resonators and create macroscopic superposition states by levitating in optical tweezers [125]. Later, in order to increase the accuracy of interferometric measurements of the phase shift caused by gravity, a scheme was proposed for the formation of a superposition of a nanodiamond hybrid containing an NV center and a macroscopic mechanical resonator [126], [127]. Methods are being developed that make it possible to couple the spin of an NV center with a mechanical resonator, which have wide application prospects. For example, the movement of a mechanical cantilever in a hybrid system with an NV center or a magnetic tip attached to its end can be detected by one or more NV centers due to the magnetic field gradient [128]. With the development of optomechanics [129], [130], such a nanodiamond containing an NV center became capable of realizing a high-quality factor [118], [21] by levitating under the action of an optical force [99].

### 11.2 Sensing mechanism of spin-based acceleration measurement

Spin-oscillator coupling schemes that create a spatial superposition due to the interaction with the external magnetic field gradient of an embedded two-level system, such as an NV center in diamond, have been proposed as accelerometers [131], [132]. Due to the phenomenon of the matter-wave interference, a high-precision measurement of gravity can be performed by a hybrid system that couples the electron spin of an NV center with a nanomechanical resonator. Since more massive objects make it possible to measure acceleration with greater accuracy, nanodiamond schemes demonstrate a relative phase difference measurement accuracy three orders of magnitude greater than schemes using atomic interference, and the relative accuracy of the gravitational acceleration measurements is estimated for schemes based on NV centers of the order of  $10^{-10}$  [126]. Figure 36 shows some of these hybrid schemes proposed in various studies [99].

As the first example, below the scheme of an optically levitating nanodiamond is analyzed in detail (Figure 36a). The movement of the center of mass (CoM) of a nanodiamond, which is trapped by light force tweezer in a vacuum environment, is coupled with the spin of the embedded diamond NV center through a magnetic field gradient. The magnetic tip is placed close to the diamond to create the required magnetic field gradient along the z direction. In assumption that the trapping frequency  $\omega_z$  is small enough compared to  $\omega_x$  and  $\omega_y$ , the effect of motion along the x and y directions can be neglected. Taking into account the gravitational field of the Earth, the corresponding Hamiltonian [117] has the form [99]:

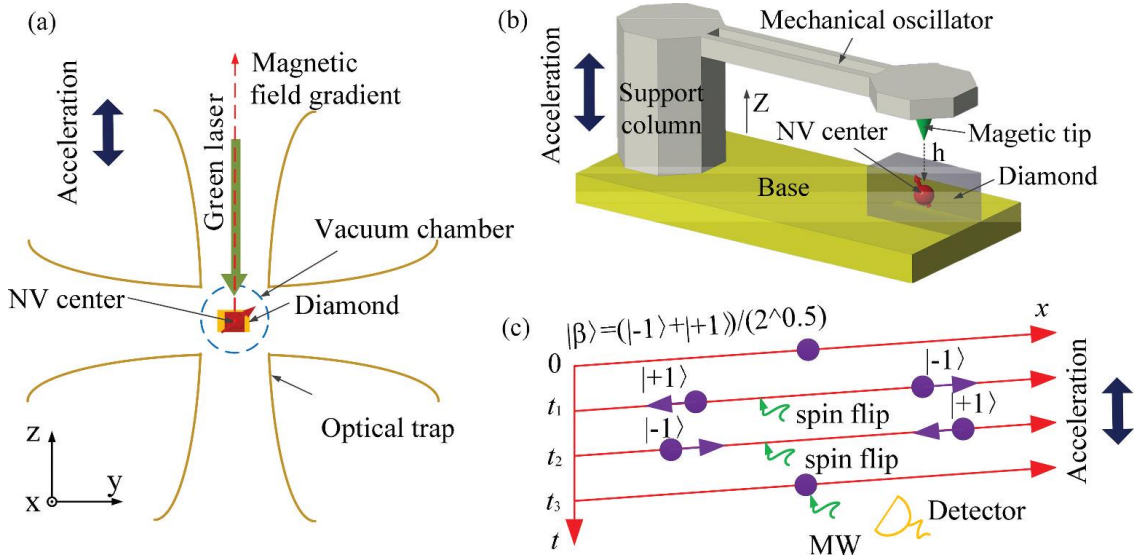


Figure 36. Spin-oscillator coupling acceleration sensing schemes based on NV center.

(a) the optical tweezer or (b) the cantilever. (c) The free-flight acceleration sensing scheme using a Ramsey interferometer facilitates the possibility of realizing a larger superposition. The spin superposition creation, the spin states flipping (at times  $t_1$  and  $t_2$ ) and wave packet merger (at time  $t_3$ ) are controlled by microwave pulses. Source: [99].

$$H = \hbar DS_z^2 + \hbar \omega_z c^\dagger c - 2(\lambda S_z - \Delta \lambda) (c + c^\dagger) \quad (\text{Eq. 11.1})$$

Here  $\lambda = g_{NV} \mu_B B_z \sqrt{\frac{\hbar}{2m\omega_z}}$  – is the spin-motion coupling strength;  $\Delta \lambda = \frac{1}{2} mg \sqrt{\frac{\hbar}{2m\omega_z}}$  – is the gravitational displacement;  $g_{NV}=2$  – is the electron Landé g-factor;  $m$  – is the mass of the nanoparticle;  $\mu_B$  – is the Bohr magneton;  $B_z$  – is the magnetic field gradient, along the acceleration-sensitive  $z$  axis;  $c$  and  $c^\dagger$  are the annihilation and creation operators, respectively. It can be concluded that, depending on the eigenvalues  $S_z$ , the motion of the oscillator CoM changes [99].

To measure the phase shift of a hybrid spin-resonator system [126] uses the Ramsey method and the Feynman path integral approach to interferometry [133]. The relative phase shift that occurs under the action of gravitational acceleration  $g$  between two energy levels of the NV center is defined as [126]:

$$\Delta \phi = \frac{16\lambda \Delta \lambda t_0}{\hbar^2 \omega_z} = \frac{g_{NV} \mu_B B_z g t_0^3}{\pi^2 \hbar} \quad (\text{Eq. 11.2})$$

Here  $t_0=2\pi/\omega_z$  – is oscillation period. The phase shift is proportional to the gravitational acceleration  $g$  and can be precisely determined by the spin state population readout [99].

The next example of such hybrid spin-oscillator systems is shown in Figure 36b. In this system, in order to couple the mode of mechanical vibrations of the oscillator to the state of the electron spin of the NV center in diamond, a magnetic tip is attached to the cantilever resonator, which creates a magnetic gradient near the electron spin. To manipulate and readout the spin states, as in the previous case, the Ramsey method is used [99].

To measure the mass-independent dynamic phase that appeared under the influence of spin-dependent gravitational potentials, it was proposed to use an interferometric scheme with an untrapped nanodiamond containing an NV center (Figure 36 c) [125], [134], [135]. To couple the state of the electron spin of the NV center to the motion of the



CoM of diamond, as in the previous cases, the magnetic field gradient is used. With the help of MW-pulses, a spin superposition is created at the time  $t_1$ , and the spin states are flipped at the time  $t_2$ . By splitting, accelerating, decelerating and merging the wave packet, a fluorescent signal containing information about the phase factor proportional to gravity is obtained [99]:

$$\Delta\phi = \frac{1}{16\hbar} g_{NV} \mu_B B_z a t_3^3 \cos(\theta) \quad , \quad (\text{Eq. 11.3})$$

Here  $t_3$  – is the total time of free fall;  $\theta$  – is the angle between the acceleration direction and the applied magnetic field  $B_z$ . Due to its independence from the mass, this free-flight scheme facilitates the realization of a larger superposition compared to methods using levitation [99].

### 11.3 Sensitivity optimization of acceleration measurement

The acceleration measurement accuracy of matter-wave interferometry, due to the shorter de Broglie wave, is higher than that of the light interferometers. With the correct parameter settings, a gravimeter based on a diamond resonator will exceed in measurement accuracy a gravimeter based on cold atoms, due to the larger mass of the nanodiamond. Thus, in comparison with sodium atoms, the resonator of an optical spin-oscillator sensing system is  $10^{10}$  times more massive, and the resonator of the cantilever spin-oscillator system is  $10^{16}$  times more massive [99].

According to [126], the equation (11.2) can be rewritten as:

$$\Delta\phi = \frac{16\pi m g \Delta z}{\hbar \omega_z} \quad . \quad (\text{Eq. 11.4})$$

Here  $\Delta z$  – is the size of the interferometer and  $m$  – is the mass of the resonator. Thus, at a fixed integration time  $t_0 = 2\pi/\omega_z$ , a large resonator mass makes it possible to obtain a larger phase shift  $\Delta\phi$  within a smaller interferometer. Therefore, accelerometers based on NV centers, which have a higher mass, have a higher potential for miniaturization and the possibility of integration in a chip [99].

Other possible advantages of NV center-based instruments over conventional atomic inertial sensors are the faster start-up time and the ability to operate at normal temperatures, leading to additional potential miniaturization since an air chamber is not required [99].

The parameters and characteristics of the proposed designs of accelerometers based on NV centers in many aspects have the potential for future improvements. Optical tweezers were originally investigated as a basic system for constructing light force accelerometers [130], therefore, in the case of using this tool to create the macroscopic superposition states of the NV center spin, further research is needed in the field of levitating optomechanics in order to provide a more accurate determination of the position of a nanodiamond, reliable control of the spin state cooling, and stable collection of the fluorescence (limited only by shot noise) [129]. For example, using a fiber with total internal reflection can significantly improve the efficiency of photoconversion. Through various active or passive methods, improved stabilization of temperature and magnetic fields can be achieved to increase the long-term performance of the sensor. In particular, a greater resistance of the device to the field fluctuations in the environment can be achieved using schemes that implement feedback control over the magnetic field [136]. Also, by optimizing the properties of the initial material used to create sensors, it is possible to improve the characteristic times of dephasing and coherence of the spin states, which significantly affect the sensitivity of measurements [99].



## 11.4 Hybrid opto-mechanical systems with nitrogen-vacancy centers. Atomic accelerometers

The methods applied to couple NV centers and mechanical oscillators can be divided into two main types [21]:

1. Methods that use the coupling of a strong magnetic field gradient and the mechanical oscillators with the NV centers [117].
2. Methods using a strain-induced effective electric field for coupling the phonon mode with the electron spins of NV centers [137].

Both these methods make it possible to achieve a strong coupling mode, when it is possible to cool a mechanical oscillator by means of a coherent exchange of the excitations between the motion degrees and the spin states [138]. It becomes possible to generate arbitrary superposition of states of a mechanical oscillator, implement a phonon laser<sup>5</sup>, and squeezing<sup>6</sup> in the system [139]. Also, due to the possibility of interacting with many different degrees of freedom, such a system can be used to process a quantum information [21].

The motion of a nanoparticle in an optical trap can be cooled to temperatures of the order of mK using feedback without cavity. By exchanging excitations between the spin and phonon degrees, or by cooling the cavity sideband, the ground state can be reached. In such systems the matter wave interference can be observed even in thermal states. Thus, it is possible to realize an ultrasensitive mass spectrometer even at room temperature by detecting the coherence of NV center spin [21].

### 11.4.1 Inertial sensing technology based on levitated optomechanics

Levitated optomechanics is a field of science that provides the measurement of states and control of micro- or nanoscale mechanical oscillators and is a combination of quantum optics and optomechanics. Quantum methods of levitated optomechanics have broad prospects for application and development. They are used to measure physical parameters such as acceleration, displacement, force, torque and others, demonstrating extremely high sensitivity at a room temperature. Due to their unprecedented observational precision, levitated optomechanics methods have the potential to not only approach, but even go beyond, standard quantum limits. Currently, there is an active transition of the methods of this disruptive technology (especially in the areas of inertial sensing and highly precision measurement) from the stage of fundamental research to applied engineering [98].

Most research in the field of creating high precision quantum devices is based on these two main principles) [98]:

- the cold atom interferometry (cold atomic gyroscope, cold atomic gravimeter, cold atomic accelerometer);
- the hot atom spin principle (magnetic resonance gyroscope, the spin-exchange relaxation free gyroscope).

Due to the advancing of the methods of levitated optomechanics, there are new opportunities for the development of quantum inertial sensing instruments outside the scope of both the cold atom interferometry and the hot atom spin principle [98].

---

<sup>5</sup> A phonon laser is a device that coherently amplifies phonons (vibration quanta), similar to a conventional laser that coherently amplifies photons (light quanta).

<sup>6</sup> In quantum physics, a squeezed state of light is such a state when the strength of its electric field for some phases has a smaller quantum uncertainty than that of a coherent state. Thus, the term squeezing refers to reduced quantum uncertainty.



Based on levitated optomechanics, quantum inertial sensing technology has the following characteristics [98]:

- a. Solid state sensing unit. Highly dynamic measurements are performed continuously and in real time by a micro- or nano-scaled levitating solid medium which is represent the sensing unit.
- b. Ultra-sensitivity. The theoretical sensitivity of a suspended micro- or nano-scaled solid medium can reach much higher values than that of a classical solid-state inertial sensor, because the equivalent thermal temperature of its CoM movement can be reduced to  $\lesssim 1$  mK, and the mechanical quality factor of such a levitating medium can reach  $> 10^{10}$ .
- c. High resolution. The recoil momentum of photons, which reaches very high values for levitating systems, sets the limit of their resolution and amounts, for example, to  $10^{-17}$  g for a single photon when a levitating quartz sphere of  $10 \mu\text{m}$  in diameter is used to measure the acceleration.
- d. High stability. While the key stability issue of a conventional solid-state sensor is the stress-time effect caused by the mechanical support, an optically levitated in a vacuum micro- or nano-scaled solid-state medium can completely avoid this effect.
- e. Large range. The wide measurement range of the levitating sensor is given by the closed-loop control ability of the photon momentum and can reach  $> 10$  g at closed-loop control with a laser power of 100 mW for an acceleration-sensitive levitating quartz sphere with a diameter of  $10 \mu\text{m}$ .

The capabilities of levitating optomechanics also have the potential to revolutionize the field of sensors and precision measurements by transferring a micro- or nano-scaled mechanical oscillator into the quantum realm to develop inertial sensing technologies from optical or atomic interferometry (represented by devices such as an optical gyroscope, cold atomic gravimeter or cold atomic gyroscope) to solid-state matter-wave interferometry [98].

#### 11.4.2 Magnetic field gradient induced coupling

Figure 37 illustrates the idea of a strong magnetic coupling between the electron spin of the single NV center in diamond and a mechanical oscillator with a magnetic tip. Other engineering solutions of such a system are also possible, when the magnet, on the contrary, is fixed motionless, and a diamond containing an NV center is attached to the end of the mechanical oscillator. The energy states of the electron spin experience Zeeman shifts under the action of a time-varying magnetic field created by vibrations of a mechanical oscillator whose frequency is  $\omega_r$ . The energy shift corresponding to one quantum of motion is defined as [117]:

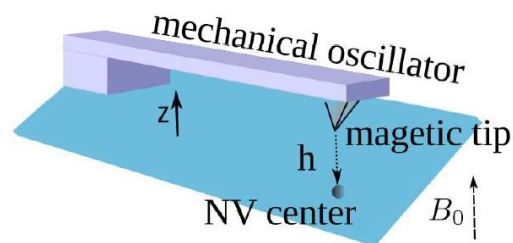


Figure 37. Magnetic coupling between a mechanical oscillator and a NV center

A magnetic tip, which is attached to the end of a cantilever, is placed at a distance  $h$  above a single NV center. It creates a strong magnetic gradient near the electronic spin of the NV center. As the spin energy is in proportional to the magnetic field, a strong coupling between the NV center electrons spin and the motion of cantilever is created. Laser field is used for initializing and measuring the spin states. Microwave is used for manipulating the spin states. Source: [21].

$$\lambda = g_s \mu_B G_m a_0. \quad (\text{Eq. 11.5})$$

Here  $g_s \cong 2$  – is electron g-factor,  $\mu_B$  – is the Bohr magneton,  $G_m$  – is the magnetic field gradient,  $a_0 = \sqrt{\hbar/2m\omega_r}$  – is the zero-field fluctuation for a resonator of mass  $m$ .

Experimental studies of such hybrid systems show that the value of  $\lambda$  can reach 100 kHz and provide a higher sensitivity than high-quality mechanical resonators with a decay rate  $\gamma = \omega_r/Q$  and a spin coherence time of 1 ms [117].

### 11.4.3 Applications as resonator cooling

The methods of cooling and quantum manipulation of the states of motion of nanomechanical resonators are currently being actively developed under the influence of the ideas of quantum informatics, the possibility of potential applications of these techniques for nano-scale sensing and with the aim of testing quantum mechanical laws for macroscopic objects. Work in this direction is carried out with optical cavities, superconducting devices or cold atoms. Also, a very promising object for such research is the NV center in diamond, being a well-controlled two-level system. Thus, in [117] and [140] for a single NV center, and in [141] for NV-ensemble, using optical pumping methods, it was possible to induce a coherent exchange between spin and motional excitations, to achieve the ground state cooling and controlled generation of arbitrary quantum superpositions of states of a nanomechanical resonator coupled to electronic spin states of NV center in diamond.

### 11.4.4 Applications in quantum information processing

After preparing the mechanical ground state, a hybrid system based on a coupled to NV center nanomechanical resonator can be used to process quantum information. It is also possible to achieve distant coupling between the resonators by charging a mechanical oscillator [21].

By coupling multiple NV centers with the same mechanical oscillator, which plays the role of a quantum bus, it is possible to entangle distant NV centers. Such a scheme is shown in Figure 38 [142]. Here, qubits encoded by two spin levels  $|0\rangle$  and  $|-1\rangle$  are created by an array of NV centers located at an equal distance from each other, over which magnetic tips are fixed one-to-one at the end of the cantilever. MW radiation is used to control all spins of NV centers array. Such high-accuracy experiments make it possible to generate spin entanglement of NV centers [21].

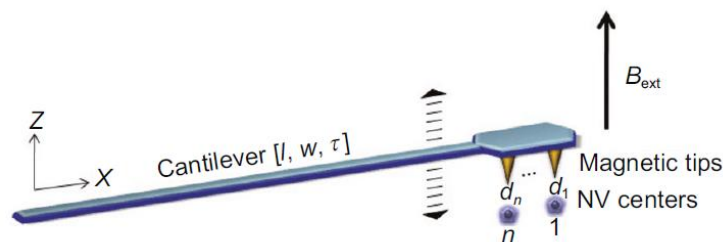


Figure 38. Multiple NV centers spins that couple with mechanical oscillator

A scheme to entangle multiple NV centers spins that couple with the same mechanical oscillator. An array of evenly spaced magnetic tips are attached at the end of a nanomechanical cantilever, under which are one-to-one correspondent NV centers. Source: [142].

To implement a scalable quantum information processor, the above idea can be extended by fabricating an array of  $N$  nanomechanical resonators (Figure 39) [143]. Each resonator is coupled to the located under it in the substrate, an electronic spin qubit created on the basis of the NV center in diamond. With a magnetic gradient of  $10^7$  T/m,

the resulting spin-phonon coupling can reach 100 kHz. Charging the resonator and capacitively coupling it to a nearby wire allows for a long-range interaction between distant sites [21].

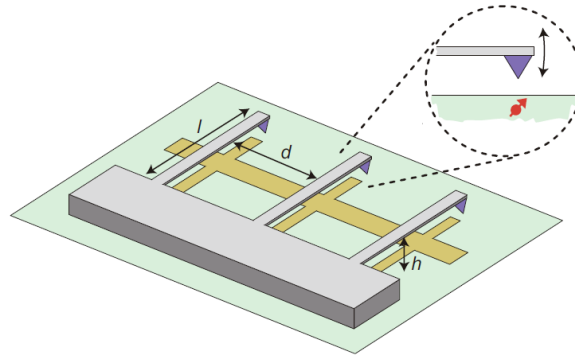


Figure 39. Schematic view of a scalable quantum information processor on an electromechanical quantum bus and NV centers spins as qubits. Source: [143].

### 11.4.5 Applications in ultra-sensitive measurement

For supersensitive measurements of the states of a mechanical resonator, the spin of the NV center coupled to it can be used. The Brownian motion of the resonator in the classical regime can be detected in this way even when the strong coupling conditions are not satisfied [21].

Such a hybrid system is implemented in [144], (Figure 40). At the end of the SiC nanowire, a nanodiamond containing a single NV center is fixed, affected by a strong magnetic field gradient, which couples the spin states to nanowire motions. Thus, by readout a single electron spin of the NV center the movement of the nanowire can be investigated [21].

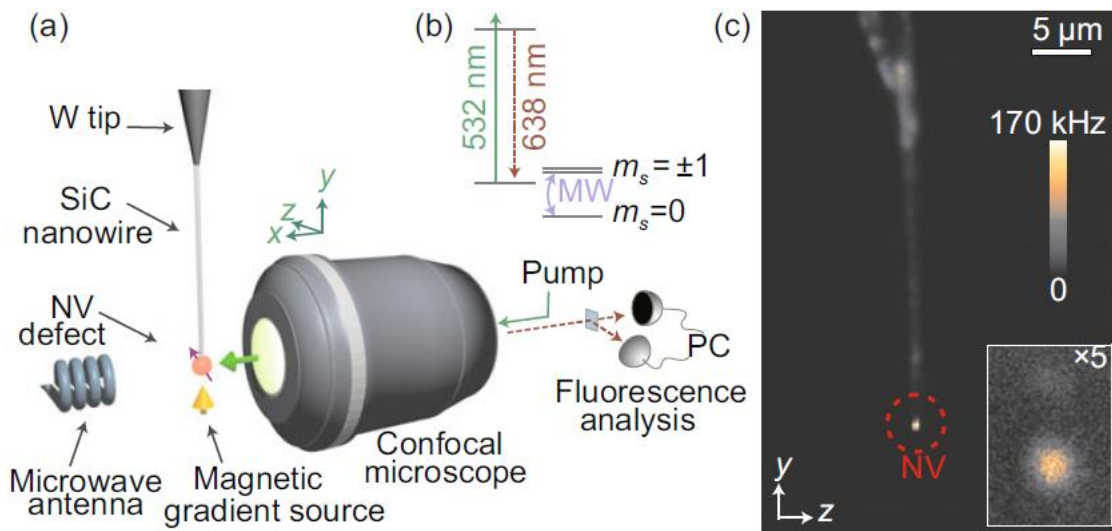


Figure 40. A hybrid system in which a single nitrogen-vacancy center coupled with a nanomechanical oscillator.

(a) A confocal microscope monitors the fluorescence of a single NV defect hosted in a diamond nanocrystal placed at the extremity of a SiC nanowire. A microwave antenna is used to manipulate the NV electronic spin, while a micro-fabricated magnetic structure approaching in the vicinity of the suspended NV center generates a strong magnetic field gradient. (b) The electronic levels structure of the NV centers at zero magnetic field. (c) Fluorescence map of the system recorded with the confocal microscope while scanning the objective position. The isolated bright spot circled in red corresponds to the fluorescence of a single NV center. Inset: Enlarged view of the nanowire extremity. Source: [144]



Another experiment [128] achieved coherent coupling of a single spin of an NV center with a magnetized mechanical cantilever. By measuring the spin coherence of the NV center, it was possible to control the movement of the cantilever despite the fact that the changes in the magnetic field caused by it were very small. The accuracy achieved in the experiment was  $\sim$  pm under ambient conditions. The spin echo protocol was used for measurements, which filtered out unwanted background noise and amplifies the useful signal generated by the magnetic field due to the movement of the cantilever [21].

## 12. MAGNETOMETER PROTOTYPES AND COMMERCIALLY AVAILABLE MAGNETOMETERS ON NV-CENTERS

The literature describes designed prototypes of compact magnetometers intended for use in various fields such as navigation, geology, biology or medicine. Scanning microscopes with sensitive tips on diamond NV centers are also described. In addition, commercial companies have recently emerged offering magnetometers, relaxometers or microscopes at NV centers for both practical application and research purposes or for use in the educational process.

### 12.1 Integrated magnetometers prototypes

The equipment used in laboratory experiments, designed to carry out measurements with the help of sensors based on NV centers, is a series of separate bulky instruments. In order to facilitate the implementation of this new technology in practical applications, the corresponding devices should be replaced by more compact designs. Two of such recently proposed prototypes of integral hand-held magnetometers based on the NV centers in diamond with a sensitivity of the order of nT [145], [146], [147]. ] are presented in Figures 41, 42.

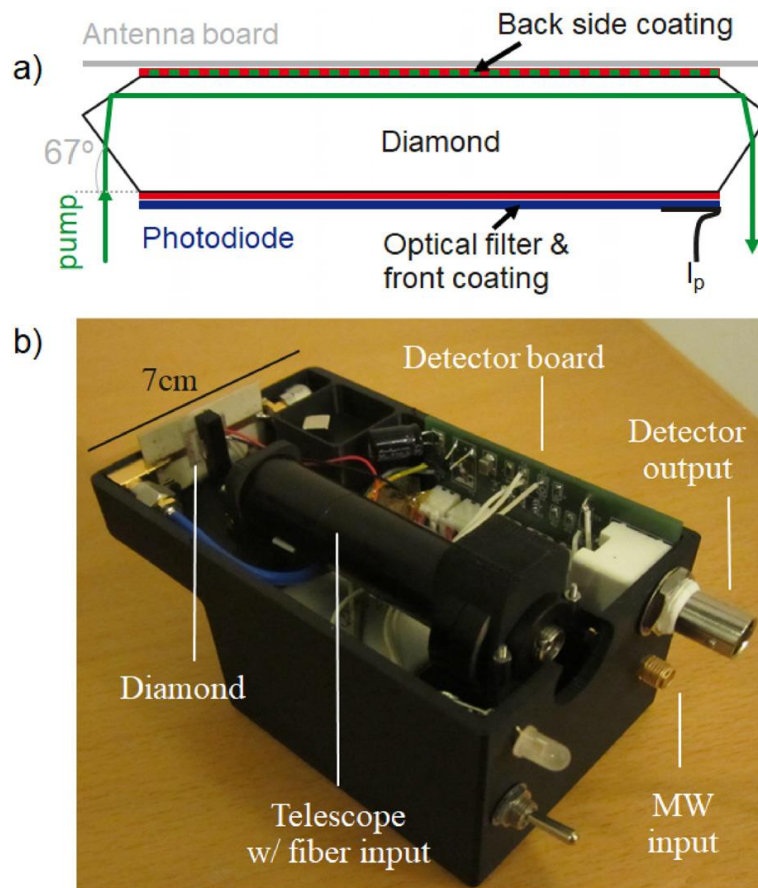


Figure 41. The hand-held magnetometer

(a) Schematic of the specially cut diamond crystal, optical coatings and filter, attached photodiode, and MW antenna. Two cut surfaces, one at the diamond Brewster angle ( $67^\circ$ ) was used to ensure maximum transmission of a beam perpendicular to the diamond front surface and a second cut at  $22.7^\circ$  to direct the beam laterally through the entire width of the diamond, exciting the maximum number of NV centers as possible and exiting at an identically cut facet on the opposite side. (b) Labeled photograph of the opened handheld sensor head. Source: [145].

Another of the proposed methods for integrating sensors based on NV centers involves the use of a standard complementary metal-oxide semiconductor (CMOS) technology

[148], [149] (Figure 43), with which on an area of  $200\ \mu\text{m} \times 200\ \mu\text{m}$  the main components used to control and measure the spin states of NV centers (MW generator, optical filter, photodetector) can be integrated.

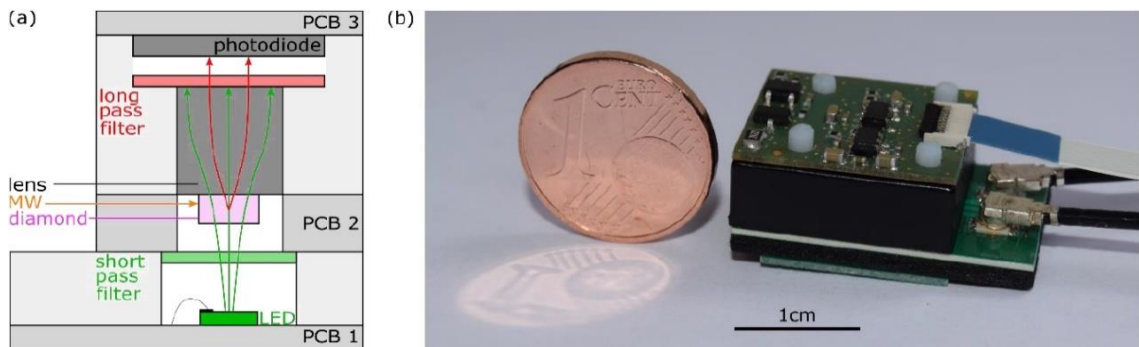


Figure 42. Miniaturised and integrated magnetometer based on NV- centers.

(a) Schematic of the sensor assembly with a construction volume of  $2.9\ \text{cm}^3$ . (b) Image of the sensor device placed next to an Euro cent coin. The ribbon cable is used for the power supply of the integrated electronics and for the readout of the photodetector. Source: [146].

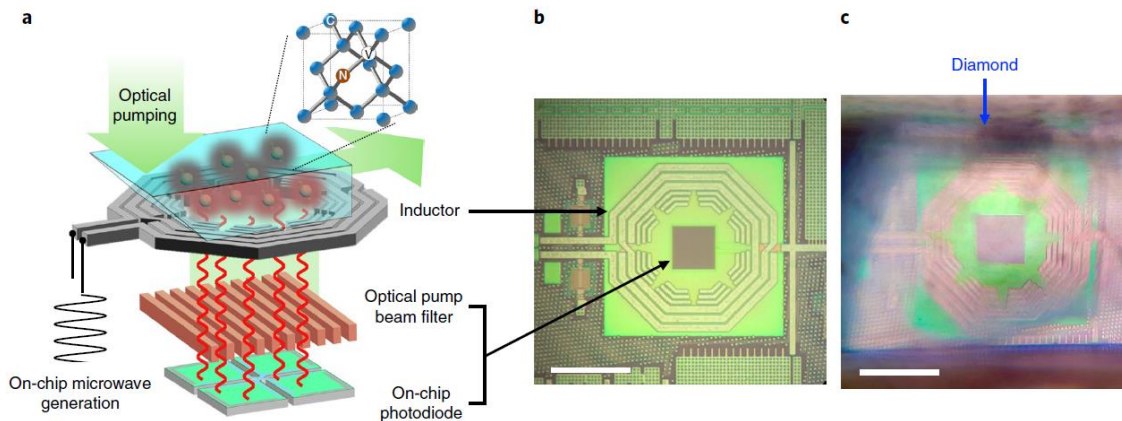


Figure 43. CMOS-integrated quantum sensing architecture.

**a**, A green pump laser excites an NV ensemble in the diamond slab. Microwave fields generated on-chip manipulate NV electron spins through an on-chip inductor, leading to ODMR. A metal/dielectric grating absorbs the green pump beam and transmits the NV spin-dependent fluorescence to the on-chip photodiode. Inset: NV atomic structure. **b**, **c**, Top-view micrographs of the fabricated CMOS chip without (**b**) and with (**c**) the diamond slab. Scale bars,  $200\ \mu\text{m}$ . Source: [148].

An integration option using optical fibers has also been proposed [150]. A diamond chip containing an NV center is attached to the end of the optical fiber. A hybrid fiber-optic NV center thermometer based on this engineering solution is shown in Figure 44.

In order to increase the efficiency of excitation and collection of fluorescence and improve the spatial resolution, various improvements can be made to such designs, for instance the use of additional mirrors or application of a conical optical fiber in an endoscope-like configuration [151].

Also, for the implementation of distributed magnetometry sensing at extended lengths, nanodiamonds doped into fibers were used. This implementation applies a hollow optical waveguide containing a fluid with nanodiamonds and a thermally drawn fiber with hundreds of embedded parallel-connected photodiodes [152]. To provide the required microwave excitation, the fiber is placed in a larger coaxial cable (Figure 45).

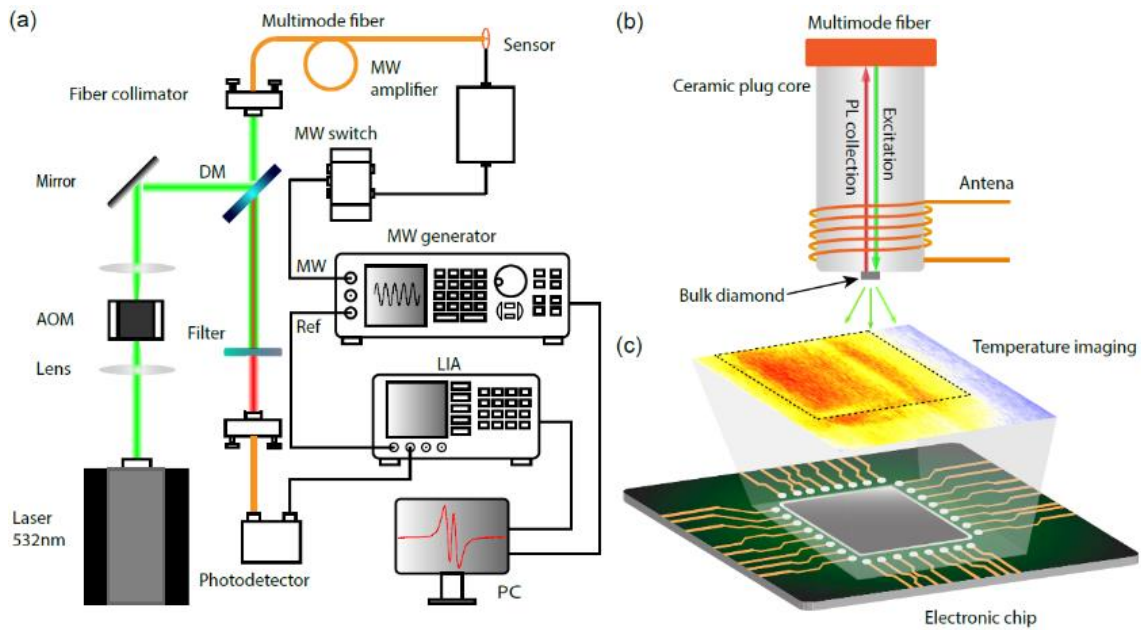
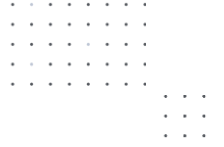


Figure 44. The hybrid fiber-optical thermometer setup

(a) The schematic of hybrid fiber-optical thermometer setup. DM – long-pass dichroic mirror with the edge wavelength of 658.8 nm; Ref. – the output reference signal from MW generator; AOM – acousto-optical modulator; LIA – lock-in amplifier. (b) Simplified schematic of the sensor. (c) An electronic chip used for temperature imaging via the fiber-based quantum thermometer. Source: [150].

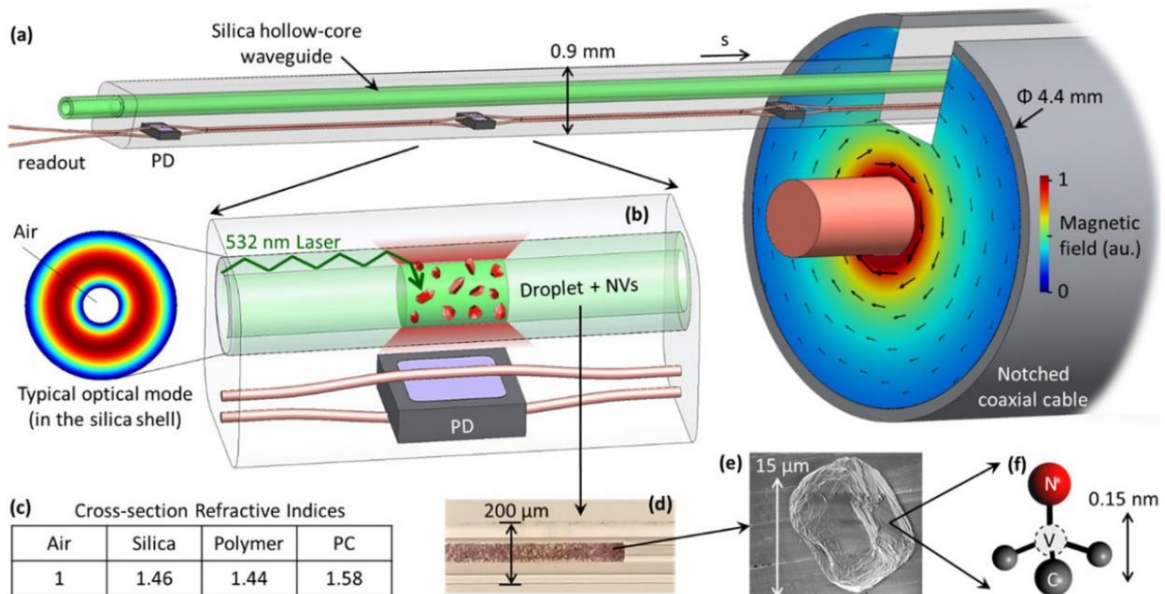


Figure 45. Fiber magnetometer mechanism.

a) Schematic of the microfluidic system that allows distributed long-range magnetometry. The hollow-core silica fiber is coated with a polymer that functions as cladding for light guidance. b) Zoom-in on one sensing module. The system is composed of a 532 nm laser source coupled to a hollow-core silica waveguide. Typical donut-shaped optical mode that propagates in the silica shell is shown. The droplet position is controlled using an air pressure pump connected at the end of the fiber. A liquid droplet mixed with >4 ppm NV concentration (estimated by manufacturer) micro-diamond particles (red crystals) is aligned with an embedded diode to collect red fluorescence. A notched coaxial cable waveguides the required microwave frequency to control the NV's spin state to provide ODMR. c) Refractive indices table of the cross section of the fiber (PC – polycarbonate). d) Photograph of the NV droplet. e) SEM photograph of a single micro-diamond. f) Simplified atomic structure of the NV, where the dashed circle is the vacancy. Source.: [152].

## 12.2 The diamond magnetic microscope imaging schemes

Recently, highly sensitive ensembles of NV centers [153] have been widely used in numerous imaging applications [154] in such diverse fields as NMR spectroscopy [155], condensed matter physics [156], geology [157], [158], biomagnetism [159] and others. The measuring technology consists in placing the test sample directly on top of a diamond crystal containing a thin near-surface layer of NV centers. Spin-dependent fluorescence imaging is performed using a CMOS or CCD camera in a wide-field detection scheme (Figure 46). The scheme has a diffraction-limited spatial resolution of  $\sim 500$  nm. Improvement in the technology of creating the thin diamond layers characterized with high density, preferential orientation, and long spin coherence time will provide an enhancement of the described NV-imaging applications performance.

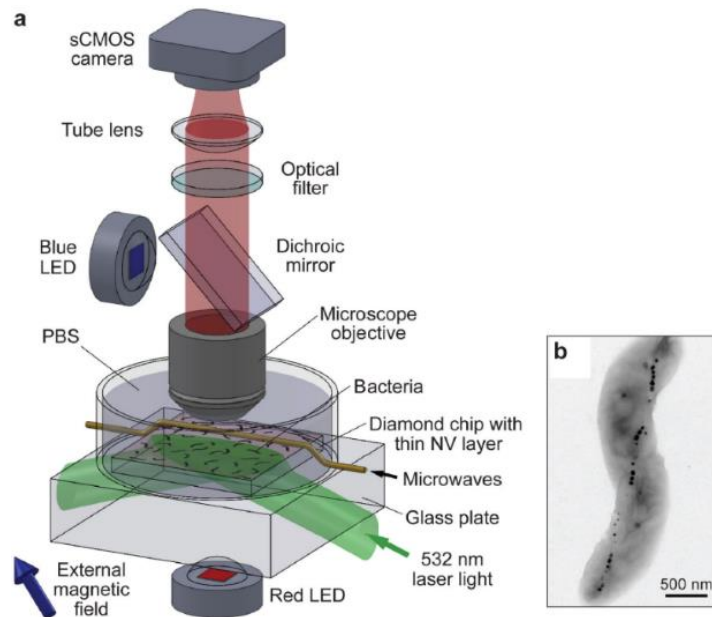


Figure 46. Wide-field magnetic imaging fluorescence microscope used for combined optical and magnetic imaging

a, Wide-field magnetic imaging fluorescence microscope used for combined optical and magnetic imaging. Live magnetotactic bacteria (MTB) are placed in phosphate-buffered saline (PBS) on the surface of a diamond chip implanted with nitrogen vacancy (NV) centers. Vector magnetic field images are derived from optically detected magnetic resonance (ODMR) interrogation of NV centers excited by a totally-internally-reflected 532 nm laser beam, and spatially correlated with bright field optical images. b, Typical transmission electron microscope (TEM) image of a *Magnetospirillum magneticum* AMB-1 bacterium. Magnetite nanoparticles appear as spots of high electron density. Source: [159].

Figure 47 shows the principle of operation of an atomic force microscope (AFM) using a probe based on NV centers [42]. Scanning a testing sample with such a microscope allows obtaining an image of the magnetic field with  $\sim$  nanometer resolution, while a gas atomic magnetometer provides only  $\sim$  millimeter resolution [160]. Such an ultra-high spatial resolution and a completely new level of applicability is achieved due to a significant reduction in the sensitive volume and, as a result, a small number of NV centers involved in the detection. This makes it possible to achieve the sensitivity of the order of  $\mu$ T.



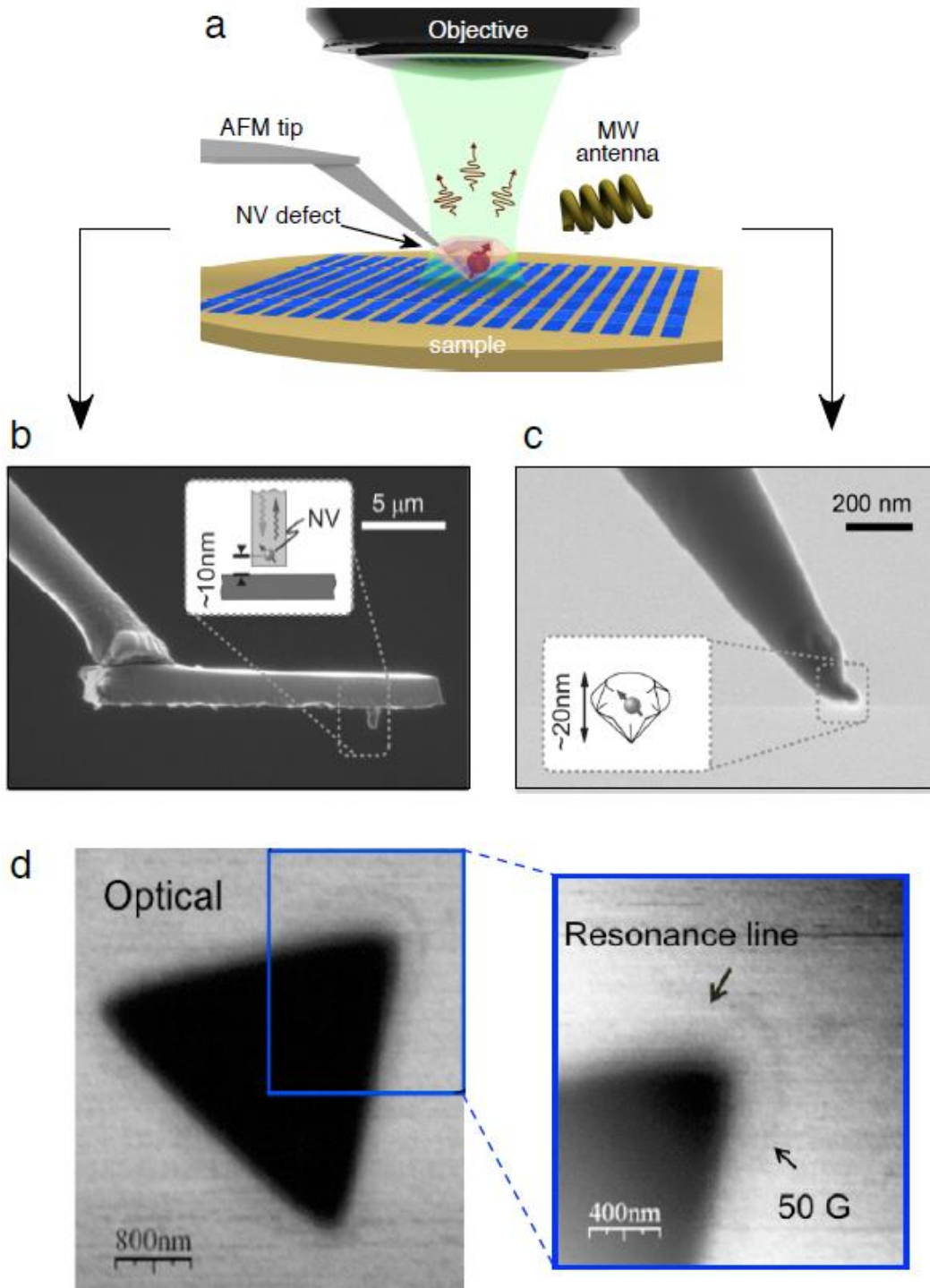


Figure 47. Principle of scanning-NV magnetometry which combines an atomic force microscope (AFM) and a confocal microscope.

The AFM tip is functionalised with a single NV defect and a microwave (MW) antenna is used to perform optical detection of the NV defect ESR transition. (b) All-diamond nanopillar probe with a single NV center placed at the apex of the tip through ion implantation. (c) NV defect hosted in a diamond nanocrystal grafted at the end of an AFM tip. (d) First experimental realization of scanning-NV magnetometry showing a magnetic field contour (50 G) around a triangularly shaped micro-magnet. Since the magnetic sample is opaque, it appears black in the image because the magnetometer is mounted in an inverted configuration. Source.: [42].

### 12.3 Applications of NV centers to sensing the inhomogeneities, deformations, stress and strain in crystal.

NV centers, in addition to the magnetic field, are sensitive to many physical quantities, including stress in crystal and deformations. This dependence was proposed in [161] to be used to create an accelerometer for the purpose of its application in the car security system – as a measurer of the force of an impact, which determines if an airbag has to inflate.

In [37] a method was proposed to measure the stress inhomogeneity present in the diamond AFM-probes in order to enhance the performance of the magnetic field imaging, which is significantly affected by such stresses. To optimize NV sensing, a diamond stress mapping method was proposed that restores stress tensor elements over a two-dimensional field of view using the ODMR method. Figure 48 shows such a millimeter-field-of-view stress imaging scheme with micrometer resolution, used for diamonds containing a thin surface layer of NV centers.

The mentioned accelerometer design and the described experiment demonstrate the application of the dependence of the spin states of NV centers on stress, strain, deformations and inhomogeneities in the crystal.

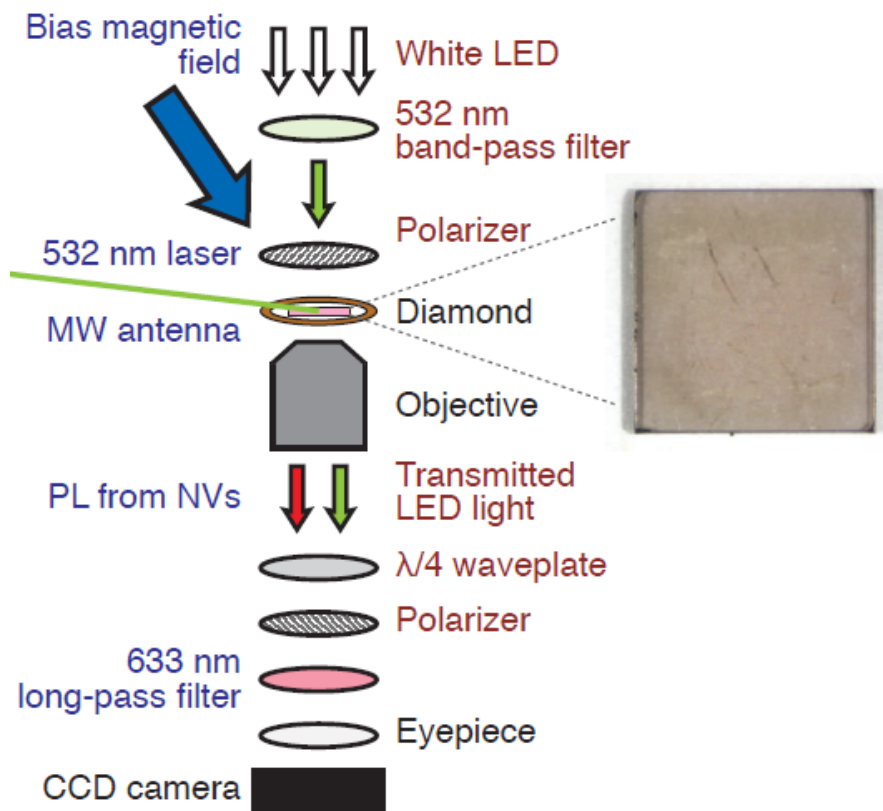


Figure 48. Schematic of the combined NV stress and birefringence imager.

The NV stress imager (blue labels) uses a 532 nm laser to illuminate the diamond, an applied microwave field to drive transitions between NV ground-state sublevels, and a bias magnetic field. The birefringence imager (maroon labels) uses an LED illuminator, two linear polarizers, and a quarter-wave plate. Both imagers use the same microscope and CCD camera (black labels) to collect and image the transmitted light. The photograph on the right shows the diamond sample studied. Source.: [37].

### 12.4 Nanodiamond for in vivo sensing and cell tracking applications

Diamonds are distinguished by excellent biological and physicochemical stability, which opens up wide possibilities for using nanometer diamond particles for fluorescent labeling and quantum measurements of biological cells. Proposed in [162], a prototype

of such a magnetometer, designed to detect magnetic nanoparticles in biomedical applications, is shown in Figure 49. The study of various biological issues such as the structure and dynamics of proteins in the cell using sensors based on NV centers is a new, developing area. Due to their unique properties, diamond magnetic field sensors with nanoscopic or even atomic precision can be used in living biological systems as probes for investigation the dynamics and structure of biomolecules in a biological environment, detecting the smallest magnetic fields, measuring temperature, and the state of electron spins.

Nanodiamonds differ from traditional fluorescent dyeing materials in a number of advantages. With low biotoxicity and good stability without photofading, they are excellent as a fluorescent labeling material for detection of gadolinium spin labels in artificial cell membranes and in NMR cell tracking applications. They can also be used to measure the cell temperature [163] and as a medium for drug delivery through chemical group modification [164].

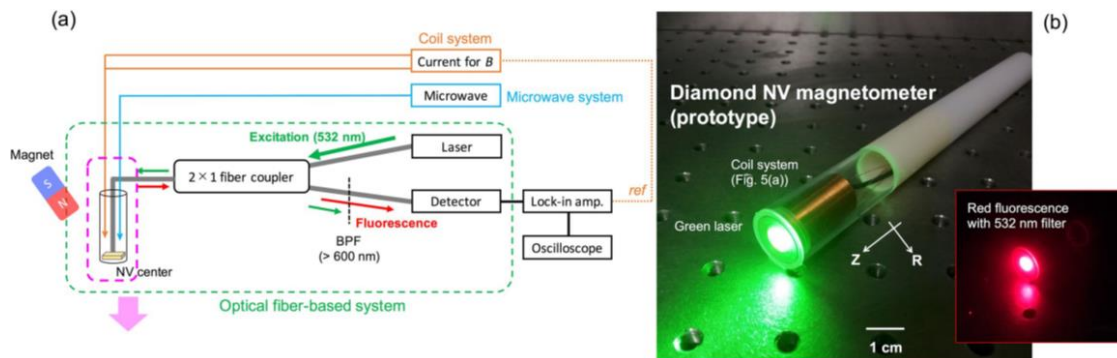


Figure 49. The prototype of NV center magnetometer for detecting magnetic nanoparticles in biomedical applications

(a) Schematic of driving and lock-in detection system of a magnetometer with diamond NV<sup>-</sup> center: MW for generating ESR, green laser for excitation of electron energy state of NV<sup>-</sup> center, photodetector for measuring red fluorescence, and electric current for generating AC magnetic fields. Excitation and luminescence light enters and returns through a bifurcated optical fiber bundle, respectively. The external magnetic fields of a permanent magnet produce dip splitting of each NV axis. (b) Image of the developed diamond NV magnetometer (prototype). The green laser excites red fluorescence in the diamond NV. The longitudinal and lateral directions are the Z-axis and R-axis, respectively. Source: [162].

## 12.5 Companies that offer magnetometers on NV centers, quantum diamond microscopes or quantum diamond microscope tips

### 12.5.1 WAINVAM-E (Ploemeur in the west region of France)

WAINVAM-E was created in April 2020. Since the summer of 2020, WAINVAN-E has been based in Ploemeur in the west region of France. Its main products are:

- Low Field NV Magnetometer [165] WAINMAG-LF is a highly sensitive compact vector magnetometer (Figure 50). According to the company's website, the WAINMAG-LF is designed to measure both static and rapidly fluctuating magnetic fields, making it an ideal candidate for non-destructive testing of metal parts.

The WAINMAG-LF consists of a fibre optic point magnetometer, of millimetre size for easy integration, and a control unit. The magnetic field is measured by the ODMR method. The diamond is illuminated with a green laser, and the photoluminescence of the diamond NV centers is collected and analyzed under MW excitation. This allows direct vector measurement of the magnetic field in the sensor reference frame. The WAINMAG-LF is suitable for use in an eddy current detection scheme and for the detection of static leakage fields of a defect in a

material due to very fast magnetic field measurements. The parameters of the WAINMAG-LF magnetometer available on the company's website are shown in Table 14 [165].

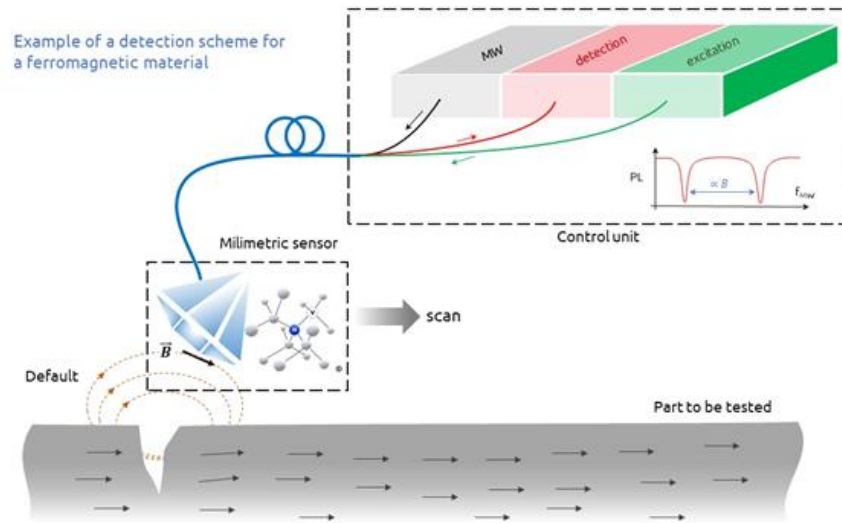


Figure 50. Low Field NV Magnetometer WAINMAG-LF. Source: [165].

**Table 14.** The parameters of the magnetometer WAINMAG-LF. Source: [165].

Magnetic field dynamics	0 to 1 mT
Sensitivity	3 nT / $\sqrt{\text{Hz}}$
Bandwidth	DC to 300 Hz
Sensor dimensions	Millimetric (customisable)
Distance between sensor and control unit	5m (more on request)
Voltage / frequency (mains)	230V / 50Hz
Power consumption	< 20W
Nominal operating temperature	20°C +/- 5°C
Max. storage temperature	From -20°C to 55°C, humidity <65%

- **Wide Field NV Imager [166]:** WAINIM-WF is a microscope that can quantitatively map the magnetic field generated by a millimeter sample with micrometer optical resolution (Figure 51). According to the company's website, this makes it ideal for studying micromagnetic samples in fields such as geology or spintronics, as well as imaging electric currents by reversing the Ørsted field.

WAINIM-WF consists of diamond with a layer enriched by NV centers. This layer is illuminated by a green laser and emits photoluminescence, which is collected by the camera. ODMR is performed by scanning the frequency of microwaves and analyzing the photoluminescence of each camera pixel. The device allows measuring the vector magnetic field in the layer of NV centers. Analysis of field

maps using appropriate inversion models makes it possible to trace magnetic field sources to any current or magnetization. Table 15 shows the parameters of the wide field NV imager WAINIM-WF, presented on the company's website [166].

**Table 15.** The parameters of the wide field NV imager WAINIM-WF. Source: [166].

Magnetic field dynamics	0 to 10 mT
Sensitivity	10 $\mu\text{T} / \sqrt{\text{Hz}}$
Maximum image size	3 $\times$ 3 mm
Dimensions of the instrument	700 $\times$ 700 $\times$ 700 mm
Voltage / frequency (network)	230V / 50Hz
Power consumption	< 20 W
Nominal operating temperature	20°C +/- 5°C
Max. storage temperature	From -20°C to 55°C, humidity <65%

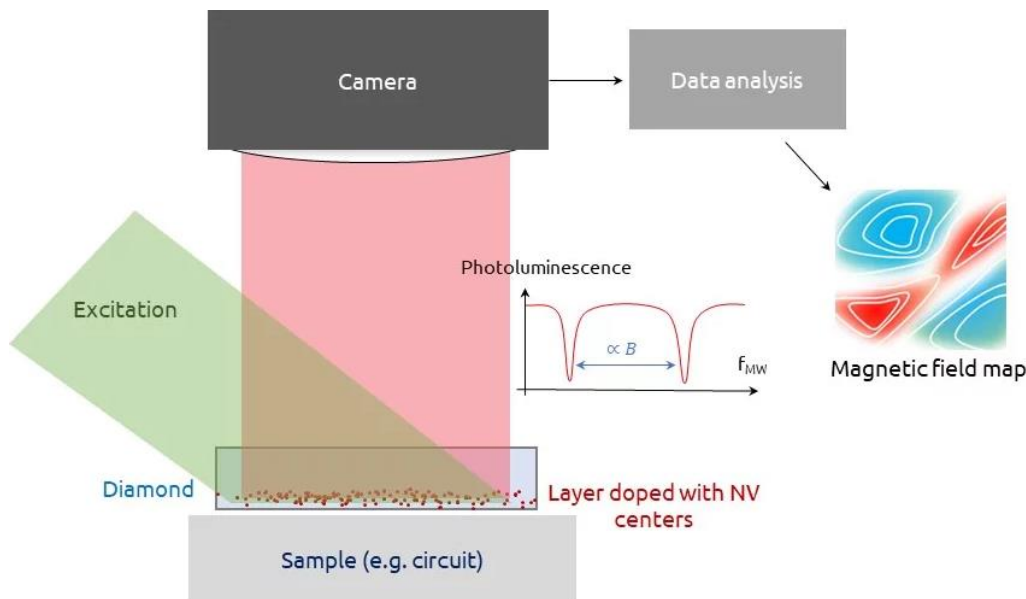


Figure 51. Wide Field NV Imager WAINIM-WF. Source: [166].

- High Field NV Magnetometer [167]: WAINMAG-ST is an ultra-stable magnetometer for stabilizing strong magnetic fields (Figure 52). According to the company's website, the WAINMAG-ST characterised by very low drift and small size, making it easy to integrate for the use in magnetic field control in fields ranging from advanced atomic physics experiments to medical imaging.

The WAINMAG-ST consists of a millimeter size fiber optic point magnetometer to facilitate its integration, and a control unit. The magnetic field is measured by the ODMR method. Having received the value of the magnetic field, it can be adjusted, for example, through feedback from the current that generates the field. On the other hand, the ODMR method allows to directly measure the temperature of the sensor, thereby eliminating thermal drift. Table 16 shows the parameters

of the High Field NV Magnetometer WAINMAG-ST, presented on the company's website [167].

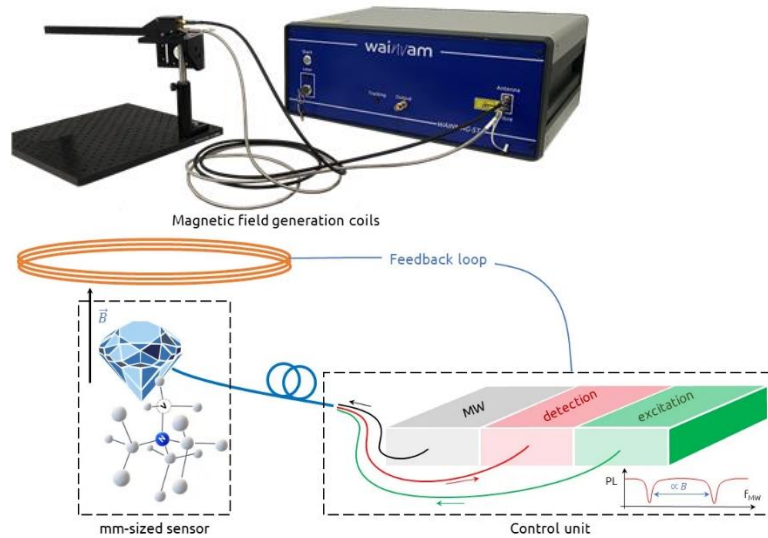


Figure 52. High Field NV Magnetometer WAINMAG-ST. Source: [167].

**Table 16.** The parameters of the High Field NV Magnetometer WAINMAG-ST. Source: [167].

Magnetic field dynamics	Up to 100 mT in standard measurements (more on request)
Drift	< ppm/day
Sensitivity	10 nT / $\sqrt{\text{Hz}}$
Bandwidth	DC to 100 Hz
Sensor dimensions	Millimetric (customisable)
Distance between sensor and control unit	5 m (more on request)
Voltage / frequency (mains)	230V / 50Hz
Power consumption	< 20 W
Best performance	20°C +/- 5°C
Max. storage temperature	From -20°C to 55°C, humidity <65%

- Electronic cards [168] Microwave Generator. According to the company's website, the WAINVAM-MW-GEN01 (Figure 53) is a radio-frequency (RF) transmitter that generates microwaves between 2100 and 3500 MHz. This module is controlled by a TTL to switch ON and OFF the single-ended RF output signal adjustable from 2100 to 3500 MHz with an output power of +25 dBm from 2.3 to 3 GHz and up to +28 dBm at 2.87 GHz. Specifications and absolute maximum ratings of microwave generator WAINVAM-MW-GEN01 presented on the company's website are summarised in tables 17 and 18 [168].

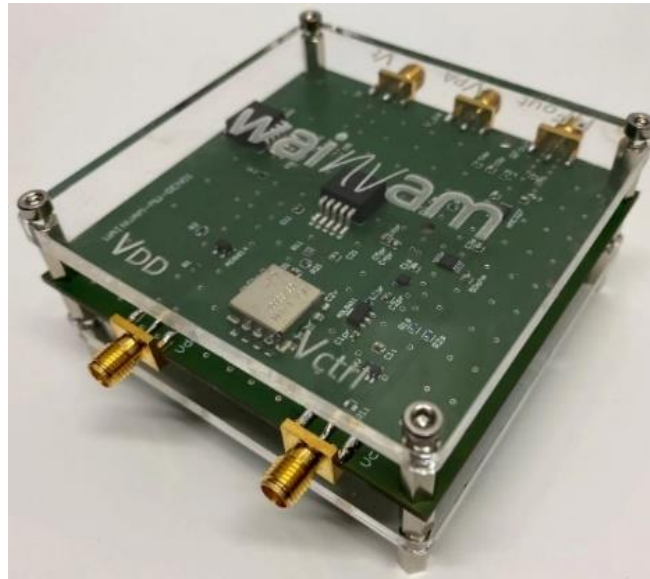


Figure 53. Microwave Generator WAINVAM-MW-GEN01. Source: [168].

Table 17. Specifications of microwave generator WAINVAM-MW-GEN01. Source: [168].

Parameter	Symbol	Min	Typ	Max	Units
<b>SWITCH</b>					
Isolation		20	35	45	dB
Switching speed	$t_{rise}, t_{fall}$		60		ns
<b>RF OUTPUT</b>					
RF frequency range	$f_{RF}$	2100		3500	MHz
Output impedance			50		$\Omega$
Return Loss			15		dB
<b>POWER SUPPLY</b>					
Supply Voltage					
LO tuning voltage	$V_t$	0		5	V
PA supply voltage	$V_{PA}$		5	6	V
Board supply voltage	$V_{dd}$		18	20	V
Supply Current					
Board supply current	$I_{dd}$		170	250	mA
PA supply current	$I_{PA}$		250	320	mA
<b>PERFORMANCE</b>					
Output power	$P_{out}$	10	25	28	dBm
Output Third-Order Intercept	$OIP_3$	36	40		dBm
Phase noise at					
100 kHz offset			-66		dBc/Hz
1 MHz offset			-95		dBc/Hz
10 MHz offset			-120		dBc/Hz



**Table 18.** Absolute maximum ratings of microwave generator WAINVAM-MW-GEN01. Source: [168].

Parameter	Rating
Board Supply Current	250 mA
PA Supply Current	320 mA
Board supply voltage $V_{DD}$	20 V
PA supply voltage $V_{PA}$	6V
Temperature	
Operating	-40 to +85 °C
Storage	-45 to +90 °C
ESD Sensitivity (Human Body Model)	1500 V

- Confocal NV microscope [169] The WAINVIEW Microscope, according to the company's website, is a confocal fluorescence microscope that allows one to observe the fluorescence of diamond NV centers and to determine their quantum state. It reliably, sensitively and kinetically measures pH and magnetic field changes in a variety of samples including oil, water and cell media.

The WAINVIEW microscope is equipped with a variable power green laser source that can be adapted to a specific application. The pulse system required for quantum detection allows the generation of very fast and precise sequences of light pulses. The incident beam is then directed onto the sample using a galvanometric mirror to scan the samples. The fluorescence signal from the diamonds is then recorded by a photon counter, which makes it possible to detect a low level of fluorescence in the pulse sequence. The WAINVIEW software converts the optical data into numerical data appropriate for each application for easy reading of the results. Table 19 shows the parameters of the WAINVIEW confocal NV microscope provided by the company's website [169].

**Table 19.** The parameters of the WAINVIEW confocal NV microscope. Source: [169].

Laser illumination	520nm
Variable light power	from 1μW to 1mW
Warm-up time	1h for high accuracy and kinetic measurements
Laser pulse and detection frequency	up to 2MHz
Spatial resolution	500nm, diffraction limit
Scan	2D galvanometric mirror
Pinhole	100μm
Detection filter	> 650nm
Photon detection efficacy	65% at 650nm





Detector noise	1500 photons/second
Measurement time	1 to 10 min, depending on the desired sensitivity
Magnetic species detection limit	1nM to 1 $\mu$ M
Size	70x70x70cm
Power supply	230V / 50Hz
Optimum temperature	22°C without interruption
Storage	-20°C to 55°C, humidity <65%.

- Relaxometer NV [170] The WAINVIEW relaxometer, according to information on the company's website, is a metrological device for measuring the fluorescence of diamond NV centers and, thus, determining their quantum state. It reliably, sensitively and kinetically measures changes in pressure, temperature, pH and magnetic field in a variety of samples, including oily and aqueous media.

The WAINVIEW relaxometer is equipped with a variable power green laser source that can be adapted to various applications. The pulse system required for quantum detection allows the generation of very fast and accurate light pulse sequences to perform the  $T_1$  relaxometry protocol. The incident beam is then directed towards the sample containing NV-center diamonds through the microscope objective. The fluorescence signal from the diamonds is then backscattered and picked up by a very sensitive and fast detector to identify the low level of fluorescence in the pulse sequence. The WAINVIEW software converts the optical data into the numerical data required by the application to make the results easier to read. Table 20 shows the parameters of the WAINVIEW relaxometer presented on the company's website [170].

**Table 20.** The parameters of the WAINVIEW relaxometer. Source: [170].

Laser illumination	520nm
Variable light power	from 1 $\mu$ W to 1mW
Warm-up time	1h for high accuracy and kinetic measurements
Laser pulse and detection frequency	up to 2MHz
Detection filter	> 650nm
NEP (noise equivalent power) of the detector	1.3fW/Hz <sup>1/2</sup>
Detector detection limit	2 pW RMS
Measurement time	1 to 10 min, depending on the desired sensitivity
Magnetic species detection limit	1nM to 1 $\mu$ M



Size	70x70x70cm
Power supply	230V / 50Hz
Optimum temperature	22°C without interruption
Storage	-20°C to 55°C, humidity <65%

### 12.5.2 QZabre (Zurich, Switzerland)

QZabre originated from the Spin Physics group of Prof. Christian Degen at ETH Zurich, Switzerland. Its main products are:

- Quantum Sensor Tips [171]. The QZabre quantum sensor tips, according to the information on the company's website, are a complete solution for scanning quantum sensors (Figure 54). The sensor chip contains a high-quality diamond tip with one built-in NV center mounted on a robust ceramic carrier plate. An integrated force feedback sensor ensures safe remote control. Each sensor chip is delivered fully assembled and characterized, ready to be used in experiments.

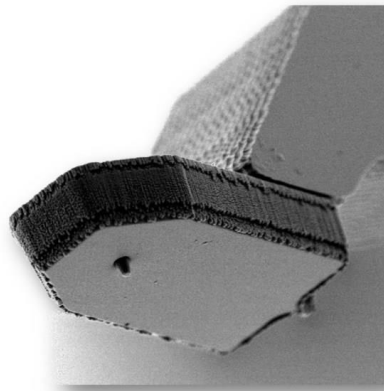


Figure 54. QZabre quantum sensor tip. Source: [171].

According to information on the company's website, the proposed Quantum Sensor Tips have the following properties [171]:

- Simple plug-and-play sensor chip
- Diamond probe tip etched from high quality, single crystal diamond
- Highest count rate and contrast
- Piezoelectric control of z-distance via quartz tuning fork
- Compatible with attoAFM/CFM microscope and Akiyama probe footprint

NV center tips with different orientations are also offered [171]:

- NV experiments, measurements are always projections onto the NV symmetry axis, which depends on the crystal orientation of the diamond from which the tips are made. The most widely available cut is  $\langle 100 \rangle$  which leads to NV orientations of  $54.7^\circ$  with respect to the normal. For many applications, this work very well.
- QZabre also offer tips with **in-plane** and **out-of-plane** orientation. This is especially useful for measurements with magnetic bias, as signal decreases with increasing off-axis magnetic fields, or elimination directional bias (**out-of-plane tips**).



Key specifications [171]:

Contrast	Better than 20/25%
Count rate at maximum contrast (0.75 NA)	150-700 kC/s
Saturation count rate (0.75 NA)	0.6-1.2 MC/s
Nominal depth of NV center	10 nm
Hyperfine splitting visible	On request
NV vector orientation	<111> (100-cut diamond)
Nominal magnetic sensitivity	1-10 $\mu\text{T}/\text{Hz}^{1/2}$

- QSM – Quantum Scanning Microscope [172]. The QSM is, according to the information on the company's website, a next-generation scanning probe microscope based on quantum sensing (Figure 55). It provides new capabilities and unmatched performance in the quantitative magnetic analysis of nanoscale surfaces and device elements.

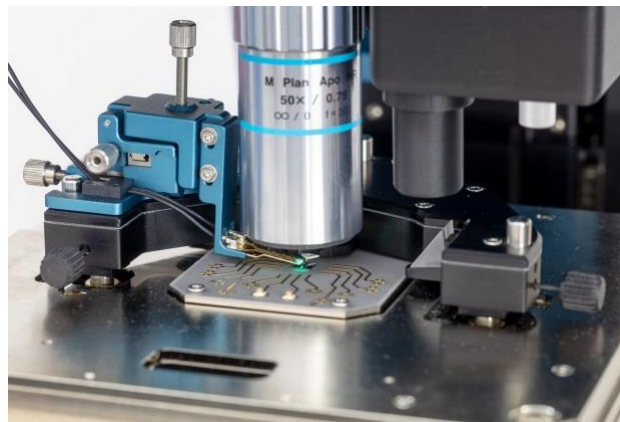


Figure 55. QZabre Quantum Scanning Microscope. Source: [172].

Quantum Scanning Microscop is characterised by [172]:

- Turn-key instrument with best in class scanning performance
- Magnetic field resolution better than 35 nm and sensitivity better than 1.3  $\mu\text{T}/\text{srqt}(\text{Hz})$
- Low drift scanning stage
- Optimised optical performance over the NV emission band for faster scanning
- Compatible with multiple excitation wavelengths

Key specifications [172]:

<b>Scanning modes</b>	ODMR (standard and fast feedback), Iso-B, Quench, pulsed (Rabi, Ramsey, T1, etc.), MOKE, AFM
<b>Scan range</b>	85 x 85 x 15 $\mu\text{m}$ , 0.2 nm resolution, 6 mm coarse range, closed loop
<b>Drift rate</b>	< 2 nm/h in temperature stabilized housing
<b>Magnetic spatial resolution</b>	better than 30 nm



<b>Magnetic sensitivity</b>	better than 1.3 $\mu\text{T}/\sqrt{\text{Hz}}$ in cw-ODMR using HF25-B2 depends on probe tip
<b>Optimised optical system</b>	>70% increase in optical transmission compared to standard CFM setups
<b>MOKE microscope</b>	The QSM includes a polar magneto-optical Kerr effect mode to quickly determine areas of interest
<b>Multi-colour excitation</b>	Compatible with green, red and yellow excitation wavelengths

The following features are included in the QSM systems (Figure 56) [172]:

- Scanning force microscope and controller, closed-loop control
- Optics head including NV excitation and detection channels, MOKE microscope, two bright field imaging systems including a pair of independent LEDs and CCD cameras
- Sample holder
- Sensor holder with force-feedback and integrated microwave connectivity
- Quantum control console including optical and microwave excitation and detection capabilities
- QS3 quantum control software package with an intuitive user interface
- You can customize the system with additional options:
- Time-domain option providing powerful pulsed quantum control and AC detection capabilities. Includes hardware and software suite.
- Vector electromagnet option providing switchable vector fields up to 80 mT

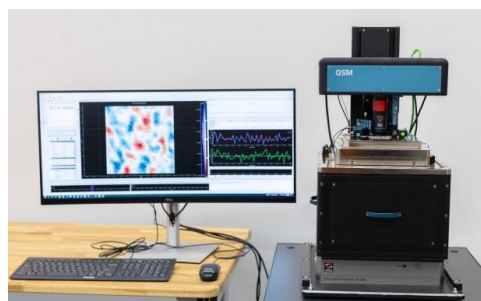


Figure 56. QZabre QSM system. Source: [172].

### 12.5.3 Qnami AG (Switzerland)

The company was founded in 2016; it started with the laboratory work of Prof. Dr. Patrick Maletinsky at the University of Basel. Its main product is:

- Qnami ProteusQ [173]. Qnami ProteusQ is, according to the information on the company's website, a complete quantum microscope system. It is the first scanning NV microscope for the analysis of magnetic materials at the atomic scale. The Qnami ProteusQ system comes with state-of-the-art electronics and software. Its flexible design allows for future adjustments and scaling, expansion and capability for upgrades. The proprietary Qnami ProteusQ quantum technology provides high precision directly imaging of the most subtle properties of measured samples and the effect of microscopic changes in experimental design or fabrication process.

The main features of the equipment are [173]:



- AFM
  - 5x5x15 mm<sup>3</sup> motorized approach system for XYZ sample positioning with positioning resolution < 1 μm
  - 100x100x15 (+/-10%) μm<sup>3</sup> XYZ piezo closed-loop sample scanner with XY non-linearity of 0.05%, and Z non-linearity of 0.05%
  - Noise level:
    - 0.1nm RMS in XY dimension in 200Hz bandwidth with capacitance sensors 'on'
    - 0.02nm RMS in XY dimension @ 100Hz bandwidth with capacitance sensors 'off'
    - < 0.04nm RMS Z capacitance sensor @ 1000Hz bandwidth
  - Maximum sample size: 40x50mm<sup>2</sup>, 15mm thickness
  - Quantilever tuning-fork probe holder
  - Integrated miniaturized microwave near-field antenna
  - 4x4x4 mm<sup>3</sup> xyz manual stage for near-field antenna positioning with resolution < 1 μm
  - NV bias magnet mounted on objective (vertical direction: -2.5 to +2.5 mT, manually adjustable)
- Optics
  - 100x Plan Apo infinity corrected objective, NA=0.7, working distance: 6mm
  - 30x30x10μm<sup>3</sup> XYZ closed loop piezo objective scanner with M26 x 36 TPI thread
  - Video microscope top channel, including LED illuminator and a USB Industry CMOS camera (DFK 22AUC03), 744x480 pxl (0.4Mpxl), 4.46x2.88mm<sup>2</sup> sensor size
  - Confocal optical unit with up-straight photon collection and 50μm multimode fiber output coupler
  - Optical diode laser (λ=515±5 nm), tunable output power 0.01 -20.0mW at focal point
  - Single photon counting module
- Microwave generator
  - Operating frequency bandwidth 2.5-3.5 GHz, 10Hz resolution
  - Maximum power> 30dBm, with 0.1dB power resolution
  - Gain compensated for flat power distribution across the whole frequency bandwidth
  - 4 General purpose Input-Output (GPIO) channels with TTL level specification
  - 1 Gigabit Ethernet connection port for data transmission
- Software
  - Windows software for control of Smartscan SPM modes
  - LabQ software for SNVM (NV fluorescence mode, optically detected magnetic resonance spectroscopy)
  - Fluorescence auto-track routine
  - Measurement scripting abilities via Jupyter Notebook

### 13. BIBLIOGRAPHY

- [1] R. Löfgren, “A theoretical investigation of the nitrogen-vacancy center in diamond as a single molecule sensor and qubit,” Luleå tekniska universitet, 2021.
- [2] L. J. Rogers *et al.*, “All-Optical Initialization, Readout, and Coherent Preparation of Single Silicon-Vacancy Spins in Diamond,” *Phys Rev Lett*, vol. 113, no. 26, p. 263602, Dec. 2014, doi: 10.1103/PhysRevLett.113.263602.
- [3] D. Qiu, Z. Sun, N. Gao, and H. Li, “Spin and charge state dependent electrical and magnetic properties of diamond with defects of vacancy and substituted silicon by first-principles calculation,” *Appl Phys Lett*, vol. 114, no. 17, p. 172401, Apr. 2019, doi: 10.1063/1.5092246.
- [4] R. Schirhagl, K. Chang, M. Loretz, and C. L. Degen, “Nitrogen-Vacancy Centers in Diamond: Nanoscale Sensors for Physics and Biology,” *Annu Rev Phys Chem*, vol. 65, no. 1, pp. 83–105, Apr. 2014, doi: 10.1146/annurev-physchem-040513-103659.
- [5] V. N. Mochalin, O. Shenderova, D. Ho, and Y. Gogotsi, “The properties and applications of nanodiamonds,” *Nat Nanotechnol*, vol. 7, no. 1, pp. 11–23, Jan. 2012, doi: 10.1038/nnano.2011.209.
- [6] A. Nagl, S. R. Hemelaar, and R. Schirhagl, “Improving surface and defect center chemistry of fluorescent nanodiamonds for imaging purposes—a review,” *Anal Bioanal Chem*, vol. 407, no. 25, pp. 7521–7536, Oct. 2015, doi: 10.1007/s00216-015-8849-1.
- [7] D. Amans *et al.*, “Nanodiamond synthesis by pulsed laser ablation in liquids,” *Diam Relat Mater*, vol. 18, no. 2–3, pp. 177–180, Feb. 2009, doi: 10.1016/j.diamond.2008.10.035.
- [8] Y. Morita *et al.*, “A Facile and Scalable Process for Size-Controllable Separation of Nanodiamond Particles as Small as 4 nm,” *Small*, vol. 4, no. 12, pp. 2154–2157, Dec. 2008, doi: 10.1002/sml.200800944.
- [9] J.-P. Boudou *et al.*, “High yield fabrication of fluorescent nanodiamonds,” *Nanotechnology*, vol. 20, no. 23, p. 235602, Jun. 2009, doi: 10.1088/0957-4484/20/23/235602.
- [10] M. E. Trusheim *et al.*, “Scalable Fabrication of High Purity Diamond Nanocrystals with Long-Spin-Coherence Nitrogen Vacancy Centers,” *Nano Lett*, vol. 14, no. 1, pp. 32–36, Jan. 2014, doi: 10.1021/nl402799u.
- [11] S. Chouaieb *et al.*, “Optimizing synthetic diamond samples for quantum sensing technologies by tuning the growth temperature,” *Diam Relat Mater*, vol. 96, pp. 85–89, Jun. 2019, doi: 10.1016/j.diamond.2019.04.022.
- [12] T. Miyazaki *et al.*, “Atomistic mechanism of perfect alignment of nitrogen-vacancy centers in diamond,” *Appl Phys Lett*, vol. 105, no. 26, p. 261601, Dec. 2014, doi: 10.1063/1.4904988.



- [13] V. M. Acosta *et al.*, “Diamonds with a high density of nitrogen-vacancy centers for magnetometry applications,” *Phys Rev B*, vol. 80, no. 11, p. 115202, Sep. 2009, doi: 10.1103/PhysRevB.80.115202.
- [14] N. Chen *et al.*, “Defect and Stress Reduction in High-Pressure and High-Temperature Synthetic Diamonds Using Gradient Cooling Technology,” *Cryst Growth Des*, vol. 20, no. 5, pp. 3358–3364, May 2020, doi: 10.1021/acs.cgd.0c00148.
- [15] R. S. Balmer *et al.*, “Chemical vapour deposition synthetic diamond: materials, technology and applications,” *Journal of Physics: Condensed Matter*, vol. 21, no. 36, p. 364221, Sep. 2009, doi: 10.1088/0953-8984/21/36/364221.
- [16] H. Chatterjee, “Magnetic field sensing based on the infrared absorption of nitrogen-vacancy centers in diamond,” Universität des Saarlandes, Saarbrücken, 2021.
- [17] S. Eaton-Magana and J. E. Shigley, “Observations on CVD-Grown Synthetic Diamonds: A Review,” *Gems & Gemology*, pp. 222–245, Nov. 2016, doi: 10.5741/GEMS.52.3.222.
- [18] S. Eaton-Magana, J. E. Shigley, and C. M. Breeding, “Observations on HPHT-Grown Synthetic Diamonds: A Review,” *Gems & Gemology*, vol. 53, no. 3, pp. 262–284, Nov. 2017, doi: 10.5741/GEMS.53.3.262.
- [19] Rob Bates, “Just How Eco-Friendly Are Lab-Created Diamonds?,” <https://www.jckonline.com/editorial-article/lab-created-diamonds-eco-friendly/>, Mar. 29, 2019. <https://www.jckonline.com/editorial-article/lab-created-diamonds-eco-friendly/> (accessed Nov. 17, 2022).
- [20] M. W. Doherty, N. B. Manson, P. Delaney, F. Jelezko, J. Wrachtrup, and L. C. L. Hollenberg, “The nitrogen-vacancy colour centre in diamond,” *Phys Rep*, vol. 528, no. 1, pp. 1–45, Jul. 2013, doi: 10.1016/j.physrep.2013.02.001.
- [21] Z. Yin, N. Zhao, and T. Li, “Hybrid opto-mechanical systems with nitrogen-vacancy centers,” *Sci China Phys Mech Astron*, vol. 58, no. 5, pp. 1–12, May 2015, doi: 10.1007/s11433-015-5651-1.
- [22] J. S. Hodges *et al.*, “Long-lived NV<sup>-</sup> spin coherence in high-purity diamond membranes,” *New J Phys*, vol. 14, no. 9, p. 093004, Sep. 2012, doi: 10.1088/1367-2630/14/9/093004.
- [23] S. Pezzagna, B. Naydenov, F. Jelezko, J. Wrachtrup, and J. Meijer, “Creation efficiency of nitrogen-vacancy centres in diamond,” *New J Phys*, vol. 12, no. 6, p. 065017, Jun. 2010, doi: 10.1088/1367-2630/12/6/065017.
- [24] K. Ohno *et al.*, “Engineering shallow spins in diamond with nitrogen delta-doping,” *Appl Phys Lett*, vol. 101, no. 8, p. 082413, Aug. 2012, doi: 10.1063/1.4748280.
- [25] K. Ohashi *et al.*, “Negatively Charged Nitrogen-Vacancy Centers in a 5 nm Thin <sup>12</sup>C Diamond Film,” *Nano Lett*, vol. 13, no. 10, pp. 4733–4738, Oct. 2013, doi: 10.1021/nl402286v.



- [26] B. K. Ofori-Okai *et al.*, “Spin properties of very shallow nitrogen vacancy defects in diamond,” *Phys Rev B*, vol. 86, no. 8, p. 081406, Aug. 2012, doi: 10.1103/PhysRevB.86.081406.
- [27] J. Tisler *et al.*, “Fluorescence and Spin Properties of Defects in Single Digit Nanodiamonds,” *ACS Nano*, vol. 3, no. 7, pp. 1959–1965, Jul. 2009, doi: 10.1021/nn9003617.
- [28] B. R. Smith *et al.*, “Five-Nanometer Diamond with Luminescent Nitrogen-Vacancy Defect Centers,” *Small*, vol. 5, no. 14, pp. 1649–1653, Jul. 2009, doi: 10.1002/smll.200801802.
- [29] J. M. Smith, S. A. Meynell, A. C. Bleszynski Jayich, and J. Meijer, “Colour centre generation in diamond for quantum technologies,” *Nanophotonics*, vol. 8, no. 11, pp. 1889–1906, Nov. 2019, doi: 10.1515/nanoph-2019-0196.
- [30] M. L. Markham *et al.*, “CVD diamond for spintronics,” *Diam Relat Mater*, vol. 20, no. 2, pp. 134–139, Feb. 2011, doi: 10.1016/j.diamond.2010.11.016.
- [31] J. Achard, V. Jacques, and A. Tallaire, “Chemical vapour deposition diamond single crystals with nitrogen-vacancy centres: a review of material synthesis and technology for quantum sensing applications,” *J Phys D Appl Phys*, vol. 53, no. 31, p. 313001, Jul. 2020, doi: 10.1088/1361-6463/ab81d1.
- [32] E. v. Levine *et al.*, “Principles and techniques of the quantum diamond microscope,” *Nanophotonics*, vol. 8, no. 11, pp. 1945–1973, Sep. 2019, doi: 10.1515/nanoph-2019-0209.
- [33] B. Naydenov *et al.*, “Increasing the coherence time of single electron spins in diamond by high temperature annealing,” *Appl Phys Lett*, vol. 97, no. 24, p. 242511, Dec. 2010, doi: 10.1063/1.3527975.
- [34] H. Ozawa, K. Tahara, H. Ishiwata, M. Hatano, and T. Iwasaki, “Formation of perfectly aligned nitrogen-vacancy-center ensembles in chemical-vapor-deposition-grown diamond (111),” *Applied Physics Express*, vol. 10, no. 4, p. 045501, Apr. 2017, doi: 10.7567/APEX.10.045501.
- [35] A. D. P. L. Craik, P. Kehayias, A. S. Greenspon, and X. Zang, “A microwave-assisted spectroscopy technique for determining charge state in nitrogen-vacancy ensembles in diamond,” *Preprint*, Nov. 2018.
- [36] A. Horsley *et al.*, “Microwave Device Characterization Using a Widefield Diamond Microscope,” *Phys Rev Appl*, vol. 10, no. 4, p. 044039, Oct. 2018, doi: 10.1103/PhysRevApplied.10.044039.
- [37] P. Kehayias *et al.*, “Imaging crystal stress in diamond using ensembles of nitrogen-vacancy centers,” *Phys Rev B*, vol. 100, no. 17, p. 174103, Nov. 2019, doi: 10.1103/PhysRevB.100.174103.
- [38] J. F. Barry *et al.*, “Sensitivity optimization for NV-diamond magnetometry,” *Rev Mod Phys*, vol. 92, no. 1, p. 015004, Mar. 2020, doi: 10.1103/RevModPhys.92.015004.
- [39] A. Gali, M. Fyta, and E. Kaxiras, “*Ab initio* supercell calculations on nitrogen-vacancy center in diamond: Electronic structure and hyperfine





- tensors,” *Phys Rev B*, vol. 77, no. 15, p. 155206, Apr. 2008, doi: 10.1103/PhysRevB.77.155206.
- [40] B. Smeltzer, L. Childress, and A. Gali, “<sup>13</sup>C hyperfine interactions in the nitrogen-vacancy centre in diamond,” *New J Phys*, vol. 13, no. 2, p. 025021, Feb. 2011, doi: 10.1088/1367-2630/13/2/025021.
- [41] A. Jarmola, V. M. Acosta, K. Jensen, S. Chemerisov, and D. Budker, “Temperature- and Magnetic-Field-Dependent Longitudinal Spin Relaxation in Nitrogen-Vacancy Ensembles in Diamond,” *Phys Rev Lett*, vol. 108, no. 19, p. 197601, May 2012, doi: 10.1103/PhysRevLett.108.197601.
- [42] L. Rondin, J.-P. Tetienne, T. Hingant, J.-F. Roch, P. Maletinsky, and V. Jacques, “Magnetometry with nitrogen-vacancy defects in diamond,” *Reports on Progress in Physics*, vol. 77, no. 5, p. 056503, May 2014, doi: 10.1088/0034-4885/77/5/056503.
- [43] A. Gruber, A. Dräbenstedt, C. Tietz, L. Fleury, J. Wrachtrup, and C. von Borczyskowski, “Scanning Confocal Optical Microscopy and Magnetic Resonance on Single Defect Centers,” *Science (1979)*, vol. 276, no. 5321, pp. 2012–2014, Jun. 1997, doi: 10.1126/science.276.5321.2012.
- [44] J. Köhler, “Magnetic resonance of a single molecular spin,” *Phys Rep*, vol. 310, no. 5–6, pp. 261–339, Mar. 1999, doi: 10.1016/S0370-1573(98)00057-X.
- [45] F. Dolde *et al.*, “Electric-field sensing using single diamond spins,” *Nat Phys*, vol. 7, no. 6, pp. 459–463, Jun. 2011, doi: 10.1038/nphys1969.
- [46] G. Balasubramanian *et al.*, “Ultralong spin coherence time in isotopically engineered diamond,” *Nat Mater*, vol. 8, no. 5, pp. 383–387, May 2009, doi: 10.1038/nmat2420.
- [47] J.-P. Tetienne *et al.*, “Magnetic-field-dependent photodynamics of single NV defects in diamond: an application to qualitative all-optical magnetic imaging,” *New J Phys*, vol. 14, no. 10, p. 103033, Oct. 2012, doi: 10.1088/1367-2630/14/10/103033.
- [48] N. D. Lai, D. Zheng, F. Jelezko, F. Treussart, and J.-F. Roch, “Influence of a static magnetic field on the photoluminescence of an ensemble of nitrogen-vacancy color centers in a diamond single-crystal,” *Appl Phys Lett*, vol. 95, no. 13, p. 133101, Sep. 2009, doi: 10.1063/1.3238467.
- [49] A. Dréau *et al.*, “Avoiding power broadening in optically detected magnetic resonance of single NV defects for enhanced dc magnetic field sensitivity,” *Phys Rev B*, vol. 84, no. 19, p. 195204, Nov. 2011, doi: 10.1103/PhysRevB.84.195204.
- [50] H. Fedder *et al.*, “Towards T<sub>1</sub>-limited magnetic resonance imaging using Rabi beats,” *Applied Physics B*, vol. 102, no. 3, pp. 497–502, Mar. 2011, doi: 10.1007/s00340-011-4408-4.
- [51] F. Jelezko, T. Gaebel, I. Popa, A. Gruber, and J. Wrachtrup, “Observation of Coherent Oscillations in a Single Electron Spin,” *Phys Rev Lett*, vol. 92, no. 7, p. 076401, Feb. 2004, doi: 10.1103/PhysRevLett.92.076401.



- [52] S. Steinert *et al.*, “Magnetic spin imaging under ambient conditions with sub-cellular resolution,” *Nat Commun*, vol. 4, no. 1, p. 1607, Jun. 2013, doi: 10.1038/ncomms2588.
- [53] J. M. Schloss, “Optimizing Nitrogen-Vacancy Diamond Magnetic Sensors and Imagers for Broadband Sensitivity,” Massachusetts Institute of Technology, 2019.
- [54] V. M. Acosta, E. Bauch, M. P. Ledbetter, A. Waxman, L.-S. Bouchard, and D. Budker, “Temperature Dependence of the Nitrogen-Vacancy Magnetic Resonance in Diamond,” *Phys Rev Lett*, vol. 104, no. 7, p. 070801, Feb. 2010, doi: 10.1103/PhysRevLett.104.070801.
- [55] E. Bauch *et al.*, “Ultralong Dephasing Times in Solid-State Spin Ensembles via Quantum Control,” *Phys Rev X*, vol. 8, no. 3, p. 031025, Jul. 2018, doi: 10.1103/PhysRevX.8.031025.
- [56] K. Fang *et al.*, “High-Sensitivity Magnetometry Based on Quantum Beats in Diamond Nitrogen-Vacancy Centers,” *Phys Rev Lett*, vol. 110, no. 13, p. 130802, Mar. 2013, doi: 10.1103/PhysRevLett.110.130802.
- [57] B. J. Shields, Q. P. Unterreithmeier, N. P. de Leon, H. Park, and M. D. Lukin, “Efficient Readout of a Single Spin State in Diamond via Spin-to-Charge Conversion,” *Phys Rev Lett*, vol. 114, no. 13, p. 136402, Mar. 2015, doi: 10.1103/PhysRevLett.114.136402.
- [58] I. Lovchinsky *et al.*, “Nuclear magnetic resonance detection and spectroscopy of single proteins using quantum logic,” *Science (1979)*, vol. 351, no. 6275, pp. 836–841, Feb. 2016, doi: 10.1126/science.aad8022.
- [59] P. Neumann *et al.*, “Single-Shot Readout of a Single Nuclear Spin,” *Science (1979)*, vol. 329, no. 5991, pp. 542–544, Jul. 2010, doi: 10.1126/science.1189075.
- [60] M. V. Berry, “Quantal phase factors accompanying adiabatic changes,” *Proceedings of the Royal Society of London. A. Mathematical and Physical Sciences*, vol. 392, no. 1802, pp. 45–57, Mar. 1984, doi: 10.1098/rspa.1984.0023.
- [61] D. Maclaurin, M. W. Doherty, L. C. L. Hollenberg, and A. M. Martin, “Measurable Quantum Geometric Phase from a Rotating Single Spin,” *Phys Rev Lett*, vol. 108, no. 24, p. 240403, Jun. 2012, doi: 10.1103/PhysRevLett.108.240403.
- [62] C. Zu *et al.*, “Experimental realization of universal geometric quantum gates with solid-state spins,” *Nature*, vol. 514, no. 7520, pp. 72–75, Oct. 2014, doi: 10.1038/nature13729.
- [63] S. Arroyo-Camejo, A. Lazarev, S. W. Hell, and G. Balasubramanian, “Room temperature high-fidelity holonomic single-qubit gate on a solid-state spin,” *Nat Commun*, vol. 5, no. 1, p. 4870, Dec. 2014, doi: 10.1038/ncomms5870.
- [64] C. G. Yale, F. J. Heremans, B. B. Zhou, A. Auer, G. Burkard, and D. D. Awschalom, “Optical manipulation of the Berry phase in a solid-state spin qubit,” *Nat Photonics*, vol. 10, no. 3, pp. 184–189, Mar. 2016, doi: 10.1038/nphoton.2015.278.



- [65] B. B. Zhou, P. C. Jerger, V. O. Shkolnikov, F. J. Heremans, G. Burkard, and D. D. Awschalom, “Holonomic Quantum Control by Coherent Optical Excitation in Diamond,” *Phys Rev Lett*, vol. 119, no. 14, p. 140503, Oct. 2017, doi: 10.1103/PhysRevLett.119.140503.
- [66] K. Arai, J. Lee, C. Belthangady, D. R. Glenn, H. Zhang, and R. L. Walsworth, “Geometric phase magnetometry using a solid-state spin,” *Nat Commun*, vol. 9, no. 1, p. 4996, Dec. 2018, doi: 10.1038/s41467-018-07489-z.
- [67] L. M. Pham *et al.*, “Enhanced solid-state multispin metrology using dynamical decoupling,” *Phys Rev B*, vol. 86, no. 4, p. 045214, Jul. 2012, doi: 10.1103/PhysRevB.86.045214.
- [68] J. Zhang *et al.*, “Diamond Nitrogen-Vacancy Center Magnetometry: Advances and Challenges,” *Applied Physics*, 2020.
- [69] M. S. Grinolds *et al.*, “Nanoscale magnetic imaging of a single electron spin under ambient conditions,” *Nat Phys*, vol. 9, no. 4, pp. 215–219, Apr. 2013, doi: 10.1038/nphys2543.
- [70] E. van Oort and M. Glasbeek, “Electric-field-induced modulation of spin echoes of N-V centers in diamond,” *Chem Phys Lett*, vol. 168, no. 6, pp. 529–532, May 1990, doi: 10.1016/0009-2614(90)85665-Y.
- [71] L. P. McGuinness *et al.*, “Quantum measurement and orientation tracking of fluorescent nanodiamonds inside living cells,” *Nat Nanotechnol*, vol. 6, no. 6, pp. 358–363, Jun. 2011, doi: 10.1038/nnano.2011.64.
- [72] P. Neumann *et al.*, “High-Precision Nanoscale Temperature Sensing Using Single Defects in Diamond,” *Nano Lett*, vol. 13, no. 6, pp. 2738–2742, Jun. 2013, doi: 10.1021/nl401216y.
- [73] M. W. Doherty *et al.*, “Electronic Properties and Metrology Applications of the Diamond NV<sup>-</sup> Center under Pressure,” *Phys Rev Lett*, vol. 112, no. 4, p. 047601, Jan. 2014, doi: 10.1103/PhysRevLett.112.047601.
- [74] M. E. Trusheim and D. Englund, “Wide-field strain imaging with preferentially aligned nitrogen-vacancy centers in polycrystalline diamond,” *New J Phys*, vol. 18, no. 12, p. 123023, Dec. 2016, doi: 10.1088/1367-2630/aa5040.
- [75] A. Barfuss, J. Teissier, E. Neu, A. Nunnenkamp, and P. Maletinsky, “Strong mechanical driving of a single electron spin,” *Nat Phys*, vol. 11, no. 10, pp. 820–824, Oct. 2015, doi: 10.1038/nphys3411.
- [76] A. Barfuss, M. Kasperczyk, J. Kölbl, and P. Maletinsky, “Spin-stress and spin-strain coupling in diamond-based hybrid spin oscillator systems,” *Phys Rev B*, vol. 99, no. 17, p. 174102, May 2019, doi: 10.1103/PhysRevB.99.174102.
- [77] J. R. Maze *et al.*, “Properties of nitrogen-vacancy centers in diamond: the group theoretic approach,” *New J Phys*, vol. 13, no. 2, p. 025025, Feb. 2011, doi: 10.1088/1367-2630/13/2/025025.
- [78] G. Chatzidrosos *et al.*, “Miniature Cavity-Enhanced Diamond Magnetometer,” *Phys Rev Appl*, vol. 8, no. 4, p. 044019, Oct. 2017, doi: 10.1103/PhysRevApplied.8.044019.



- [79] C.-F. Liu *et al.*, “Ultra-sensitive hybrid diamond nanothermometer,” *Natl Sci Rev*, vol. 8, no. 5, May 2021, doi: 10.1093/nsr/nwaa194.
- [80] D. M. Toyli, D. J. Christle, A. Alkauskas, B. B. Buckley, C. G. van de Walle, and D. D. Awschalom, “Measurement and Control of Single Nitrogen-Vacancy Center Spins above 600 K,” *Phys Rev X*, vol. 2, no. 3, p. 031001, Jul. 2012, doi: 10.1103/PhysRevX.2.031001.
- [81] Y. Dumeige *et al.*, “Magnetometry with nitrogen-vacancy ensembles in diamond based on infrared absorption in a doubly resonant optical cavity,” *Phys Rev B*, vol. 87, no. 15, p. 155202, Apr. 2013, doi: 10.1103/PhysRevB.87.155202.
- [82] E. Bourgeois *et al.*, “Photoelectric detection of electron spin resonance of nitrogen-vacancy centres in diamond,” *Nat Commun*, vol. 6, no. 1, p. 8577, Dec. 2015, doi: 10.1038/ncomms9577.
- [83] J. M. Taylor *et al.*, “High-sensitivity diamond magnetometer with nanoscale resolution,” *Nat Phys*, vol. 4, no. 10, pp. 810–816, Oct. 2008, doi: 10.1038/nphys1075.
- [84] H. Y. Carr and E. M. Purcell, “Effects of Diffusion on Free Precession in Nuclear Magnetic Resonance Experiments,” *Physical Review*, vol. 94, no. 3, pp. 630–638, May 1954, doi: 10.1103/PhysRev.94.630.
- [85] S. Meiboom and D. Gill, “Modified Spin-Echo Method for Measuring Nuclear Relaxation Times,” *Review of Scientific Instruments*, vol. 29, no. 8, pp. 688–691, Aug. 1958, doi: 10.1063/1.1716296.
- [86] K. Beha, A. Batalov, N. B. Manson, R. Bratschitsch, and A. Leitenstorfer, “Optimum Photoluminescence Excitation and Recharging Cycle of Single Nitrogen-Vacancy Centers in Ultrapure Diamond,” *Phys Rev Lett*, vol. 109, no. 9, p. 097404, Aug. 2012, doi: 10.1103/PhysRevLett.109.097404.
- [87] K. Bayat, J. Choy, M. Farrokh Baroughi, S. Meesala, and M. Loncar, “Efficient, Uniform, and Large Area Microwave Magnetic Coupling to NV Centers in Diamond Using Double Split-Ring Resonators,” *Nano Lett*, vol. 14, no. 3, pp. 1208–1213, Mar. 2014, doi: 10.1021/nl404072s.
- [88] N. Zhang *et al.*, “Microwave Magnetic Field Coupling with Nitrogen-Vacancy Center Ensembles in Diamond with High Homogeneity,” *Appl Magn Reson*, vol. 47, no. 6, pp. 589–599, Jun. 2016, doi: 10.1007/s00723-016-0777-5.
- [89] D. Labanowski *et al.*, “Voltage-driven, local, and efficient excitation of nitrogen-vacancy centers in diamond,” *Sci Adv*, vol. 4, no. 9, Sep. 2018, doi: 10.1126/sciadv.aat6574.
- [90] W. Jia, Z. Shi, X. Qin, X. Rong, and J. Du, “Ultra-broadband coplanar waveguide for optically detected magnetic resonance of nitrogen-vacancy centers in diamond,” *Review of Scientific Instruments*, vol. 89, no. 6, p. 064705, Jun. 2018, doi: 10.1063/1.5028335.
- [91] K. Sasaki *et al.*, “Broadband, large-area microwave antenna for optically detected magnetic resonance of nitrogen-vacancy centers in diamond,” *Review of Scientific Instruments*, vol. 87, no. 5, p. 053904, May 2016, doi: 10.1063/1.4952418.



- [92] E. R. Eisenach, J. F. Barry, L. M. Pham, R. G. Rojas, D. R. Englund, and D. A. Braje, “Broadband loop gap resonator for nitrogen vacancy centers in diamond,” *Review of Scientific Instruments*, vol. 89, no. 9, p. 094705, Sep. 2018, doi: 10.1063/1.5037465.
- [93] M. Mrózek, J. Mlynarczyk, D. S. Rudnicki, and W. Gawlik, “Circularly polarized microwaves for magnetic resonance study in the GHz range: Application to nitrogen-vacancy in diamonds,” *Appl Phys Lett*, vol. 107, no. 1, p. 013505, Jul. 2015, doi: 10.1063/1.4923252.
- [94] A. M. Wojciechowski *et al.*, “Contributed Review: Camera-limits for wide-field magnetic resonance imaging with a nitrogen-vacancy spin sensor,” *Review of Scientific Instruments*, vol. 89, no. 3, p. 031501, Mar. 2018, doi: 10.1063/1.5010282.
- [95] Oliver J. Woodman, “An introduction to inertial navigation,” Cambridge, Aug. 2007. Accessed: Nov. 17, 2022. [Online]. Available: <https://www.cl.cam.ac.uk/techreports/UCAM-CL-TR-696.pdf>
- [96] “Inertial Navigation Systems Information.” [https://www.globalspec.com/learnmore/sensors\\_transducers\\_detectors/tilt\\_sensing/inertial\\_gyros](https://www.globalspec.com/learnmore/sensors_transducers_detectors/tilt_sensing/inertial_gyros) (accessed Nov. 17, 2022).
- [97] P. Groves, *Principles of GNSS, Inertial, and Multisensor Integrated Navigation Systems, Second Edition*. 2013.
- [98] H. Hu, Z. Yin, N. Li, S. Che, X. Shu, and C. Liu, “Inertial Sensing Disruptive Technology Based on Levitated Optomechanics,” *Chinese Journal of Engineering Science*, vol. 20, no. 6, p. 112, 2018, doi: 10.15302/J-SSCAE-2018.06.018.
- [99] L. Zhao, X. Shen, L. Ji, and P. Huang, “Inertial measurement with solid-state spins of nitrogen-vacancy center in diamond,” *Adv Phys X*, vol. 7, no. 1, Dec. 2022, doi: 10.1080/23746149.2021.2004921.
- [100] Bill Schweber, “Magnetic-Field Navigation as an ‘Alternative’ GPS?,” <https://www.mwrf.com/technologies/systems/article/21145895/magnetic-field-navigation-as-an-alternative-gps>, Oct. 26, 2020. <https://www.mwrf.com/technologies/systems/article/21145895/magnetic-field-navigation-as-an-alternative-gps> (accessed Nov. 17, 2022).
- [101] A. Canciani and J. Raquet, “Absolute Positioning Using the Earth’s Magnetic Anomaly Field,” *Navigation*, vol. 63, no. 2, pp. 111–126, Jun. 2016, doi: 10.1002/navi.138.
- [102] “Tech That’s Cool as [Dark] Ice,” <https://www.lockheedmartin.com/en-us/news/features/2019-features/tech-thats-cool-as-dark-ice.html>. <https://www.lockheedmartin.com/en-us/news/features/2019-features/tech-thats-cool-as-dark-ice.html> (accessed Nov. 17, 2022).
- [103] “(quantum) (magnetometer) assignee: (Lockheed Corp) status: GRANT.” <https://patents.google.com/?q=quantum&q=magnetometer&assignee=Lockheed+Corp&status=GRANT> (accessed Oct. 17, 2022).
- [104] A. M. Edmonds *et al.*, “Characterisation of CVD diamond with high concentrations of nitrogen for magnetic-field sensing applications,”



*Materials for Quantum Technology*, vol. 1, no. 2, p. 025001, Jun. 2021, doi: 10.1088/2633-4356/abd88a.

- [105] “Quantum Magnetometer Augments GPS,” May 09, 2019. <https://www.insidequantumtechnology.com/news-archive/quantum-magnetometer-augments-gps/> (accessed Oct. 17, 2022).
- [106] A. Graps, “Quantum Magnetometers: Navigating Human Realms,” Jul. 26, 2022. <https://www.insidequantumtechnology.com/news-archive/quantum-magnetometers-navigating-human-realms> (accessed Oct. 17, 2022).
- [107] A. A. Wood *et al.*, “Quantum measurement of a rapidly rotating spin qubit in diamond,” *Sci Adv*, vol. 4, no. 5, May 2018, doi: 10.1126/sciadv.aar7691.
- [108] A. A. Wood, L. C. L. Hollenberg, R. E. Scholten, and A. M. Martin, “Observation of a Quantum Phase from Classical Rotation of a Single Spin,” *Phys Rev Lett*, vol. 124, no. 2, p. 020401, Jan. 2020, doi: 10.1103/PhysRevLett.124.020401.
- [109] A. A. Wood *et al.*, “Magnetic pseudo-fields in a rotating electron–nuclear spin system,” *Nat Phys*, vol. 13, no. 11, pp. 1070–1073, Nov. 2017, doi: 10.1038/nphys4221.
- [110] M. P. Ledbetter, K. Jensen, R. Fischer, A. Jarmola, and D. Budker, “Gyroscopes based on nitrogen-vacancy centers in diamond,” *Phys Rev A (Coll Park)*, vol. 86, no. 5, p. 052116, Nov. 2012, doi: 10.1103/PhysRevA.86.052116.
- [111] A. Ajoy and P. Cappellaro, “Stable three-axis nuclear-spin gyroscope in diamond,” *Phys Rev A (Coll Park)*, vol. 86, no. 6, p. 062104, Dec. 2012, doi: 10.1103/PhysRevA.86.062104.
- [112] A. Jarmola *et al.*, “Demonstration of diamond nuclear spin gyroscope,” *Sci Adv*, vol. 7, no. 43, Oct. 2021, doi: 10.1126/sciadv.abl3840.
- [113] C. Zhang, H. Yuan, Z. Tang, W. Quan, and J. C. Fang, “Inertial rotation measurement with atomic spins: From angular momentum conservation to quantum phase theory,” *Appl Phys Rev*, vol. 3, no. 4, p. 041305, Dec. 2016, doi: 10.1063/1.4972187.
- [114] X. Song, L. Wang, F. Feng, L. Lou, W. Diao, and C. Duan, “Nanoscale quantum gyroscope using a single <sup>13</sup>C nuclear spin coupled with a nearby NV center in diamond,” *J Appl Phys*, vol. 123, no. 11, p. 114301, Mar. 2018, doi: 10.1063/1.5000787.
- [115] V. v. Soshenko *et al.*, “Nuclear Spin Gyroscope based on the Nitrogen Vacancy Center in Diamond,” *Phys Rev Lett*, vol. 126, no. 19, p. 197702, May 2021, doi: 10.1103/PhysRevLett.126.197702.
- [116] J. H. Simpson, J. T. Fraser, and I. A. Greenwood, “An Optically Pumped Nuclear Magnetic Resonance Gyroscope,” *IEEE Transactions on Aerospace*, vol. 1, no. 2, pp. 1107–1110, 1963, doi: 10.1109/TA.1963.4319483.
- [117] P. Rabl, P. Cappellaro, M. V. G. Dutt, L. Jiang, J. R. Maze, and M. D. Lukin, “Strong magnetic coupling between an electronic spin qubit and a mechanical resonator,” *Phys Rev B*, vol. 79, no. 4, p. 041302, Jan. 2009, doi: 10.1103/PhysRevB.79.041302.



- [118] Z. Yin, T. Li, X. Zhang, and L. M. Duan, “Large quantum superpositions of a levitated nanodiamond through spin-optomechanical coupling,” *Phys Rev A (Coll Park)*, vol. 88, no. 3, p. 033614, Sep. 2013, doi: 10.1103/PhysRevA.88.033614.
- [119] M. A. Kowarsky, L. C. L. Hollenberg, and A. M. Martin, “Non-Abelian geometric phase in the diamond nitrogen-vacancy center,” *Phys Rev A (Coll Park)*, vol. 90, no. 4, p. 042116, Oct. 2014, doi: 10.1103/PhysRevA.90.042116.
- [120] N. El-Sheimy and A. Youssef, “Inertial sensors technologies for navigation applications: state of the art and future trends,” *Satellite Navigation*, vol. 1, no. 1, p. 2, Dec. 2020, doi: 10.1186/s43020-019-0001-5.
- [121] R. Tycko, “Adiabatic Rotational Splittings and Berry’s Phase in Nuclear Quadrupole Resonance,” *Phys Rev Lett*, vol. 58, no. 22, pp. 2281–2284, Jun. 1987, doi: 10.1103/PhysRevLett.58.2281.
- [122] S. Chen, “Quantum Physicists Found a New, Safer Way to Navigate,” Nov. 01, 2018. <https://www.wired.com/story/quantum-physicists-found-a-new-safer-way-to-navigate> (accessed Oct. 17, 2022).
- [123] A. Jarmola *et al.*, “Robust optical readout and characterization of nuclear spin transitions in nitrogen-vacancy ensembles in diamond,” *Phys Rev Res*, vol. 2, no. 2, p. 023094, Apr. 2020, doi: 10.1103/PhysRevResearch.2.023094.
- [124] C. A. Hart, J. M. Schloss, M. J. Turner, P. J. Scheidegger, E. Bauch, and R. L. Walsworth, “N-V–diamond magnetic microscopy using a double quantum 4-r Ramsey protocol,” *Phys Rev Appl*, vol. 15, no. 4, p. 044020, Apr. 2021, doi: 10.1103/PhysRevApplied.15.044020.
- [125] M. Rademacher, J. Millen, and Y. L. Li, “Quantum sensing with nanoparticles for gravimetry: when bigger is better,” *Advanced Optical Technologies*, vol. 9, no. 5, pp. 227–239, Nov. 2020, doi: 10.1515/aot-2020-0019.
- [126] X.-Y. Chen and Z.-Q. Yin, “High-precision gravimeter based on a nano-mechanical resonator hybrid with an electron spin,” *Opt Express*, vol. 26, no. 24, p. 31577, Nov. 2018, doi: 10.1364/OE.26.031577.
- [127] S. Castelletto, L. Rosa, and A. Boretti, “Micro-manipulation of nanodiamonds containing NV centers for quantum applications,” *Diam Relat Mater*, vol. 106, p. 107840, Jun. 2020, doi: 10.1016/j.diamond.2020.107840.
- [128] S. Kolkowitz *et al.*, “Coherent Sensing of a Mechanical Resonator with a Single-Spin Qubit,” *Science (1979)*, vol. 335, no. 6076, pp. 1603–1606, Mar. 2012, doi: 10.1126/science.1216821.
- [129] J. Millen, T. S. Monteiro, R. Pettit, and A. N. Vamivakas, “Optomechanics with levitated particles,” *Reports on Progress in Physics*, vol. 83, no. 2, p. 026401, Feb. 2020, doi: 10.1088/1361-6633/ab6100.
- [130] F. Monteiro, S. Ghosh, A. G. Fine, and D. C. Moore, “Optical levitation of 10-ng spheres with nano-  $g$  acceleration



sensitivity,” *Phys Rev A (Coll Park)*, vol. 96, no. 6, p. 063841, Dec. 2017, doi: 10.1103/PhysRevA.96.063841.

- [131] P. Kumar and M. Bhattacharya, “Magnetometry via spin-mechanical coupling in levitated optomechanics,” *Opt Express*, vol. 25, no. 16, p. 19568, Aug. 2017, doi: 10.1364/OE.25.019568.
- [132] M. Scala, M. S. Kim, G. W. Morley, P. F. Barker, and S. Bose, “Matter-Wave Interferometry of a Levitated Thermal Nano-Oscillator Induced and Probed by a Spin,” *Phys Rev Lett*, vol. 111, no. 18, p. 180403, Oct. 2013, doi: 10.1103/PhysRevLett.111.180403.
- [133] P. Storey and C. Cohen-Tannoudji, “The Feynman path integral approach to atomic interferometry. A tutorial,” *Journal de Physique II*, vol. 4, no. 11, pp. 1999–2027, Nov. 1994, doi: 10.1051/jp2:1994103.
- [134] A. Geraci and H. Goldman, “Sensing short range forces with a nanosphere matter-wave interferometer,” *Physical Review D*, vol. 92, no. 6, p. 062002, Sep. 2015, doi: 10.1103/PhysRevD.92.062002.
- [135] C. Wan *et al.*, “Free Nano-Object Ramsey Interferometry for Large Quantum Superpositions,” *Phys Rev Lett*, vol. 117, no. 14, p. 143003, Sep. 2016, doi: 10.1103/PhysRevLett.117.143003.
- [136] J.-C. Jaskula, K. Saha, A. Ajoy, D. J. Twitchen, M. Markham, and P. Cappellaro, “Cross-Sensor Feedback Stabilization of an Emulated Quantum Spin Gyroscope,” *Phys Rev Appl*, vol. 11, no. 5, p. 054010, May 2019, doi: 10.1103/PhysRevApplied.11.054010.
- [137] S. D. Bennett, N. Y. Yao, J. Otterbach, P. Zoller, P. Rabl, and M. D. Lukin, “Phonon-Induced Spin-Spin Interactions in Diamond Nanostructures: Application to Spin Squeezing,” *Phys Rev Lett*, vol. 110, no. 15, p. 156402, Apr. 2013, doi: 10.1103/PhysRevLett.110.156402.
- [138] J.-Q. Zhang *et al.*, “Fast optical cooling of nanomechanical cantilever with the dynamical Zeeman effect,” *Opt Express*, vol. 21, no. 24, p. 29695, Dec. 2013, doi: 10.1364/OE.21.029695.
- [139] K. v. Kepesidis, S. D. Bennett, S. Portolan, M. D. Lukin, and P. Rabl, “Phonon cooling and lasing with nitrogen-vacancy centers in diamond,” *Phys Rev B*, vol. 88, no. 6, p. 064105, Aug. 2013, doi: 10.1103/PhysRevB.88.064105.
- [140] P. Rabl, “Cooling of mechanical motion with a two-level system: The high-temperature regime,” *Phys Rev B*, vol. 82, no. 16, p. 165320, Oct. 2010, doi: 10.1103/PhysRevB.82.165320.
- [141] E. R. MacQuarrie, M. Otten, S. K. Gray, and G. D. Fuchs, “Cooling a mechanical resonator with nitrogen-vacancy centres using a room temperature excited state spin–strain interaction,” *Nat Commun*, vol. 8, no. 1, p. 14358, Apr. 2017, doi: 10.1038/ncomms14358.
- [142] Z. Y. Xu, Y. M. Hu, W. L. Yang, M. Feng, and J. F. Du, “Deterministically entangling distant nitrogen-vacancy centers by a nanomechanical cantilever,” *Phys Rev A (Coll Park)*, vol. 80, no. 2, p. 022335, Aug. 2009, doi: 10.1103/PhysRevA.80.022335.





- [143] P. Rabl, S. J. Kolkowitz, F. H. L. Koppens, J. G. E. Harris, P. Zoller, and M. D. Lukin, “A quantum spin transducer based on nanoelectromechanical resonator arrays,” *Nat Phys*, vol. 6, no. 8, pp. 602–608, Aug. 2010, doi: 10.1038/nphys1679.
- [144] O. Arcizet, V. Jacques, A. Siria, P. Poncharal, P. Vincent, and S. Seidelin, “A single nitrogen-vacancy defect coupled to a nanomechanical oscillator,” *Nat Phys*, vol. 7, no. 11, pp. 879–883, Nov. 2011, doi: 10.1038/nphys2070.
- [145] J. L. Webb *et al.*, “Nanotesla sensitivity magnetic field sensing using a compact diamond nitrogen-vacancy magnetometer,” *Appl Phys Lett*, vol. 114, no. 23, p. 231103, Jun. 2019, doi: 10.1063/1.5095241.
- [146] F. M. Stürner *et al.*, “Compact integrated magnetometer based on nitrogen-vacancy centres in diamond,” *Diam Relat Mater*, vol. 93, pp. 59–65, Mar. 2019, doi: 10.1016/j.diamond.2019.01.008.
- [147] D. Zheng *et al.*, “A hand-held magnetometer based on an ensemble of nitrogen-vacancy centers in diamond,” *J Phys D Appl Phys*, vol. 53, no. 15, p. 155004, Apr. 2020, doi: 10.1088/1361-6463/ab6af2.
- [148] D. Kim, M. I. Ibrahim, C. Foy, M. E. Trusheim, R. Han, and D. R. Englund, “A CMOS-integrated quantum sensor based on nitrogen–vacancy centres,” *Nat Electron*, vol. 2, no. 7, pp. 284–289, Jul. 2019, doi: 10.1038/s41928-019-0275-5.
- [149] M. I. Ibrahim, C. Foy, D. R. Englund, and R. Han, “High-Scalability CMOS Quantum Magnetometer With Spin-State Excitation and Detection of Diamond Color Centers,” *IEEE J Solid-State Circuits*, vol. 56, no. 3, pp. 1001–1014, Mar. 2021, doi: 10.1109/JSSC.2020.3027056.
- [150] S.-C. Zhang *et al.*, “A robust fiber-based quantum thermometer coupled with nitrogen-vacancy centers,” *Review of Scientific Instruments*, vol. 92, no. 4, p. 044904, Apr. 2021, doi: 10.1063/5.0044824.
- [151] D. Duan, V. K. Kavatamane, S. R. Arumugam, Y.-K. Tzeng, H.-C. Chang, and G. Balasubramanian, “Tapered ultra-high numerical aperture optical fiber tip for nitrogen vacancy ensembles based endoscope in a fluidic environment,” *Appl Phys Lett*, vol. 116, no. 11, p. 113701, Mar. 2020, doi: 10.1063/1.5140785.
- [152] S. Maayani, C. Foy, D. Englund, and Y. Fink, “Distributed Quantum Fiber Magnetometry,” *Laser Photon Rev*, vol. 13, no. 7, p. 1900075, Jul. 2019, doi: 10.1002/lpor.201900075.
- [153] T. Wolf *et al.*, “Subpicotesla Diamond Magnetometry,” *Phys Rev X*, vol. 5, no. 4, p. 041001, Oct. 2015, doi: 10.1103/PhysRevX.5.041001.
- [154] S. Steinert *et al.*, “High sensitivity magnetic imaging using an array of spins in diamond,” *Review of Scientific Instruments*, vol. 81, no. 4, p. 043705, Apr. 2010, doi: 10.1063/1.3385689.
- [155] D. R. Glenn, D. B. Bucher, J. Lee, M. D. Lukin, H. Park, and R. L. Walsworth, “High-resolution magnetic resonance spectroscopy using a solid-state spin sensor,” *Nature*, vol. 555, no. 7696, pp. 351–354, Mar. 2018, doi: 10.1038/nature25781.



- [156] D. A. Broadway *et al.*, “Spatial mapping of band bending in semiconductor devices using in situ quantum sensors,” *Nat Electron*, vol. 1, no. 9, pp. 502–507, Sep. 2018, doi: 10.1038/s41928-018-0130-0.
- [157] R. R. Fu *et al.*, “Solar nebula magnetic fields recorded in the Semarkona meteorite,” *Science (1979)*, vol. 346, no. 6213, pp. 1089–1092, Nov. 2014, doi: 10.1126/science.1258022.
- [158] D. R. Glenn *et al.*, “Micrometer-scale magnetic imaging of geological samples using a quantum diamond microscope,” *Geochemistry, Geophysics, Geosystems*, vol. 18, no. 8, pp. 3254–3267, Aug. 2017, doi: 10.1002/2017GC006946.
- [159] D. le Sage *et al.*, “Optical magnetic imaging of living cells,” *Nature*, vol. 496, no. 7446, pp. 486–489, Apr. 2013, doi: 10.1038/nature12072.
- [160] J. Kitching, “Chip-scale atomic devices,” *Appl Phys Rev*, vol. 5, no. 3, p. 031302, Sep. 2018, doi: 10.1063/1.5026238.
- [161] R. Mouris, “Quantum Enhanced Accelerometer using NV Centres in Diamond,” Delft University of Technology, Delft, 2019.
- [162] A. Kuwahata *et al.*, “Magnetometer with nitrogen-vacancy center in a bulk diamond for detecting magnetic nanoparticles in biomedical applications,” *Sci Rep*, vol. 10, no. 1, p. 2483, Dec. 2020, doi: 10.1038/s41598-020-59064-6.
- [163] G. Kucsko *et al.*, “Nanometre-scale thermometry in a living cell,” *Nature*, vol. 500, no. 7460, pp. 54–58, Aug. 2013, doi: 10.1038/nature12373.
- [164] Y. Wu, F. Jelezko, M. B. Plenio, and T. Weil, “Diamond Quantum Devices in Biology,” *Angewandte Chemie International Edition*, vol. 55, no. 23, pp. 6586–6598, Jun. 2016, doi: 10.1002/anie.201506556.
- [165] “Low Field NV Magnetometer.” <https://wainvam-e.com/equipment/low-field-nv-magnetometer/> (accessed Oct. 17, 2022).
- [166] “Wide Field NV Imager.” <https://wainvam-e.com/equipment/wide-field-nv-imager/> (accessed Oct. 17, 2022).
- [167] “High Field NV Magnetometer.” <https://wainvam-e.com/equipment/high-field-nv-magnetometer/> (accessed Oct. 18, 2022).
- [168] “Electronic cards.” <https://wainvam-e.com/equipment/electronic-cards/> (accessed Oct. 18, 2022).
- [169] “Confocal NV microscope.” <https://wainvam-e.com/equipment/confocal-nv-microscope/> (accessed Oct. 18, 2022).
- [170] “Relaxometer NV.” <https://wainvam-e.com/equipment/relaxometer-nv/> (accessed Oct. 18, 2022).
- [171] “Quantum Sensor Tips.” <https://qzabre.com/tips/> (accessed Oct. 18, 2022).
- [172] “QSM – Quantum Scanning Microscope.” <https://qzabre.com/microscope/> (accessed Oct. 18, 2022).



[173] “Qnami ProteusQ.” <https://qnami.ch/portfolio/proteusq/> (accessed Oct. 18, 2022).




---

# QFIRST

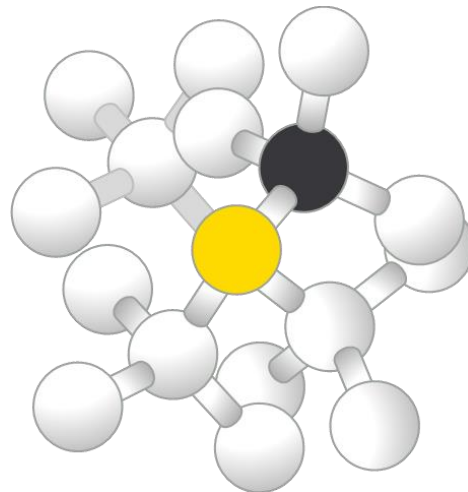
## Quantum Sensing & Metrology

### Nitrogen Vacancy Centres in Diamond

## State of the Art

Edited by Phd. Nina Slobodian, 2022

---



[www.tecnalia.com](http://www.tecnalia.com)



[www.ehu.eus](http://www.ehu.eus)



<https://cfm.ehu.es>



[www.tekniker.com](http://www.tekniker.com)



<https://www.a-v-s.es/>

This initiative is supported by the Basque Government through the ELKARTEK Program under Grant KK2022/00062 – Qfirst, Devices based on Quantum Technologies.

